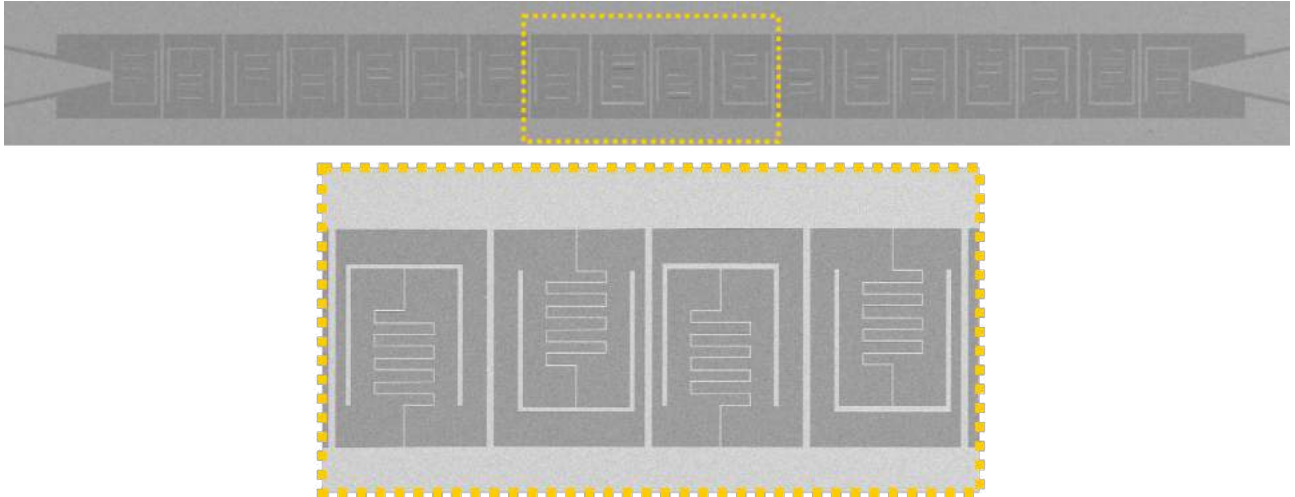


# Microwave Superconducting Metamaterial for Analog Quantum Simulation

MASTER THESIS



Author: Vera Jo Weibel  
Supervisor: Vincent Jouanny  
Professor: Prof. Dr. Pasquale Scarlino  
Group: Hybrid Quantum Circuits Laboratory, EPFL  
First Assessor: Prof. Dr. Christian Schönenberger  
Time frame: 01.02.2021 - 29.10.2021

## Abstract

In this thesis we investigate a possible realization of a bosonic multimode environment for analog quantum simulation. This platform consists of a metamaterial implemented by an one-dimensional array of coupled superconducting microwave cavities made from thin Niobium Nitride (NbN) films. Such disordered superconductor allows to reach a very high kinetic inductance, which presents a two-fold advantage. First, it allows to reach ultra-strong coupling with an artificial atom as the capacitive coupling is proportional to the square root of the resonators' impedance. The impedance of the resonator can be highly increased thanks to its kinetic inductance. Second, its high kinetic inductance allows for very compact resonator and array dimensions: Our resonator have a width of  $50\text{ }\mu\text{m}$ , allowing three arrays to fit on a chip of 4 by 7 mm. Furthermore, metamaterials allow engineering a non-trivial photonic dispersion relation, where it is possible to obtain states displaying topological properties (so-called SSH-states). This coupled resonator array was first simulated and modelled using finite element simulations and numerical calculations based on ABCD circuit models and a tight-binding Hamiltonian. The observed features could be qualitatively reproduced in measurement. The topological array configuration exhibits hybridised edge modes in the center of the middle band gap, characteristic for the SSH model. In conclusion, we succeeded in realising a metamaterial which allows for flexible engineering of the resulting band spectrum, a promising first step towards spin boson model simulations.

# Contents

<b>1</b>	<b>Introduction</b>	<b>3</b>
<b>2</b>	<b>Coupled Resonator Arrays</b>	<b>5</b>
2.1	Parallel RLC Resonator . . . . .	5
2.1.1	Transmission Spectrum of Hanged Resonator . . . . .	7
2.2	Hybridised Resonators . . . . .	8
2.3	Theoretical Models of A Coupled Resonator Array . . . . .	8
2.3.1	ABCD Matrix . . . . .	8
2.3.2	Lagrangian Formalism . . . . .	11
2.4	High Kinetic Inductance . . . . .	15
<b>3</b>	<b>Materials and Methods</b>	<b>17</b>
3.1	Design . . . . .	17
3.1.1	Resonator . . . . .	17
3.1.2	Waveguide for Transmission Measurements . . . . .	18
3.1.3	Waveguide for Hanged Resonators . . . . .	19
3.2	Simulation . . . . .	19
3.3	Fabrication . . . . .	20
3.4	Cryogenic System . . . . .	21
3.4.1	Measurement Setup . . . . .	22
3.5	Fitting . . . . .	23
3.5.1	Hanged Resonators . . . . .	23
3.5.2	Arrays . . . . .	24
<b>4</b>	<b>Modelling</b>	<b>25</b>
4.1	Dimer . . . . .	25
4.2	Array . . . . .	25
4.2.1	$S_{21}$ Transmission Spectra . . . . .	25
4.2.2	Current Distributions . . . . .	26
4.2.3	Second-Neighbour Coupling . . . . .	28
4.2.4	Displacement of HEMs . . . . .	30
<b>5</b>	<b>Experimental Results</b>	<b>33</b>
5.1	Characterisation of Resonators . . . . .	33
5.2	Arrays . . . . .	34
5.2.1	Influence of Geometry of Feedline on Transmission Spectrum . . . . .	34
5.2.2	Power Sweep . . . . .	35
5.2.3	Comparison to Simulation . . . . .	36
5.2.4	Decay Rate and Density of States . . . . .	37
5.2.5	Evolution of Topological Peak Amplitude With Number of Resonators . . . . .	39
5.2.6	Engineering the Band Spectrum . . . . .	41
<b>6</b>	<b>Conclusion</b>	<b>43</b>
<b>7</b>	<b>Outlook</b>	<b>43</b>
7.1	Hexagonal Lattice . . . . .	43
7.2	Coupling to Transmon . . . . .	44
7.3	Study of Array Non-Linearity . . . . .	45
	<b>Acknowledgements</b>	<b>46</b>
	<b>References</b>	<b>47</b>
	<b>Appendix</b>	<b>50</b>
<b>A</b>	<b>Derivation of SSH Model</b>	<b>50</b>
A.1	Bulk Hamiltonian . . . . .	51
A.2	Edge States . . . . .	53

<b>B</b>	<b>Supplementary Simulation Data</b>	<b>55</b>
B.1	4 LC Array with Ghost Feedline . . . . .	55
B.2	16 LC Array with Ghost Feedline . . . . .	56
<b>C</b>	<b>Supplementary Measurement Data</b>	<b>57</b>
C.1	Hanged Resonators . . . . .	57
C.2	16 LC Array with T-shaped Feedline . . . . .	58
C.3	16 LC Array with Ghost Feedline . . . . .	59
C.4	32 LC Array with Ghost Feedline . . . . .	60
C.5	64 LC Array with Ghost Feedline . . . . .	61

# 1 Introduction

Systems in nature are oftentimes described by many particles interacting with each other. To model such many-body systems, it is necessary to define a playground which allows to simulate the couplings and correlations between particles. However, modelling such systems relying on classical computing resources is not feasible, due to their complexity. Advances in technology lead to the emergence of a new research field called quantum simulation. There, complex quantum systems are investigated by using *quantum* hardware, i.e. hardware which inherently obeys quantum mechanical laws [1]. One of the most interesting models to be studied in this manner is the quantum impurity model. Most generally, a quantum impurity system consists of an “impurity” (small system with few degrees of freedom) coupled to an “environment” or “bath” (large system with numerous degrees of freedom). Quantum mechanics is needed to describe both the impurity and bath [2]. Two prominent implementations of quantum impurity models are the Kondo model [3, 4] and the spin boson model [5, 6]. In both models, the impurity has only one degree of freedom, namely spin. The Kondo model describes magnetic impurities in a nonmagnetic metal, i.e. an alloy, simplified to a single impurity with spin  $\frac{1}{2}$  coupled to the non-interacting conduction band electrons for temperatures reaching absolute zero [4]. Spin boson models can be used to simulate dissipation in quantum mechanics or to study light-atom interaction. To model dissipation, a two-level system such as a spin impurity is coupled to a bath of bosonic modes, which are described by harmonic oscillators [6]. We consider a multimode bosonic system whose spectrum is represented in Figure 1.1. This multimode bosonic environment interacts with a single two level system. We can identify three coupling regimes:

- ↔ Individual mode coupling: The qubit couples strongly with a single resonator mode with a coupling strength  $g$  smaller than the free spectral range  $\Delta\omega$ .
- ↔ Multimode coupling: For a coupling strength  $g$  that exceeds the free spectral range  $\Delta\omega$  ( $g > \Delta\omega$ ), the impurity can couple to several resonator modes at once.
- ↔ Ultra-strong multimode coupling: By pushing the coupling strength  $g$  to be comparable to the qubit transition frequency  $\omega_q$ , while maintaining  $g > \Delta\omega$ , the qubit can couple ultra-strongly to several resonator modes. The rotating wave approximation breaks down and the system must be described by the full Rabi Hamiltonian. For realisation of the spin boson model, the ultra-strong coupling regime must be reached. The ultra-strong coupling regime for a capacitively coupled artificial atom can be reached by making use of high-impedance resonators [7].

An integral part of quantum impurity modelling is engineering a suitable multimode environment. This multimode environment serves as the bosonic bath, which interacts with the (spin) qubit. This can be implemented by several approaches, such as using a superconducting long coplanar waveguide resonator [8], photonic crystals [9] or coupled cavity arrays [10]. Such metamaterials allow for flexible and precise engineering of the mode spectrum, making them a promising platform for analog quantum simulation [11, 12].

In this thesis, a specific type of metamaterial, namely a capacitively coupled resonator array, is investigated. The building block of the metamaterial is hence a superconducting lumped-element LC resonator.

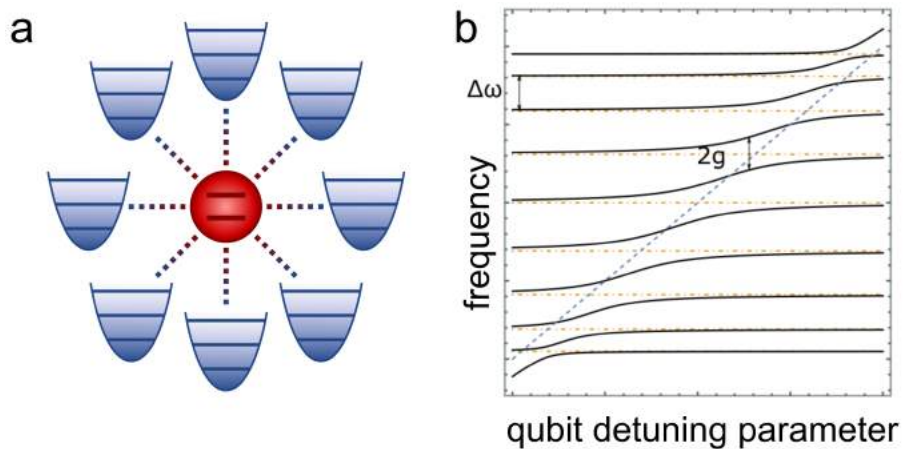


**Fig. 1.1: Multimode Coupling.** a) Schematic of multimode bosonic environment, depicted as several harmonic oscillators (blue), coupled to a qubit (red). b) Spectrum of multimode bosonic environment, with free spectral range  $\Delta\omega$  and coupling strength  $g$  with the qubit.

The outline of the thesis is as follows:

- ↪ Section 2 provides the basis for understanding the physics of coupled resonator arrays, starting with one parallel RLC Resonator in Section 2.1. The description is then extended to two hybridised resonators (Section 2.2) and arrays (Section 2.3). It is also explained why the high kinetic inductance of the metamaterial makes it an exciting platform in Section 2.4.
- ↪ In Section 3, it is described how the devices were designed (Section 3.1), simulated (Section 3.2 and fabricated (Section 3.3). The (cryogenic) measurement setup, as well as the fitting procedure are presented in Section 3.4 and Section 3.5, respectively.
- ↪ Section 4 is dedicated to modelling of the metamaterial. The metamaterial was modelled using a circuit model, a tight-binding model and the software Sonnet. The main findings for both dimer (Section 4.1) and array (Section 4.2) simulations are presented.
- ↪ Section 5 summarises the principal experimental results obtained during the thesis. After a characterisation of the implemented lumped-element resonators in Section 5.1, the focus lies on the coupled resonator arrays in Section 5.2. The measurements are also compared to simulations in Section 5.2.3.
- ↪ Section 6 draws a conclusion from the results produced during the thesis.
- ↪ Lastly, Section 7 provides an outlook on on-going research, stemming from the insights obtained from the thesis results.

## 2 Coupled Resonator Arrays

The metamaterial studied in this thesis is built from superconducting lumped-element resonators, which are capacitively coupled to each other. In this section, the vocabulary and general equations for treating such a coupled resonator array are presented. In Section 2.1, the building block of the metamaterial, a parallel RLC resonator, is introduced. It is explained how one can measure its properties in subsection 2.1.1. In the next section 2.2, two coupled resonators and their transmission spectrum are discussed. The study is extended to coupled resonator arrays in Section 2.3, where two different models are introduced for modelling such an array: The ABCD-Matrix approach (see Section 2.3.1) and derivation of the Hamiltonian from the Lagrangian (see Section 2.3.2). In Section 2.3.2, it is also briefly explained how this Hamiltonian follows the Su-Schrieffer-Heeger model and its terminology is acquainted. Lastly, in Section 2.4, one important material property of the investigated coupled resonator array is presented, namely its high kinetic inductance.

### 2.1 Parallel RLC Resonator

The building block of our metamaterial is a superconducting, lumped-element resonator. In microwave circuitry, a lumped element is defined as a passive component with a size such that there is a negligible phase shift of voltage and current across the element from input to output. The lumped element approximation holds well for a maximal dimension size less than  $\lambda/20$ , where  $\lambda$  is the wavelength of the applied microwave signal [13]. An important characteristic in analysis of (microwave) circuits is the impedance  $Z$ , which was originally defined as the complex ratio between voltage  $V$  and current  $I$  in lumped AC circuits [14].

Near resonance, the building block of our metamaterial can be modelled as a parallel RLC resonator (see Fig. 2.1). The input impedance of this circuit is

$$Z_{\text{in}} = \left( \frac{1}{Z_R} + \frac{1}{Z_L} + \frac{1}{Z_C} \right)^{-1} = \left( \frac{1}{R} + \frac{1}{i\omega L} + i\omega C \right)^{-1} \quad (2.1)$$

at an angular frequency  $\omega$ , for a resistance  $R$ , an inductance  $L$  and a capacitance  $C$  [14]. For amplitudes  $|I|, |V| \neq 0$ , the resistance  $R$  of the circuit dissipates the power

$$P_{\text{loss}} = \frac{1}{2} \frac{|V|^2}{R}. \quad (2.2)$$

On the other hand, the capacitor stores, on time-average, the electric energy

$$W_{\text{el}} = \frac{1}{4} |V|^2 C \quad (2.3)$$

and the inductor the average magnetic energy

$$W_{\text{mag}}(\omega) = \frac{1}{4} |I_L|^2 L = \frac{1}{4} |V|^2 \frac{1}{\omega^2 L}, \quad (2.4)$$

with the current flowing through the inductor as  $|I_L| = \frac{1}{\omega L} |V|$ , using  $V = L \frac{dI_L}{dt}$  for  $V \propto \sin \omega t$ . The two energies in Eqs. (2.3) and (2.4) are equal at resonance  $\omega = \omega_r$  [14, 15]. The resonance frequency  $f_r = \omega_r / (2\pi)$  is thus given by

$$\begin{aligned} W_{\text{el}} &= W_{\text{mag}}(\omega = \omega_r) \\ \frac{1}{4} |V|^2 C &= \frac{1}{4} |V|^2 \frac{1}{\omega_r^2 L} \\ \omega_r &= \frac{1}{\sqrt{LC}} \quad \Longleftrightarrow \quad f_r = \frac{1}{2\pi \sqrt{LC}}. \end{aligned} \quad (2.5)$$

Aside from the resonance frequency  $f_r$ , the quality factor  $Q$ <sup>1</sup> is another important parameter to characterise a resonant circuit. It is defined as

$$Q = \omega \frac{\text{average energy stored}}{\text{energy loss per cycle}} = \frac{f_r}{\Delta f}, \quad (2.6)$$

where  $\Delta f$  denotes the linewidth or full width at half maximum (FWHM) of the resonance curve [14, 16]. A resonance curve in transmission is plotted in Fig. 2.1. The FWHM  $\Delta f$  is also called decay rate  $\kappa$  and is an equivalent measure of losses. From Eq. (2.6) we note that the decay rate is thus given by  $\kappa = f_r / Q$ .

<sup>1</sup>Apparently, K.S. Johnson was the first one to attribute the letter of Q to this ratio, before it was even named “quality factor”. He chose Q because it was the only letter of the alphabet left without a meaning assigned. The term “quality factor” was later introduced by V.E. Legg and prevailed. The whole story can be read in Ref. [16].

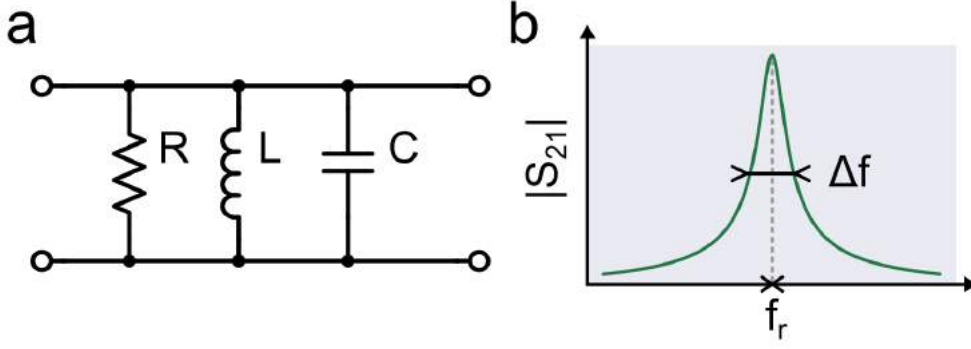


**Fig. 2.1: Parallel RLC Resonator.** a) Circuit schematic of a parallel RLC resonator. The resonator has an inductance  $L$ , capacitance  $C$  and resistance  $R$ . b)  $S_{21}$  transmission amplitude of a parallel RLC resonator. Its shape follows a Lorentzian and reaches its maximum at resonance frequency  $f_r$ . The FWHM  $\Delta f$  is marked.

The higher the quality factor of a resonator, the lower are its losses. Internal, i.e. intrinsic, losses of a resonator may be conductor losses, dielectric losses or radiation losses and are modelled by the resistance  $R$  - which is why a resistance is included in the model, even though the resonator itself is superconducting. For a parallel RLC resonator, this internal or unloaded quality factor  $Q_i$  reads

$$Q_i = \omega_r \frac{W_{\text{el}} + W_{\text{mag}}(\omega = \omega_r)}{P_{\text{loss}}} \stackrel{(2.2-2.4)}{=} \omega_r \frac{1/2 \left( C + \frac{1}{\omega_r^2 L} \right)}{1/R} = \omega_r R C = \frac{R}{\omega_r L}, \quad (2.7)$$

with  $\frac{1}{\omega_r^2 L} = C$  from Eq. (2.5) [14]. However, a resonator is commonly coupled to an external circuit in order to measure its spectrum. For a parallel RLC, this is captured by connecting an external load resistance  $R_{\text{ext}}$  in parallel (see Fig. 2.2). The total resistance is then

$$R_{\text{tot}} = \left( \frac{1}{R} + \frac{1}{R_{\text{ext}}} \right)^{-1} = \frac{R R_{\text{ext}}}{R_{\text{ext}} + R}. \quad (2.8)$$

The total or loaded quality factor  $Q_L$  is then given by replacing  $R$  by  $R_{\text{tot}}$  in Eq. (2.7)

$$Q_L = \frac{R_{\text{tot}}}{\omega_r L} = \frac{R R_{\text{ext}}}{(R_{\text{ext}} + R) \omega_r L}. \quad (2.9)$$

The internal and loaded quality factor are linked by

$$\frac{1}{Q_L} = \frac{1}{Q_i} + \frac{1}{Q_c}, \quad (2.10)$$

where the external or coupling quality factor  $Q_c$  accounts for losses due to coupling to the environment. From Eqs. (2.7) and (2.9) it follows that

$$Q_c = \frac{R_{\text{ext}}}{\omega_r L}. \quad (2.11)$$

Analogously, losses can be quantified using the internal decay rate  $\kappa_i$ , the total decay rate  $\kappa_L$  and the coupling rate to the environment  $\kappa_c$ . Combining Eq. (2.6) with Eqs. (2.7), (2.9) and (2.11) it follows that

$$\kappa_i = \frac{2\pi f_r^2 L}{R}, \quad \kappa_L = \frac{2\pi f_r^2 L}{R_{\text{tot}}}, \quad \kappa_c = \frac{2\pi f_r^2 L}{R_{\text{ext}}}. \quad (2.12)$$

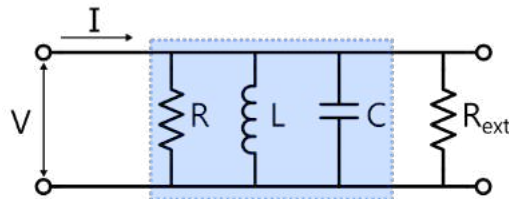


**Fig. 2.2: Circuit Schematic of a Loaded RLC Resonator.** The RLC unit is shaded in grey. An external load resistance  $R_{\text{ext}}$  is connected in parallel to the resonator.

### 2.1.1 Transmission Spectrum of Hanged Resonator

The quality factors of a resonator can be extracted by measuring it either in transmission, reflection or in hanged mode (see Fig. 2.3). The drawback of the transmission configuration is that it requires an additional recording of the transmission baseline to calibrate unity transmission through the system. This calibration is needed because cable and resonator loss cannot be distinguished in transmission mode and this limits the accuracy of quality factor extraction [17, 18]. In reflection mode, there is no need for this calibration, however, a non-reciprocal element such as a circulator is required to re-direct the reflected signal to an output port, to prevent signal going back to the input port. On the other hand, the hanged configuration provides the possibility of measuring several resonators in one run. They can all be placed on the same feedline, granted they have distinct resonance frequencies. This configuration also allows straightforward extraction of the quality factors, without calibration [17].

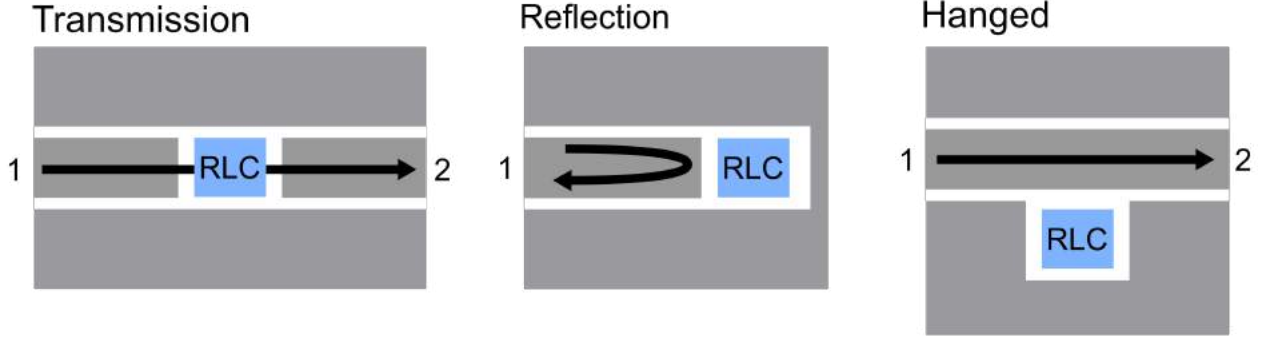


**Fig. 2.3: Three Types of Resonator Measurement.** Transmission: The resonator is coupled to an input and an output feedline on each side. Reflection: The resonator is probed by coupling it to one end of the feedline. Hanged: The resonator couples to a feedline whose transmission is measured.

To characterise our resonators, we measured them in the hanged configuration. In the ideal case, where there is no impedance mismatch and the background signal is completely flat [17], the measurement setup is described by the circuit schematic in Fig. 2.4. The parallel RLC resonator is coupled to the waveguide with impedance  $Z_0$  via a coupling capacitance  $C_c$ .

Applying Kirchhoff's voltage law for both loops and Kirchhoff's current law, we have

$$V_s = Z_0 I_1 + I_3 Z_r \quad (2.13)$$

$$Z_0 I_2 = Z_r I_3 \iff I_2 = \frac{Z_r}{Z_0} I_3 \quad (2.14)$$

$$I_1 = I_2 + I_3 \quad (2.15)$$

and from the schematic in Fig. 2.4,

$$V_2 = Z_0 I_2. \quad (2.16)$$

The transmission from port 1 to port 2 is then given by the scattering parameter  $S_{21}$ , which is defined as [19]

$$S_{21} = \frac{2V_2}{V_s} \stackrel{(2.13, 2.16)}{=} \frac{2Z_0 I_2}{Z_0 I_1 + I_3 Z_0} \stackrel{(2.15)}{=} \frac{2Z_0 I_2}{Z_0(I_2 + I_3) + I_3 Z_r} \stackrel{(2.14)}{=} \frac{2Z_r I_3}{Z_0(Z_r/Z_0 + 1)I_3 + Z_r I_3} = \frac{2}{2 + Z_0/Z_r} \quad (2.17)$$

where the resonator and its coupling capacitance  $C_c$  to the feedline are combined to form the impedance  $Z_r$ :

$$Z_r = Z_{RLC} + Z_c \stackrel{(2.1)}{=} \left( \frac{1}{R_r} + \frac{1}{i\omega L_r} + i\omega C_r \right)^{-1} + \frac{1}{i\omega C_c}. \quad (2.18)$$



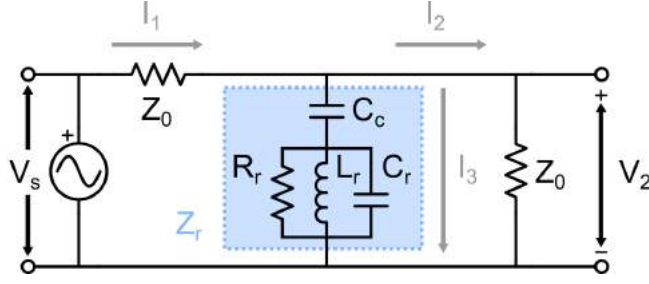


**Fig. 2.4: Circuit Schematic in Hanged Configuration.** A LC Resonator ( $L_r, C_r$ ) capacitively coupled with coupling capacitance  $C_c$  to the feedline with impedance  $Z_0$ . Losses in the resonator are modelled with the resistance  $R_r$ . Inspired by [17].

For this configuration, the internal quality factor  $Q_i$  and the coupling quality factor  $Q_c$  can be expressed as

$$Q_i = \frac{\omega_r}{R_r(C_r + C_c)} \quad (2.19)$$

$$Q_c = \frac{C_r + C_c}{\omega_r Z_0 C_c^2}, \quad (2.20)$$

where  $\omega_r = 1/\sqrt{L_r(C_r + C_c)}$  [20].

## 2.2 Hybridised Resonators

On the way to realising coupled resonator arrays, the simplest case is a dimer, i.e. two coupled resonators. They can either couple inductively or capacitively. All metamaterials discussed within this thesis rely on capacitive coupling. A typical transmission amplitude profile of a dimer is plotted in Fig. 2.5. The two resonators hybridise and their spectrum shows two Lorentzian peaks. The splitting between the two peaks is given by two times the coupling rate  $J$  between the resonators.

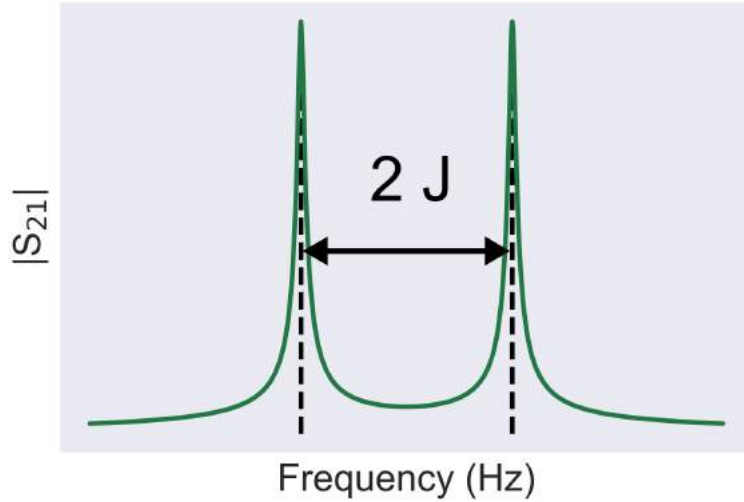


**Fig. 2.5: Transmission Spectrum of a Resonator Dimer.** Two coupled resonators have a transmission spectrum consisting of two peaks, separated by  $2J$ , where  $J$  is the coupling rate.

## 2.3 Theoretical Models of A Coupled Resonator Array

The coupled resonator arrays are theoretically modelled as a lumped-element circuit. First, the ABCD matrix formalism is introduced. Second, the Lagrangian for the system is derived and mapped to the tight-binding Hamiltonian.

### 2.3.1 ABCD Matrix

For a two-port microwave device, one can define the 2x2 transmission - or ABCD - Matrix. It links the in-flowing current  $I_1$  and voltage  $V_1$  on port 1 to out-flowing current  $I_2$  and voltage  $V_2$  on port 2 [14]:

$$\begin{pmatrix} V_1 \\ I_1 \end{pmatrix} = \begin{pmatrix} A & B \\ C & D \end{pmatrix} \begin{pmatrix} V_2 \\ I_2 \end{pmatrix} \quad (2.21)$$

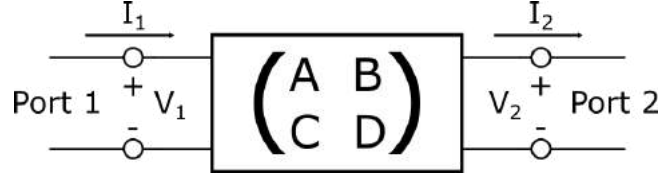


**Fig. 2.6: Simplest ABCD Model.** The impedance of the circuit is described by the ABCD Matrix, which connects ports 1 and 2.

The convenience of the ABCD formalism lies in its straight-forward extension to a cascade of microwave circuits in series or parallel (see Fig. 2.7). For obtaining the total ABCD matrix  $M_{\text{tot}}$  of a system with  $N$  circuits, one multiplies the ABCD matrices for each circuit  $M_i$  in the order of their arrangement:

$$M_{\text{tot}} = M_1 \cdot M_2 \cdot M_3 \cdots M_N$$

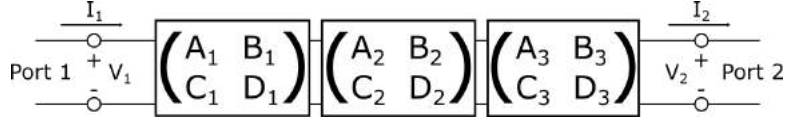


**Fig. 2.7: Multiple Circuits with the ABCD Model.** The three matrices describe circuits which are connected in series or parallel with each other and to the two ports 1,2.

Following this logic, one can construct  $M_{\text{tot}}$  for a LC resonator dimer, capacitively coupled to the ports (see Fig. 2.8). Using that the impedances  $Z$  of a capacitor  $C$ ,  $Z_C$ , and an inductor  $L$ ,  $Z_L$ , are given by

$$Z_C = \frac{1}{i\omega C} \quad (2.22)$$

$$Z_L = i\omega L, \quad (2.23)$$

as well as the fact that impedances in parallel can be added up as  $Z_\Sigma = (\sum_k 1/Z_k)^{-1}$ , the ABCD matrices for the three different circuit elements (see Fig. 2.8) can be constructed:

$$M_c = \begin{pmatrix} 1 & Z_{C_c} \\ 0 & 1 \end{pmatrix} = \begin{pmatrix} 1 & \frac{1}{i\omega C_c} \\ 0 & 1 \end{pmatrix}, \quad M_i = \begin{pmatrix} 1 & Z_{C_i} \\ 0 & 1 \end{pmatrix} = \begin{pmatrix} 1 & \frac{1}{i\omega C_i} \\ 0 & 1 \end{pmatrix} \quad (2.24)$$

$$M_r = \begin{pmatrix} 1 & 0 \\ 1/Z_{C_r} + 1/Z_{L_r} & 1 \end{pmatrix} = \begin{pmatrix} 1 & 0 \\ i\omega C_r + \frac{1}{i\omega L_r} & 1 \end{pmatrix}. \quad (2.25)$$

The parameters are the coupling capacitance  $C_c$  to the feedline, the coupling capacitance between the two resonators  $C_i$ , and self-capacitance  $C_r$  and self-inductance  $L_r$  of the resonator. The ABCD matrix for the dimer is then given by

$$M_{\text{tot}} = M_c \cdot M_r \cdot M_i \cdot M_r \cdot M_c. \quad (2.26)$$

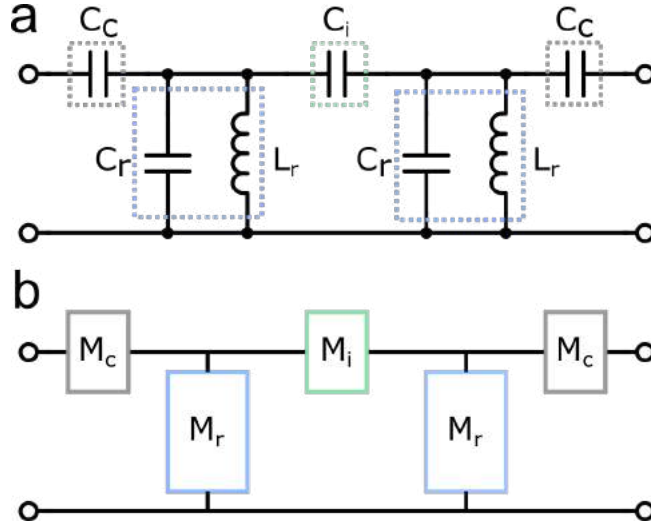


**Fig. 2.8: ABCD model for a LC resonator dimer.** a) Circuit schematic of the LC dimer. b) Schematic in the ABCD formalism, where each circuit element is modelled as an ABCD Matrix  $M$  in series or parallel.

Analogously, the system can be extended to  $N$  (dimeric) unit cells (see Fig. 2.9):

$$M_{N-\text{Array}} = M_c \cdot (M_{uc} \cdot M_x)^{N-1} \cdot M_{uc} \cdot M_c, \quad (2.27)$$

$$\text{with } M_{uc} = M_r \cdot M_i \cdot M_r \quad \text{and} \quad M_x = \begin{pmatrix} 1 & Z_{C_x} \\ 0 & 1 \end{pmatrix} = \begin{pmatrix} 1 & \frac{1}{i\omega C_x} \\ 0 & 1 \end{pmatrix}.$$

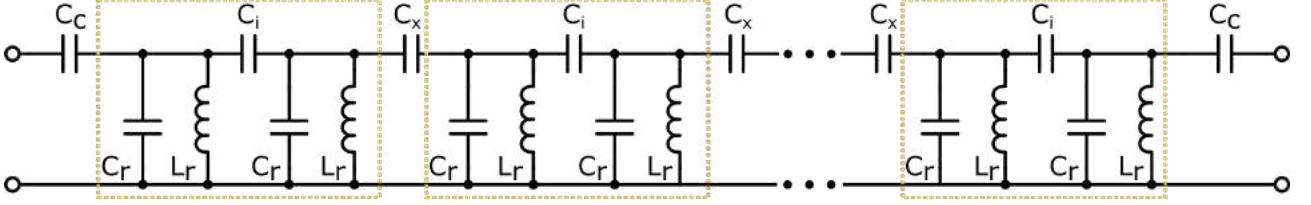


**Fig. 2.9: ABCD model for a left-handed LC Resonator Array with  $N$  unit cells.** The dimeric unit cells are framed in dotted yellow. The first and last unit cell are connected to the ports via a capacitance  $C_c$ . Each unit cell has an internal coupling capacitance  $C_i$ . The unit cells are capacitively coupled to each other with a coupling capacitance  $C_x$ .

### $S_{21}$ spectrum

Once the ABCD matrix of the system is determined, the (complex) transmission spectrum  $S_{21}$  from port 1 to port 2 can be calculated with the entries of the matrix  $M = \begin{pmatrix} A & B \\ C & D \end{pmatrix}$  and the port impedance  $Z_0$  [14]:

$$S_{21} = \frac{2}{A + B/Z_0 + CZ_0 + D}. \quad (2.28)$$

### Dispersion relation

In the limit of an infinite array, with unit cell number  $N \rightarrow \infty$ , the dispersion relation can be calculated using that in one unit cell of index  $n$ , the in- and out-going voltages and current are linked by the ABCD matrix of the unit cell,  $M_{uc}$ :

$$\begin{pmatrix} V_n \\ I_n \end{pmatrix} = M_{uc} \begin{pmatrix} V_{n+1} \\ I_{n+1} \end{pmatrix} = \begin{pmatrix} A_{uc} & B_{uc} \\ C_{uc} & D_{uc} \end{pmatrix} \begin{pmatrix} V_{n+1} \\ I_{n+1} \end{pmatrix} \quad (2.29)$$

with  $M_{uc}$  of Eq. (2.27). The voltage and current at unit cell  $n$  can be expressed as

$$V_n = V_0^+ e^{-ikna} \quad (2.30)$$

$$I_n = I_0^+ e^{-ikna}, \quad (2.31)$$

assuming that they only propagate in positive  $z = na$  direction, with unit cell length  $a$  [14, 21]. Hence, the out-going voltage  $V_{n+1}$  and current  $I_{n+1}$  pick up a propagation factor  $e^{-ika}$ :

$$V_{n+1} = V_n e^{-ika} \iff V_n = V_{n+1} e^{ika} \quad (2.32)$$

$$I_{n+1} = I_n e^{-ika} \iff I_n = I_{n+1} e^{ika} \quad (2.33)$$

Inserting Eqs. (2.32) and (2.33) in Eq. (2.29) results in

$$\begin{pmatrix} V_{n+1} e^{ika} \\ I_{n+1} e^{ika} \end{pmatrix} = \begin{pmatrix} A_{uc} & B_{uc} \\ C_{uc} & D_{uc} \end{pmatrix} \begin{pmatrix} V_{n+1} \\ I_{n+1} \end{pmatrix} \quad (2.34)$$

$$\iff 0 = \underbrace{\begin{pmatrix} A_{uc} - e^{ika} & B_{uc} \\ C_{uc} & D_{uc} - e^{ika} \end{pmatrix}}_{\tilde{M}} \begin{pmatrix} V_{n+1} \\ I_{n+1} \end{pmatrix}. \quad (2.35)$$

This system of equations has a solution with wave vector  $k(\omega)$  if the determinant of  $\tilde{M}$  is equal to zero. If the determinant of  $\tilde{M}$  were not equal to zero, the system of equation would have one definite solution for  $V_{n+1}, I_{n+1}$ . More precisely, the system of equation would only have the trivial solution  $V_{n+1}, I_{n+1} = 0$ , which is not what we are looking for. Thus,

$$\begin{aligned} \det \tilde{M} &= (A_{uc} - e^{ika})(D_{uc} - e^{ika}) - B_{uc}C_{uc} \stackrel{!}{=} 0 \\ \iff A_{uc}D_{uc} - (A_{uc} + D_{uc})e^{ika} + e^{2ika} - B_{uc}C_{uc} &= 0 \\ \iff 1 - (A_{uc} + D_{uc})e^{ika} + e^{2ika} &= 0 \end{aligned} \quad (2.36)$$

$$\iff e^{-ika} + e^{ika} = A_{uc} + D_{uc} \quad (2.37)$$

$$\iff 2 \cos(ka) = A_{uc} + D_{uc} = \text{Tr}(M_{uc}) \quad (2.38)$$

$$(2.39)$$

where we used that  $\det M = AD - BC = 1$  for any ABCD matrix  $M$  [14],  $2 \cos(ka) = e^{-ika} + e^{ika}$  and the trace ( $\text{Tr}$ ) of a matrix is given by the sum of its diagonal elements. The dispersion relation thus reads

$$\cos(ka) = \frac{1}{2} \text{Tr}(M_{uc}) \iff k(\omega) = \frac{1}{a} \arccos\left(\frac{1}{2} \text{Tr}(M_{uc})\right) \quad (2.40)$$

for a given unit cell ABCD matrix  $M_{uc}$ .

### 2.3.2 Lagrangian Formalism

One can also model the coupled resonator array by deriving the Lagrangian of the system. The schematic in Fig. 2.10 represents an overview on the variables. The voltage at each LC resonator ( $L_r, C_r$ ) is denoted by  $V_n^S$ , where  $n \in \{1, 2, \dots, N\}$  stands for the unit cell index and  $S \in \{A, B\}$  is the site index. The resonators are arranged in dimeric unit cells, with intra-cell coupling capacitance  $C_i$  and capacitance  $C_x$  between two unit cells. The first and the last resonator of the chain are coupled to the ports with a capacitance  $C_c$ .

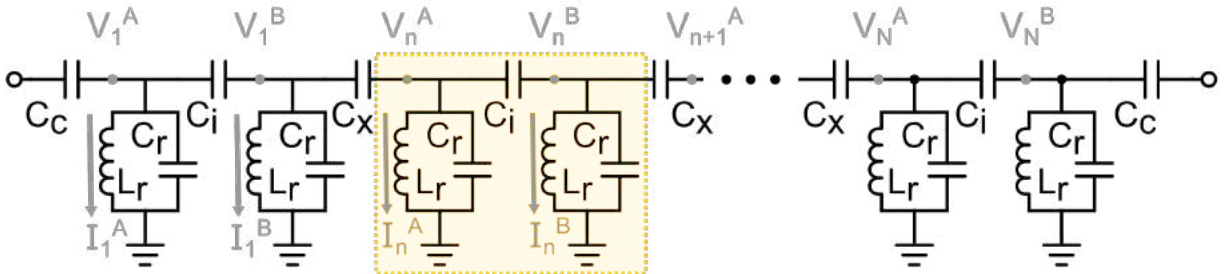


**Fig. 2.10: Circuit Model of Capacitively Coupled Resonator Array.** A unit cell is highlighted in yellow. The first and last unit cell are connected to the ports via a capacitance  $C_c$ . Each unit cell has an internal coupling capacitance  $C_i$ . The unit cells are capacitively coupled to each other with a coupling capacitance  $C_x$ . Each resonator has a capacitance  $C_r$  and an inductance  $L_r$ . The voltages  $V_n^S$  and currents  $I_n^S$  used in derivation are labelled.

To write down the Lagrangian of the whole system, we first determine the Lagrangian for one unit cell, highlighted by the yellow box in Fig. 2.10. The total potential energy stored on the capacitors of unit cell  $n$

is

$$E_{C,n} = \frac{1}{2} \left[ C_i (V_n^B - V_n^A)^2 + C_x (V_{n+1}^A - V_n^B)^2 + C_r (V_n^A)^2 + C_r (V_n^B)^2 \right], \quad (2.41)$$

while the kinetic energy in the inductors is equal to

$$E_{L,n} = \frac{L_r}{2} \left[ (I_n^A)^2 + [(I_n^B)^2] \right]. \quad (2.42)$$

Now, the kinetic energy of the inductors can also be expressed in terms of the magnetic flux through them with Faraday's law,  $I_n^S = L_r \Phi_n^S$ . By defining the flux variable  $\Phi$  as

$$\begin{aligned} \Phi_n^S &\equiv \int_{-\infty}^t V_n^S(\tau) d\tau \Rightarrow \dot{\Phi}_n^S = V_n^S \\ S &\in \{A, B\}, \quad n \in \{1, 2, \dots, N\}, \end{aligned} \quad (2.43)$$

the Lagrangian  $\mathcal{L}_n = E_{C,n} - E_{L,n}$  reads

$$\mathcal{L}_n = \frac{1}{2} \left[ C_i (\dot{\Phi}_n^B - \dot{\Phi}_n^A)^2 + C_x (\dot{\Phi}_{n+1}^A - \dot{\Phi}_n^B)^2 + C_r (\dot{\Phi}_n^A)^2 + C_r (\dot{\Phi}_n^B)^2 \right] - \frac{1}{2L_r} \left[ (\Phi_n^A)^2 + [(\Phi_n^B)^2] \right] \quad (2.44)$$

where the capacitive energy plays the role of the kinetic energy (because it contains the time derivative of term variable  $\Phi_n^S$ ) and the inductive energy assumes the form of a potential energy [11, 22].

This Lagrangian for the unit cell may also be written in matrix form [12] as

$$\mathcal{L}_n = \frac{1}{2} \dot{\Phi}^T [\mathbf{C}_n] \dot{\Phi} - \frac{1}{2} \Phi^T [\mathbf{L}_n] \Phi \quad (2.45)$$

with the vectors  $\dot{\Phi}^T = (\dot{\Phi}_n^A, \dot{\Phi}_n^B, \dot{\Phi}_{n+1}^A)$ ,  $\Phi^T = (\Phi_n^A, \Phi_n^B, \Phi_{n+1}^A)$ , the capacitance matrix  $[\mathbf{C}_n]$

$$[\mathbf{C}_n] = \begin{pmatrix} C_i + C_r & -C_i & 0 \\ -C_i & C_i + C_r + C_x & -C_x \\ 0 & -C_x & C_x \end{pmatrix} \quad (2.46)$$

and the inductance matrix  $[\mathbf{L}_n]$

$$[\mathbf{L}_n] = \frac{1}{L_r} \begin{pmatrix} 1 & 0 & 0 \\ 0 & 1 & 0 \\ 0 & 0 & 0 \end{pmatrix}. \quad (2.47)$$

The system Lagrangian is then given by summing Eq. (2.44) over all  $N$  unit cells. It is assumed that  $C_c = C_x$  in the following. This configuration is also implemented in the measured resonator arrays and simplifies the calculation. The system Lagrangian in matrix form thus reads

$$\mathcal{L}_{\text{sys}} = \frac{1}{2} \dot{\Phi}^T [\mathbf{C}] \dot{\Phi} - \frac{1}{2} \Phi^T [\mathbf{L}] \Phi \quad (2.48)$$

with the vector  $\dot{\Phi}^T = (\dot{\Phi}_1^A, \dot{\Phi}_1^B, \dot{\Phi}_2^A, \dot{\Phi}_2^B, \dots, \dot{\Phi}_N^A, \dot{\Phi}_N^B)$  (analogously for  $\Phi$ ). The capacitance matrix can be written down as

$$[\mathbf{C}] = \begin{pmatrix} C_\Sigma & -C_i & 0 & 0 & 0 & 0 & \dots & 0 & 0 & 0 & 0 \\ -C_i & C_\Sigma & -C_x & 0 & 0 & 0 & \dots & 0 & 0 & 0 & 0 \\ 0 & -C_x & C_\Sigma & -C_i & 0 & 0 & \dots & 0 & 0 & 0 & 0 \\ 0 & 0 & -C_i & C_\Sigma & -C_x & 0 & \dots & 0 & 0 & 0 & 0 \\ \vdots & \vdots & 0 & \ddots & \ddots & \ddots & \ddots & 0 & 0 & 0 & 0 \\ \vdots & \vdots & \vdots & 0 & \ddots & \ddots & \ddots & \ddots & 0 & 0 & 0 \\ \vdots & \vdots & \vdots & \vdots & 0 & \ddots & \ddots & \ddots & \ddots & 0 & 0 \\ \vdots & \vdots & \vdots & \vdots & \vdots & 0 & \ddots & \ddots & \ddots & 0 & 0 \\ \vdots & \vdots & \vdots & \vdots & \vdots & \vdots & \ddots & \ddots & \ddots & -C_x & 0 \\ 0 & 0 & 0 & 0 & 0 & 0 & \dots & 0 & -C_x & C_\Sigma & -C_i \\ 0 & 0 & 0 & 0 & 0 & 0 & \dots & 0 & 0 & -C_i & C_\Sigma \end{pmatrix} \quad (2.49)$$

with  $C_\Sigma = C_i + C_r + C_x$ . Analogously, the inductance matrix of the system is then

$$[\mathbf{L}] = \frac{1}{L_r} \begin{pmatrix} 1 & 0 & \cdots & \cdots & \cdots & 0 \\ 0 & 1 & 0 & \cdots & \cdots & 0 \\ \vdots & 0 & \ddots & \ddots & \cdots & 0 \\ \vdots & \vdots & \ddots & \ddots & 0 & 0 \\ \vdots & \vdots & \vdots & \ddots & 1 & 0 \\ 0 & 0 & 0 & \cdots & 0 & 1 \end{pmatrix} \quad (2.50)$$

In order to calculate the Hamiltonian from the Lagrangian, one introduces the charge variables  $Q_n^S$ , which play the role of canonical momenta (while the flux variables  $\Phi_n^S$  represent position):

$$\mathbf{Q} = \frac{\partial \mathcal{L}}{\partial \dot{\Phi}} \quad (2.51)$$

with  $\mathbf{Q}^T = (Q_1^A, Q_1^B, \dots, Q_N^A, Q_N^B)$ .

For the given system, the charge variables are

$$Q_n^A = \begin{cases} C_\Sigma \dot{\Phi}_n^A - C_i \dot{\Phi}_n^B & \text{for } n = 1 \\ C_\Sigma \dot{\Phi}_n^A - C_i \dot{\Phi}_n^B - C_x \dot{\Phi}_{n-1}^B & \text{for } n \in \{2, 3, \dots, N\} \end{cases} \quad (2.52)$$

$$Q_n^B = \begin{cases} C_\Sigma \dot{\Phi}_n^B - C_i \dot{\Phi}_n^A - C_x \dot{\Phi}_{n+1}^A & \text{for } n \in \{1, 2, \dots, N-1\} \\ C_\Sigma \dot{\Phi}_n^B - C_i \dot{\Phi}_n^A & \text{for } n = N \end{cases} \quad (2.53)$$

or to write it in a more compact manner,  $\mathbf{Q} = [\mathbf{C}] \dot{\Phi}$ .

Making use of the matrix formalism yet again, the Hamiltonian  $\mathcal{H}$  then reads [12, 22]

$$\mathcal{H} = \frac{1}{2} \mathbf{Q}^T \mathbf{C}^{-1} \mathbf{Q} + \frac{1}{2} \Phi^T \mathbf{L} \Phi \quad (2.54)$$

The inverse of the capacitance matrix  $[\mathbf{C}^{-1}]$  can be determined analytically. This result can be simplified using the assumption that second order terms of  $C_i, C_x$  are negligible in comparison to  $C_r$ . This assumption is fulfilled in our system, with  $C_i, C_x \sim 1$  fF and  $C_r \sim 13$  fF. Thus, we put  $C_i^2, C_x, C_i C_x \approx 0$ . Under those assumptions, the inverse capacitance matrix can be expressed as

$$[\mathbf{C}^{-1}] = L_r \omega_r^2 \begin{pmatrix} 1 & \beta_i & 0 & 0 & 0 & 0 & \cdots & 0 & 0 & 0 & 0 \\ \beta_i & 1 & \beta_x & 0 & 0 & 0 & \cdots & 0 & 0 & 0 & 0 \\ 0 & \beta_x & 1 & \beta_i & 0 & 0 & \cdots & 0 & 0 & 0 & 0 \\ 0 & 0 & \beta_i & 1 & \beta_x & 0 & \cdots & 0 & 0 & 0 & 0 \\ \vdots & \vdots & 0 & \ddots & \ddots & \ddots & \ddots & 0 & 0 & 0 & 0 \\ \vdots & \vdots & \vdots & 0 & \ddots & \ddots & \ddots & \ddots & 0 & 0 & 0 \\ \vdots & \vdots & \vdots & \vdots & 0 & \ddots & \ddots & \ddots & \ddots & 0 & 0 \\ \vdots & \vdots & \vdots & \vdots & \vdots & 0 & \ddots & \ddots & \ddots & 0 & 0 \\ \vdots & \vdots & \vdots & \vdots & \vdots & \vdots & \ddots & \ddots & \ddots & \beta_x & 0 \\ 0 & 0 & 0 & 0 & 0 & 0 & \cdots & 0 & \beta_x & 1 & \beta_i \\ 0 & 0 & 0 & 0 & 0 & 0 & \cdots & 0 & 0 & \beta_i & 1 \end{pmatrix} \quad (2.55)$$

with the definitions

$$\omega_r^2 = \frac{1}{L_r} \cdot [\mathbf{C}^{-1}]_{jj} = \frac{1}{L_r} \cdot \frac{1}{C_\Sigma} \quad (2.56)$$

$$\beta_i = \frac{C_i}{C_\Sigma} \quad (2.57)$$

$$\beta_x = \frac{C_x}{C_\Sigma}. \quad (2.58)$$

Using Eq. (2.55), the system Hamiltonian reads

$$\begin{aligned}\mathcal{H} = & \frac{1}{2} \sum_{n=1}^N L_r \omega_r^2 \left[ (Q_n^A)^2 + (Q_n^B)^2 \right] + \frac{1}{L_r} \left[ (\Phi_n^A)^2 + (\Phi_n^B)^2 \right] + \\ & + \frac{L_r \omega_r^2 \beta_i}{2} \sum_{n=1}^N Q_n^A Q_n^B + Q_n^B Q_n^A + \frac{L_r \omega_r^2 \beta_x}{2} \sum_{n=1}^{N-1} Q_{n+1}^A Q_n^B + Q_n^B Q_{n+1}^A\end{aligned}\quad (2.59)$$

and can be quantized by promoting the charge and flux variable to operators that satisfy the commutation relation

$$[\hat{Q}_n^{S'}, \hat{\Phi}_m^S] = i\hbar \delta_{mn} \delta_{S'S} \quad (2.60)$$

where  $S', S \in \{A, B\}$  and  $m, n \in \{1, 2, \dots, N\}$ . Now the charge and flux can be written in terms of annihilation and creation operators:

$$\hat{Q}_n^A = \sqrt{\frac{\hbar}{2L_r \omega_r}} (\hat{a}_n^\dagger + \hat{a}_n) \quad (2.61)$$

$$\hat{Q}_n^B = \sqrt{\frac{\hbar}{2L_r \omega_r}} (\hat{b}_n^\dagger + \hat{b}_n) \quad (2.62)$$

$$\hat{\Phi}_n^A = i\sqrt{\frac{\hbar L_r \omega_r}{2}} (\hat{a}_n^\dagger - \hat{a}_n) \quad (2.63)$$

$$\hat{\Phi}_n^B = i\sqrt{\frac{\hbar L_r \omega_r}{2}} (\hat{b}_n^\dagger - \hat{b}_n) \quad (2.64)$$

Inserting Eqs. (2.61) to (2.64) into Eq. (2.59), one arrives at

$$\begin{aligned}\hat{\mathcal{H}}_{\text{sys}} = & \hbar \omega_r \sum_{n=1}^N (\hat{a}_n^\dagger \hat{a}_n + \hat{b}_n^\dagger \hat{b}_n) + \underbrace{\hbar J_i \sum_{n=1}^N (\hat{a}_n^\dagger \hat{b}_n + \hat{a}_n \hat{b}_n^\dagger)}_{\text{intra-cell coupling terms}} + \underbrace{\hbar J_x \sum_{n=1}^{N-1} (\hat{a}_{n+1}^\dagger \hat{b}_n + \hat{a}_{n+1} \hat{b}_n^\dagger)}_{\text{inter-cell coupling terms}}\end{aligned}\quad (2.65)$$

with frequency  $\omega_r$ , intra-cell coupling  $J_i$  and inter-cell coupling  $J_x$ :

$$\omega_r = \sqrt{\frac{1}{L_r C_\Sigma}} \quad (2.66)$$

$$J_i = \frac{\omega_r \beta_i}{2} = \frac{\omega_r C_i}{2C_\Sigma} \quad (2.67)$$

$$J_x = \frac{\omega_r \beta_x}{2} = \frac{\omega_r C_x}{2C_\Sigma}. \quad (2.68)$$

The constant term  $\hbar N \omega_r$  was dropped since it is only an energy offset. Moreover, the counter-rotating terms  $\hat{a}_n^\dagger \hat{b}_n^\dagger$  and  $\hat{a}_n \hat{b}_n$  were abandoned, following the rotating wave approximation. This approximation holds for coupling strengths  $J_i, J_x \ll \omega_r$  [11], which is fulfilled in our system. The couplings ( $J_i/2\pi, J_x/2\pi$ ) are around 100 MHz, while the resonance frequency  $\omega_r/2\pi$  is around 4.4 GHz.

The Hamiltonian can also be expressed in matrix form as

$$\mathcal{H}_{\text{sys}} = \hbar \mathbf{v}^\dagger [\mathbf{H}] \mathbf{v} \quad (2.69)$$

with  $\mathbf{v}^\dagger = (\hat{a}_1, \hat{b}_1, \dots, \hat{a}_N, \hat{b}_N)$ . The matrix  $[\mathbf{H}]$  assumes the form

$$[\mathbf{H}] = \begin{pmatrix} \omega_r & J_i & 0 & 0 & 0 & 0 & \cdots & 0 & 0 & 0 & 0 \\ J_i & \omega_r & J_x & 0 & 0 & 0 & \cdots & 0 & 0 & 0 & 0 \\ 0 & J_x & \omega_r & J_i & 0 & 0 & \cdots & 0 & 0 & 0 & 0 \\ 0 & 0 & J_i & \omega_r & J_x & 0 & \cdots & 0 & 0 & 0 & 0 \\ \vdots & \vdots & 0 & \ddots & \ddots & \ddots & \ddots & 0 & 0 & 0 & 0 \\ \vdots & \vdots & \vdots & 0 & \ddots & \ddots & \ddots & \ddots & 0 & 0 & 0 \\ \vdots & \vdots & \vdots & \vdots & 0 & \ddots & \ddots & \ddots & \ddots & 0 & 0 \\ \vdots & \vdots & \vdots & \vdots & \vdots & 0 & \ddots & \ddots & \ddots & \ddots & 0 \\ \vdots & \vdots & \vdots & \vdots & \vdots & \vdots & \ddots & \ddots & \ddots & J_x & 0 \\ 0 & 0 & 0 & 0 & 0 & 0 & \cdots & 0 & J_x & \omega_r & J_i \\ 0 & 0 & 0 & 0 & 0 & 0 & \cdots & 0 & 0 & J_i & \omega_r \end{pmatrix} \quad (2.70)$$

and its eigenvalues supply the energy spectrum of the resonator array. This Hamiltonian can also be derived in the tight-binding model, which is discussed in appendix A. Note that appendix A follows a more theoretical approach with units such that  $\hbar = 1$ , and by choosing  $\hbar\omega_r$  as the zero of energy.

For the following discussion, it is necessary to introduce the Su-Schrieffer-Heeger (SSH) model and its terminology. As its name suggest, the model was introduced in 1979 by Su, Schrieffer and Heeger [23]. The SSH model concerns itself with electrons hopping along a one-dimensional chain with alternating hopping amplitudes - hence describes a system such as the one presently discussed. A detailed treatment of the SSH model can be found in appendix A. Here, the main statements are briefly presented.

The dispersion relation is

$$\omega(k) = \omega_r \pm \sqrt{J_i^2 + J_x^2 + 2J_iJ_x \cos(ka)}, \quad k = \frac{2\pi n}{Na} \quad (2.71)$$

where  $a$  is the unit cell length and  $n \in \{-N/2, \dots, N/2\}$  with  $N$  being the number of unit cells. For  $J_x \neq J_i$ , the dispersion relation has two frequency passbands. The upper passband is described by Eq. (2.71) with plus sign, while the lower passband is described using the minus sign in the same equation [11].

In the SSH model, three different coupling configurations can be distinguished:

- $\hookrightarrow$   $\mathbf{J}_i > \mathbf{J}_x$ : The intra-cell coupling is larger than the inter-cell coupling. The frequency spectrum has two passbands, separated by a middle band gap of  $2|J_i - J_x|$ . This regime is called **trivial**.
- $\hookrightarrow$   $\mathbf{J}_i = \mathbf{J}_x$ : Intra- and inter-cell coupling are equal, there is one passband. We further refer to this configuration as **normal**.
- $\hookrightarrow$   $\mathbf{J}_i < \mathbf{J}_x$ : The inter-cell coupling is larger than the intra-cell coupling. The frequency spectrum has two passbands, with a middle band gap of  $2|J_i - J_x|$  in between. In this gap, two almost-zero energy states are available. Those are the symmetric and anti-symmetric superposition of a left and right edge state. These edge states are localised at the two ends of the array and decay exponentially to the middle of the array. The left edge state only has occupancy on the first resonator of each unit cell, while the right edge states only resides on the second resonator of each unit cell. The edge states have an overlap on the order of  $e^{-(N-1)/\zeta}$  with localisation length  $\zeta = 1/\ln(J_x/J_i)$  [24]. Henceforth, the hybridised edge modes are abbreviated as **HEM**. Their splitting is proportional to  $(J_i/J_x)^N$  [25] and decays for increasing unit cell number  $N$ , since  $J_i/J_x < 1$ . This configuration is called the **topological** regime. The trivial and topological regimes can be topologically distinguished (see appendix A), hence the name.

To observe such edge state physics, the resonators must all have the same bare resonance frequency  $\omega_r$  [11].

## 2.4 High Kinetic Inductance

As mentioned in the introduction (Section 1), it is crucial to attain a high coupling strength  $g$  between bosonic environment and qubit. The coupling strength  $g$  scales with the zero-point voltage fluctuations  $V_{\text{rms}}$ . For a resonator with fundamental frequency  $f_0$ , the zero-point voltage fluctuations  $V_{\text{rms}}$  are proportional to  $f_0\sqrt{Z_r}$ , with characteristic impedance  $Z_r = \sqrt{L_\ell/C_\ell}$  [26]. It is thus desirable to increase the inductance per unit length



$L_\ell$  and decrease the capacitance per unit length  $C_\ell$ . In superconducting resonators, the characteristic impedance can be pushed by increasing the kinetic inductance  $L_k$ . As its name hints, the kinetic inductance originates from the kinetic energy of the Cooper pairs [27]. High kinetic inductance can be reached by using disordered thin superconducting films like NbN, the material chosen for this thesis. Disordered superconducting thin films, exhibiting a kinetic inductance  $L_k$ , also present a non-negligible non-linearity in the circulating current  $I$ :

$$L_k = L_{k,\text{lin}} \left( 1 + \left( \frac{I}{I_*} \right)^2 \right) \quad (2.72)$$

$$\text{with } L_{k,\text{lin}} = \frac{\hbar R_n}{\pi \Delta_0}, \quad (2.73)$$

where  $I_*$  is of the order of the critical current,  $R_n$  is the normal state resistance and  $\Delta_0 = k_B T_c$  is the superconducting energy gap, with critical temperature  $T_c$  and Boltzmann constant  $k_B$  [27–29]. Due to their non-linear kinetic inductance, the coupled resonator arrays from thin-film NbN are expected to behave differently depending on the drive power. This is why a power sweep was recorded for each measured resonator array. The high kinetic inductance, and thus high impedance, of thin-film NbN allows for very compact resonator designs. For instance, in our case, the resonator spans 50  $\mu\text{m}$  while still having a resonance frequency in the GHz regime.

### 3 Materials and Methods

This section gives an overview on the technical and methodical approaches used to produce the results of this thesis. In Section 3.1, the design process is outlined. The obtained designs were simulated as described in Section 3.2. The fabrication is briefly summarised in Section 3.3. The devices were fabricated by other members of the (extended) group. In Section 3.4, the working principle of the cryostat, as well as the measurement setup are presented. Lastly, the fitting procedure for the measurement results is described in Section 3.5.

#### 3.1 Design

The designs for both fabrication and simulation were drawn using the python module `gdsipy` [30] and the editor KLayout [31]. Each design consists of two parts: Resonator array and waveguide environment. Thus, the code to draw LC resonators and the two investigated waveguide geometries had to be developed. The approach taken and the obtained results are described in this section. All code is available on GitHub [32].

##### 3.1.1 Resonator

The resonator is designed to follow the lumped element approximation with capacitor plates for coupling and a meandering inductor to ground. Its shape is inspired by the design of Kim et al. [11]. A function to draw the resonator was written in python. It takes the length of the inductor  $l$ , its width  $w$  and interspacing  $s$ , as well as the width  $A$  and thickness  $t$  of the capacitor as input (see Fig. 3.1). The number of turns for the inductor and the height of the capacitor  $B$  are calculated as a function of these input parameters. The chosen parameter values are listed in Table 1. The values are picked such that the arrays produce a response between 4 and 8 GHz, which is the bandwidth of our measurement setup.

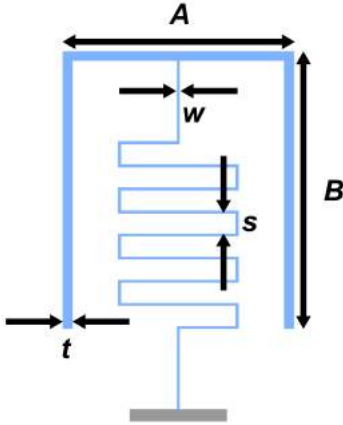


**Table 1: Dimensions for one Resonator.**  $A, t, l, w, s$  are chosen manually as input parameters for the resonator drawing function.

A	B	t	l	w	s
50 $\mu\text{m}$	60 $\mu\text{m}$	2 $\mu\text{m}$	279 $\mu\text{m}$	0.5 $\mu\text{m}$	4.5 $\mu\text{m}$

**Fig. 3.1: gds Drawing of one Resonator.** Values of the indicated parameters are listed in Table 1. The variable  $l$  is not indicated since it stands for the inductor length.

To draw the resonator array, the required number of resonator copies were aligned with the desired spacing in between them (see Fig. 3.2). The spacing between the resonators controls the capacitive coupling between them: The smaller the inter-resonator spacing, the higher the coupling capacitance. In arranging the arrays, one has two spacing parameters: The intra-cell spacing  $t_i$  and the inter-cell spacing  $t_x$ . The three different coupling configuration are thus given by choosing  $t_i, t_x$  accordingly:

- $\hookrightarrow t_i > t_x$  for trivial. Specifically,  $(t_i, t_x) = (24, 12) \mu\text{m}$  for measured and simulated arrays of this thesis.
- $\hookrightarrow t_i = t_x$  for normal. For the investigated arrays, the inter-resonator spacing was chosen as  $t_i = t_x = 18 \mu\text{m}$ , with 18  $\mu\text{m}$  being the mean of 12 and 24  $\mu\text{m}$ .
- $\hookrightarrow t_i < t_x$  for topological. The same values as for the trivial configuration were chosen for implementation of this configuration, but swapped:  $(t_i, t_x) = (12, 24) \mu\text{m}$ .

Those specific inter-resonator spacings apply for all resonator arrays of Sections 4.2 and 5.2, excluding Section 5.2.6.

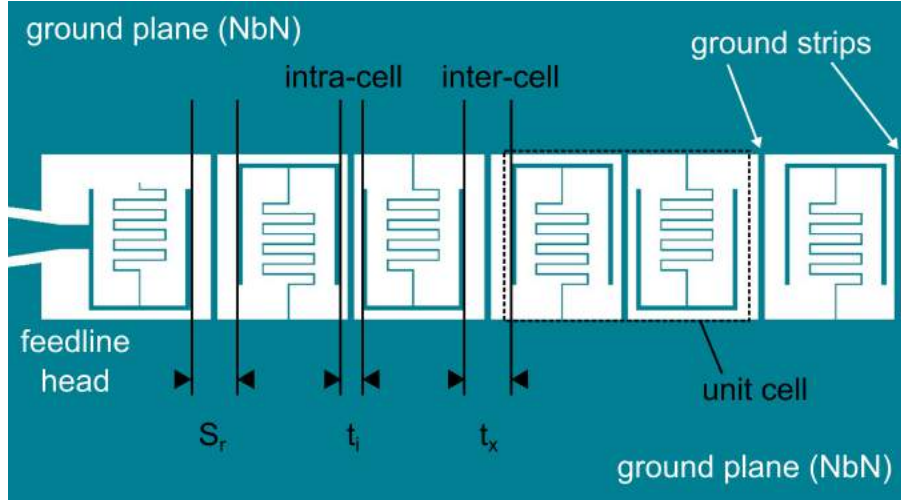


**Fig. 3.2: .gds Drawing of Trivial Resonator Array End.** The resonator array is enclosed by two ground planes, which are connected by ground strips. The spacing to the feedline  $S_r$  is chosen here to be equal to the inter-cell spacing  $t_x$ . The intra-cell spacing  $t_i$  is smaller for trivial configuration than  $t_x$ , giving a higher intra-cell coupling capacitance  $C_i$ , compared to the inter-cell coupling capacitance  $C_x$ . The array is capacitively coupled to a feedline on both ends.

### 3.1.2 Waveguide for Transmission Measurements

For transmission measurements, each end of the resonator array has to be coupled to a feedline. Here, the coupling was of capacitive nature. Two different feedline “head” geometries were implemented: A “T”-shaped feedline and a “ghost” feedline. The “T”-shaped feedline (see Fig. 3.3, blue inset) provided strong capacitive coupling. On the other hand, the “ghost” feedline (see Fig. 3.3, green inset) terminates in a structure resembling a resonator. The inductor however is not connected to ground, so that it does not resonate in the measurement range. Since it resembles a resonator unit from the array - but is not one - we call it ghost. Its purpose is to keep the resonance frequency of the edge resonator equal to the others. Apart from the head region, the microwave feedline is implemented as a coplanar waveguide in the middle and a bonding pad at the edges. The dimensions of the middle section were chosen to match an impedance of  $50\ \Omega$ , taking the high kinetic inductance of our superconducting film into account.

As indicated in Fig. 3.2, the ground planes on the two sides of the waveguide were connected to each other via the ground strips in between resonators. They reduced potential differences between the ground regions, as well as the intra- and inter-cell couplings  $C_i, C_x$ .

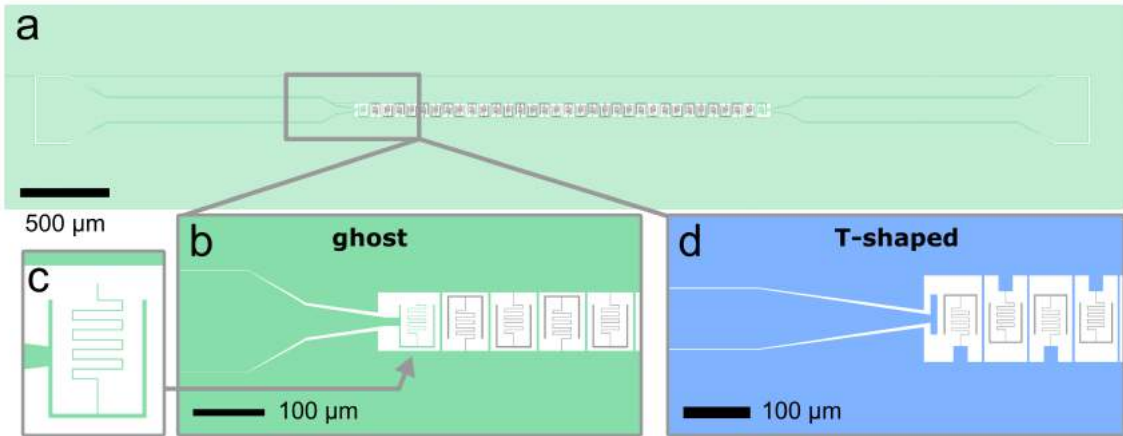


**Fig. 3.3: .gds Drawing of Transmission Waveguide.** a) Overview of whole device. The resonator array is shaded in grey. b) Enlarged view of implemented ghost feedline, c) Head region of ghost feedline, the resonator-like structure is not connected to ground. d) Enlarged view of implemented T-shaped feedline.

On a  $4 \times 7\ \text{mm}^2$  chip, three devices were placed. They all had the same number of resonators, arranged in trivial, topological and normal configuration respectively (see Fig. C.8 in appendix C.3 for the .gds of the etch mask). Devices hosting 16, 24, 32 or 64 resonators were fabricated. The “T”-shaped feedline was only implemented for a 16 resonator array, all other chips had feedlines with the “ghost head”.

### 3.1.3 Waveguide for Hanged Resonators

The waveguide for hanged resonators consists of a  $50\ \Omega$  coplanar waveguide along which hanged resonators are placed in some windows opened in the ground plane. The windows are equally spaced along the feedline. The dimensions of these windows depends on the resonator dimensions to be placed inside, as well as its spacing to the feedline. The width of one window was chosen to be twice the resonator width to reduce capacitive coupling of the resonator to the environment. The waveguide structure is shown in Fig. 3.4, without resonators. The chosen dimensions are listed in Table 2. For the waveguide, the dimension are chosen to match an impedance of  $50\ \Omega$ , taking the high kinetic inductance of our superconducting film into account.

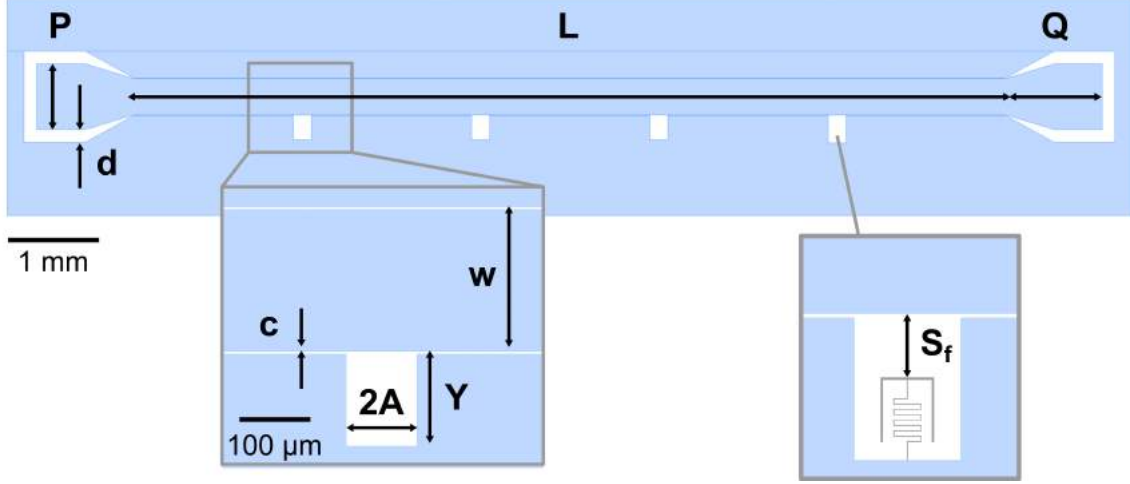


**Fig. 3.4: gds Drawing of Hanged Waveguide.** Values of the indicated parameters are listed in Table 2. Right inset: The spacing between resonator and feedline is denoted with  $S_f$ .

**Table 2: Dimensions of Waveguide for Hanged Resonator Measurements.**  $L, P, Q, d, c, w$  are chosen manually.  $A$  is the width of the hanged resonator,  $h$  is its entire height. The horizontal dimension of the wells  $Y$  is determined by the height of the hanged resonator, its spacing to the feedline  $S_f$  and the gap  $c$  of the waveguide.

$L$	$P$	$Q$	$d$	$c$	$w$	$A$	$Y$
476 mm	360 $\mu\text{m}$	530 $\mu\text{m}$	70 $\mu\text{m}$	4 $\mu\text{m}$	200 $\mu\text{m}$	50 $\mu\text{m}$	$S_f + 1.2h - c$

This hanged geometry allows simultaneous measurement of several resonators, provided they have distinguishable resonance frequencies. In our case, the resonance frequency was controlled by varying the inductor length. In this manner, four resonators were placed along the waveguide. They were designed to be apart in resonance frequency by at least 500 MHz. On one chip of  $4 \times 7\ \text{mm}^2$  dimension, three waveguides with each four resonators were placed. In each waveguide, all four resonators had the same distance  $S_f$  to the feedline. For the three waveguides,  $S_f$  was chosen to be 6, 18 or 60  $\mu\text{m}$  respectively.

While placing the resonator near the waveguide provides higher capacitive coupling, which is a good basis to check whether a response can be observed in measurement, it impedes extraction of the quality factors. The recorded spectrum will show a broad dip, due to high coupling to the feedline. To achieve accurate fitting, it is favourable to place the resonator at a sufficiently large distance to the waveguide, which will provide a coupling factor comparable to the internal quality factor (see Section 2.1).

We fabricated and measured three devices with different resonator-feedline distances  $S_f = 6, 18$  and  $60\ \mu\text{m}$ . Hence, the three distances were chosen to obtain the following information all in one cool down:

1. Whether all four resonators are visible in the spectrum ( $S_f = 6\ \mu\text{m}$ )
2. A transmission spectrum data set suited for fitting ( $S_f = 18\ \mu\text{m}$ ), and to surely be in the under-coupled regime ( $Q_c \gg Q_i$ ),  $S_f = 60\ \mu\text{m}$ .

## 3.2 Simulation

Before fabricating the devices, they were simulated to define a proper choice of parameters. To get a preliminary understanding about the frequency response of the system, we implemented simulations with Microwave Office [33]. Microwave Office allows for fast and real-time updated circuit response analysis. However, Microwave

Office only accepts a lumped-element circuit model of a resonator array as input. To implement an electromagnetic finite element simulation of our arrays, we made use of the software Sonnet [34]. Sonnet relies on solving Maxwell's Equations for the given (planar) geometry, by subdividing the metal surface and first calculating the voltage in each of those subsections separately and afterwards applying and adjusting currents to fulfil the boundary conditions across all subsections. A typical workflow in Sonnet results in a file such as in Fig. 3.5 and includes the following steps:

1. **Import a .gds file of the design to be simulated.** The .gds file should have the polygons at the places where the circuit has metal. Different materials should be separated into different layers. In our case, we only have one metal layer (NbN). Around the imported structure, a box is defined. Everything that touches this box is shorted to ground. As mentioned above, Sonnet subdivides the metal surface into smaller subsections or cells. The cell size was chosen to be  $0.5 \times 0.5 \mu\text{m}^2$ , according to the smallest dimension in the system, the inductor width  $w$ .
2. **Define the substrate and top material** (see Fig. 3.5, side view): For the substrate, we chose silicon and for the top material vacuum (air). The parameters are listed in Table 3.
3. **Specify the metal(s) layers.** Here, we used a planar metal in general mode, with kinetic inductance square  $L_s = 160 \text{ pH} / \square$  for simulations in Section 4 and  $112 \text{ pH} / \square$  in Section 5.2.3.
4. **Place the microwave ports.** All simulations required two ports to simulate the  $S_{21}$  response. We used box ports terminated in  $50 \Omega$ , placed on the edge of input and output feedline (see Fig. 3.5, top view).
5. **Configure the sweep.** The simulations were run in Adaptive Sweep (ABS) mode, with the option "Enhanced resonance detection" ticked. This option is recommended for extremely sharp resonances, characteristic for superconductor applications such as here. The ABS method calculates the full electromagnetic response at several discrete frequencies and then synthesises the whole spectrum from the acquired data [35]. Optionally, the current distribution of the circuit can also be calculated.



**Fig. 3.5: Example of Sonnet Simulation File.** For simulations, only the resonator array with two short section of feedline on each side was considered. Port 1 and Port 2 are schematically shown as boxes and terminated in  $50 \Omega$ . The structure is embedded in a grounding box (grey solid border).

**Table 3: Parameters of Substrate and Top Material** The symbols denote the relative permittivity  $\epsilon_{\text{rel}}$ , dielectric loss tangential  $\tan \delta$  and conductivity  $\sigma$ . All other parameters in the software had default values.

material	thickness	$\epsilon_{\text{rel}}$	$\tan \delta$	$\sigma$
silicon	$500 \mu\text{m}$	11.9	$10^{-7}$	$4.4 \cdot 10^{-4} \text{ S/m}$
air	$1 \text{ mm}$	1.0	0.0	0.0

### 3.3 Fabrication

All fabrication described here was carried out by other members of the (extended) group.

A schematic overview of the fabrication process is shown in Fig. 3.6. The numbering in the following description correspond to the steps defined in Fig. 3.6. The starting substrates are high-resistivity silicon wafers. These silicon wafers were first cleaned (1). Second, the wafers were spin-coated with AZ ECI 3007 photoresist (2). Markers for the electron beam lithography (EBL) were pre-defined using photo lithography (3) and subsequent development of the resist (4). For the markers, Ti/Pt was deposited using electron beam evaporation (5). The titanium acts as a adhesion layer for the platinum on the silicon substrate. Lift-off was done in NMP at  $70^\circ\text{C}$  for  $> 8 \text{ h}$  (6). Afterwards, a photoresist was spin-coated onto the wafer. The photoresist protects the wafer as it was diced into smaller chips (7), each containing several sample cells. The photoresist was stripped. Onto

those diced chips, a NbN film of thickness  $10 < t < 25$  nm was sputtered, giving a sheet inductance around  $80 < L_{\square} < 105$  pH/ $\square$  (8). For array fabrication, the chips were spin-coated with CSAR resist (9). Using the markers, the mask of the device layout was written on the chips with EBL (10). After development, all areas where the NbN needs to be etched were exposed (11). Next, the chips were dry-etched using reactive ion etching with  $\text{CF}_4/\text{Ar}$  (12). The resist was stripped by placing the chips in NMP at  $70^\circ\text{C}$  over 5 days (13). The chips were once more spin-coated with a photoresist and diced into the  $4 \times 7$  mm<sup>2</sup> sample chips. After dicing, the photoresist was stripped again.

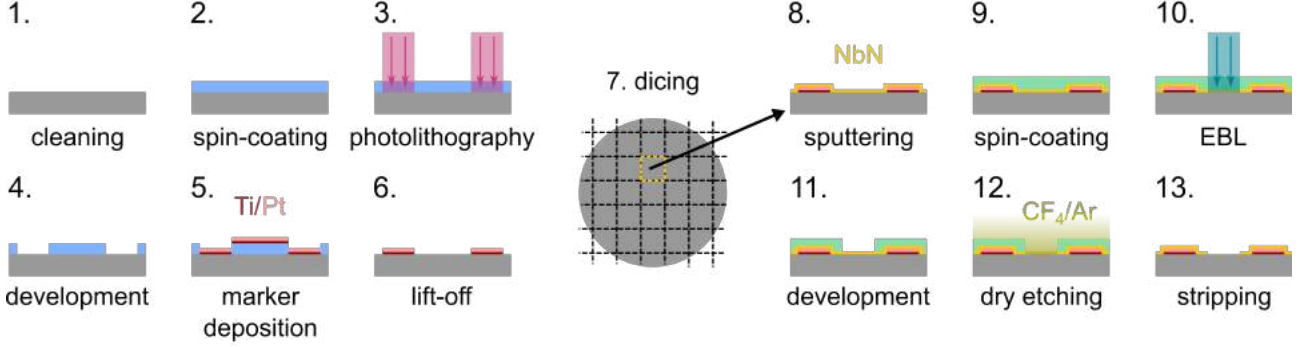


**Fig. 3.6: Schematic of Fabrication Process.** The coupled resonator arrays were fabricated from thin-film NbN on high-resistivity silicon substrate. 1) The silicon wafers were cleaned. 2) The wafer was spin-coated with photoresist. 3) The mask for markers was written with photolithography. 4) The photoresist was developed. Exposed areas are removed during the process. 5) Ti/Pt markers were deposited using electron beam evaporation. 6) The mask and metal residues were removed in a lift-off step in hot NMP. 7) The wafer was diced into smaller chips. 8) Thin-film NbN (23 nm) was sputtered onto the chips. 9) The chips were spin-coated with resist for electron beam lithography (EBL). 10) The etch mask to define the device structures was written with EBL. 11) Exposed areas of the EBL resist were removed during development. 12) The chips were dry-etched by  $\text{CF}_4/\text{Ar}$  ion plasma. 13) Resist residues were stripped from the chips by placing them in hot NMP over 5 days.

For measurement, a sample chip was glued onto a PCB with PMMA resist. The devices were connected to the PCB via wire-bonding (Fig. 3.7a). Several wires connecting the ground of the devices with the PCB improved grounding of the chip. Additionally, bridge bonds connecting the different ground areas on the sample chip were placed to prevent an imbalance in potential between the areas (Fig. 3.7b).

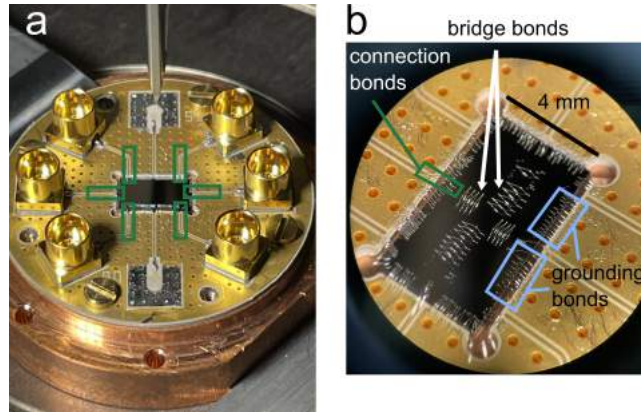


**Fig. 3.7: Bonding of the Devices.** To measure the devices in the cryostat, they were glued onto a PCB and connected via wire-bonding. The device has dimensions of  $4 \times 7$  mm<sup>2</sup>. a) PCB with chip (dark rectangle in center). The wires connecting the bonding pads of the devices with the SMP cable sockets of the PCB are framed in green. b) Zoom-in on bonded chip. One connection bond to the PCB sockets is framed in green. Bonds on the edge of the device to PCB ground (blue) improve grounding of the chip. Bridge bonds (white arrows) between on-chip ground areas reduce potential differences.

### 3.4 Cryogenic System

The devices were measured at temperatures  $< 20$  mK in a BlueFors BF-LD dilution refrigerator. An image is included in Fig. 3.8. After closing the cryostat by mounting all shields, it first needs to be pre-cooled from room temperature to  $T < 4.2$  K. A pulse tube compressor undertakes this task. The actual cooling process to reach lower than 20 mK can be initiated at temperatures  $T < 4.2$  K, the temperature of liquid helium. The cooling cycle relies on particular properties of  $\text{He}^3/\text{He}^4$  mixtures at low temperatures. A  $\text{He}^3/\text{He}^4$  mixture with



a sufficiently high concentration of  $\text{He}^3$  will separate in two phases at temperatures below 0.8 K (see Fig. 3.8b). These two phases are a  $\text{He}^3$ -rich phase (called concentrated phase) and a  $\text{He}^3$ -poor phase (called dilute phase). For  $T \rightarrow 0$  K, there is exclusively  $\text{He}^3$  in the concentrated phase. The dilute phase reaches a  $\text{He}^3$  concentration of 6.4%. In the dilute phase, the  $\text{He}^3$  have higher enthalpy than in the concentrated phase. Forcing  $\text{He}^3$  atoms from the concentrated to the dilute phase thus requires energy. This is used to induced cooling. Before initiating the cooling cycle, a condensing step of the  $\text{He}^3/\text{He}^4$  into the system is required. The helium mixture pressure is increased to about 2 bar with a compressor. The mixture is then pre-cooled by heat-exchangers on the condensing line and by its passage through the main flow impedance in the top part of the still. The condensed mixture fills up the mixing chamber, the heat exchangers and the still (see Fig. 3.8d). Subsequent pumping of the still leads to evaporative cooling, dropping still temperature below 0.8 K. As explained above, the mixture thus separates into two phases. The heavier dilute phase gathers at the bottom of the mixing chamber. After some time, the lighter concentrated phase and the heavier dilute phase settle above each other. This is the starting point for the actual cooling cycle.

The cooling cycle is depicted in Fig. 3.8d. When the still is pumped, mostly  $\text{He}^3$  will be removed, since its vapor pressure is considerably higher. The removed  $\text{He}^3$  is re-introduced via the condensing line into the mixing chamber. There, it is forced from the concentrated to the dilute phase, inducing cooling.  $\text{He}^3$  in the dilute phase is then driven from the mixing chamber to the still due to osmotic pressure (concentration gradient). The cooling power can be increased by heating the still. Heating leads to an increased still vapour pressure and thus a higher flowing rate of  $\text{He}^3$ , meaning more  $\text{He}^3$  crosses the phase boundary [36].

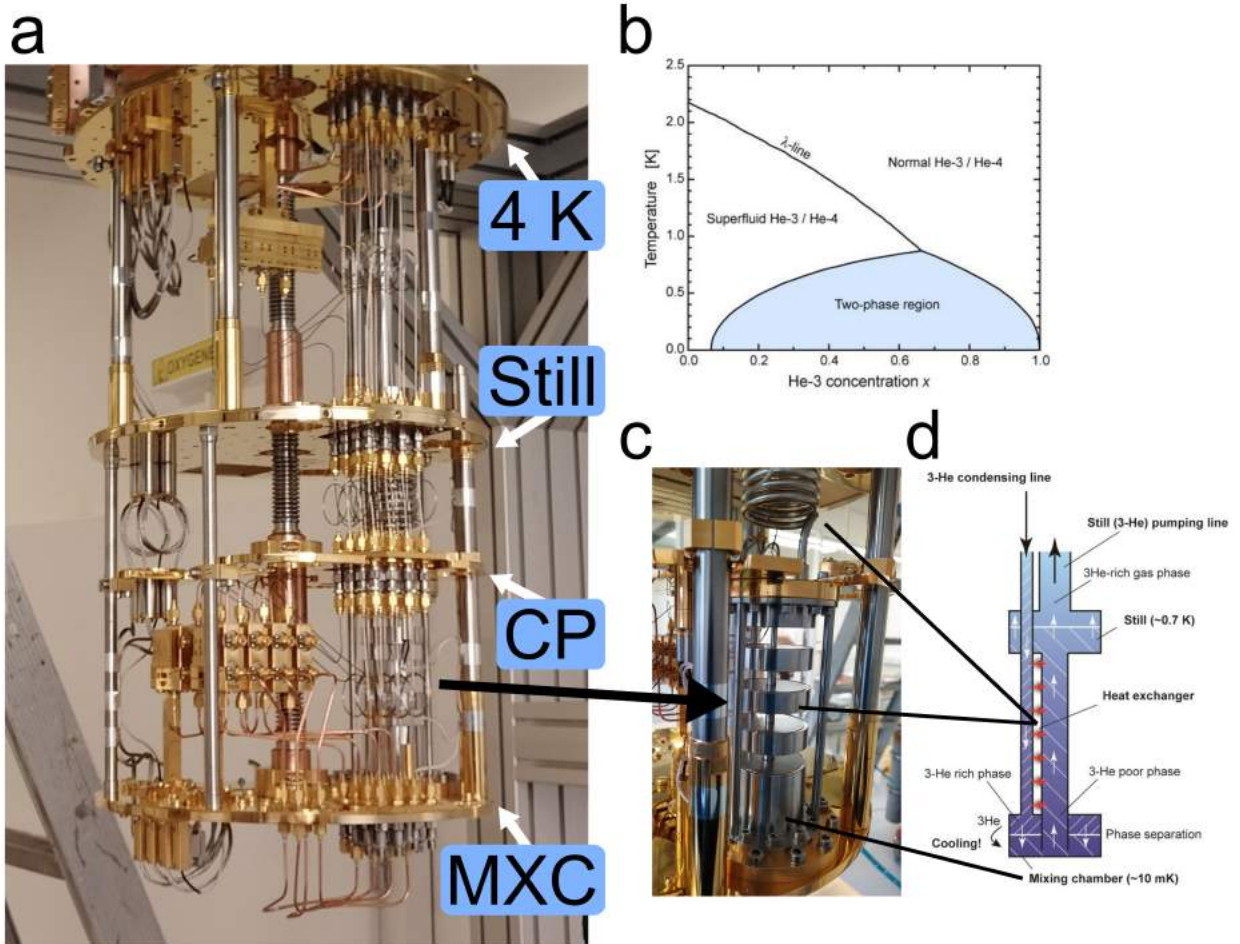


**Fig. 3.8: Dilution Cryostat.** a) Image of open cryostat. The different plates are labelled: quasi-4K plate (4K), still, cold plate (CP) and mixing chamber plate (MXC), on which the mixing chamber is situated (shown in c). Above the quasi-4K is the 50 K stage (not visible in picture). b) Phase diagram of  $\text{He}^3/\text{He}^4$ . Depending on temperature and  $\text{He}^3$  concentration fraction, the mixture is either in normal state, a superfluid or separated into two phases. d) Schematic of cooling cycle. Figure b and d taken from [36].

### 3.4.1 Measurement Setup

For measurement, a Rohde & Schwarz ZNB20 Vector Network Analyzer (VNA) with four ports was used. All four ports were connected to input and output lines as shown in Fig. 3.9a. This, and circulators, allowed subsequent measurement of all scattering parameters  $S_{11}, S_{12}, S_{21}, S_{22}$  in one measurement run. The VNA was

remotely controlled by a Jupyter notebook python script. The input lines were attenuated by 20 dB in the fridge. A chain of 3 insulators and an amplifier was placed on the output lines. DC blocks on all lines got rid of DC offsets in the signal. Since we usually placed three devices on each sample chip, microwave switches have been included into the setup at the mixing chamber plate. To each switch, 6 lines could be connected (see Fig. 3.9f,g). With the measurement setup shown here, 6 devices could thus be fully characterised in one cool down. The sample chips on the PCB were mounted on a coldfinger thermally anchored at the mixing chamber plate (see Fig. 3.9c). The coldfinger is magnetically shielded (see Fig. 3.9c) to block off vortex penetration into the superconducting thin film sample.

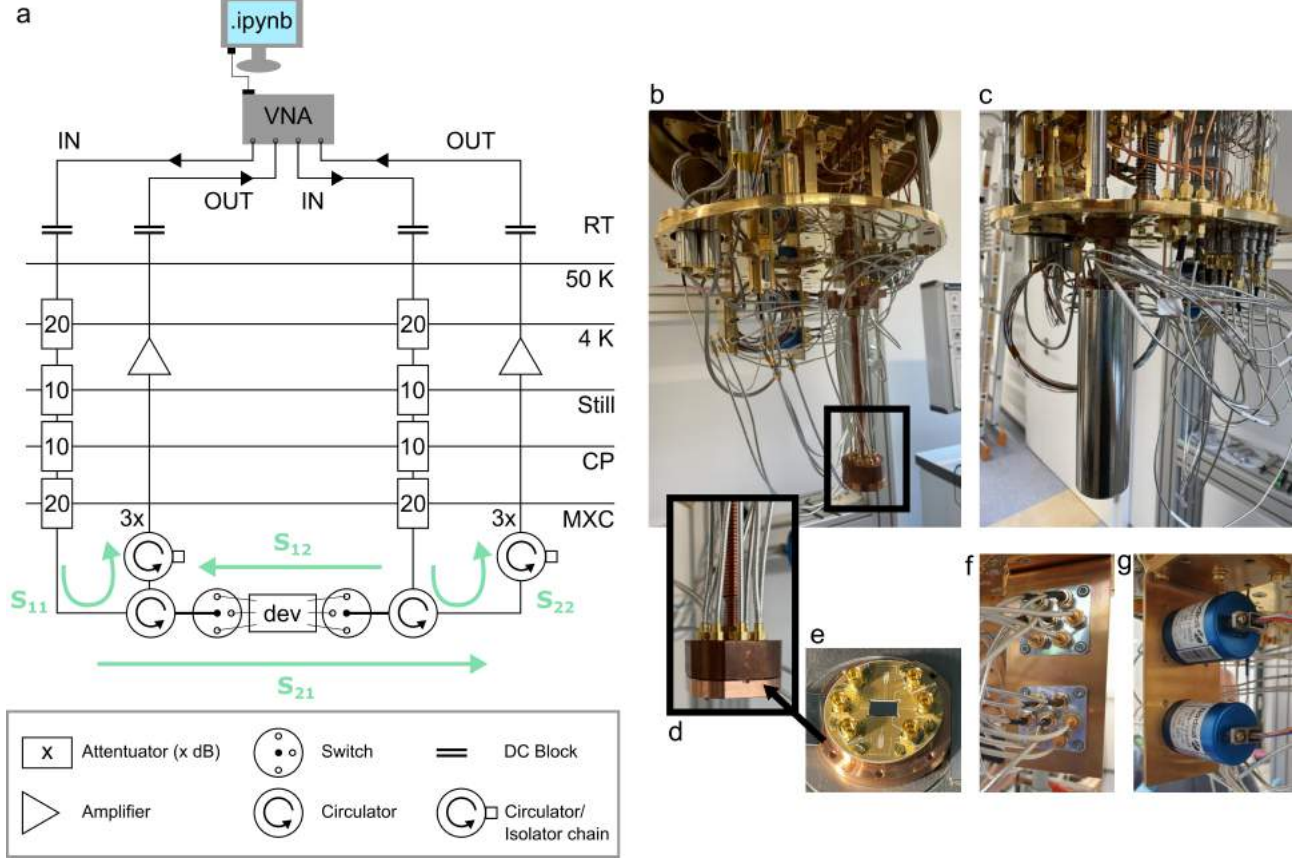


**Fig. 3.9: Measurement Setup.** The devices were mounted on a coldfinger thermally anchored at the mixing chamber plate and measured with a VNA. a) Schematic of cryogenic setup. All four ports of the VNA were connected, enabling subsequent measurement of all scattering parameters of the array ( $S_{11}$ ,  $S_{12}$ ,  $S_{21}$ ,  $S_{22}$ ). Data was recorded by controlling the VNA via computer with a Python script. Microwave switches allowed measuring several devices in one cooldown and same in- and output lines. The symbols are labelled in the legend at the bottom. The device (dev) is shown as a rectangle. On the left, the different stages are named: Room temperature (RT), 50 K stage, 4 K stage, still, cold plate (CP) and mixing chamber plate (MXC). b) Image of mixing chamber plate. On the coldfinger, the chip was mounted (framed in black). c) Image of coldfinger enclosed in its shield. d) Zoom-in on the coldfinger tip. The PCB with the chip (e) is mounted from below. f + g) Front and back of switches.

## 3.5 Fitting

### 3.5.1 Hanged Resonators

The  $S_{21}$  transmission is collected as a function of probe frequency  $f$ . To fit the hanged resonators, the python class `resonator_tools.circuit.notch_port` by Sebastian Probst [37] was applied. It includes a fitting routine with background correction for resonators in notch configuration. First, the baseline of the transmission amplitude spectrum is fitted using the function `fit_baseline_amp()`. This fit is then removed from the data and simultaneously, the data is normalised. Using the `autofit` routine, the normalised data is fitted. The python module takes the function

$$S_{21}^{\text{notch}}(f) = ae^{i\alpha}e^{-2\pi if\tau} \left( 1 - \frac{Q_L}{1 + 2iQ_L(f/f_r - 1)} e^{i\phi} \right) \quad (3.1)$$

with prefactors  $a$ ,  $\alpha$  and electrical delay  $\tau$  describing the environment of the sample, such as the wiring outside and inside the fridge, through which the signal travels. The sample-specific parameters are the resonance



frequency  $f_r$ , the loaded quality factor  $Q_L$ , the absolute value of the coupling quality factor  $|Q_c|$  and a phase  $\phi$  quantifying the impedance mismatch [38]. The fitting procedure first follows the technique described in [39] and finalises the fitting by utilising the `scipy.optimize` least square fitting toolbox.

The fitting routine provides the diameter-corrected internal quality factor  $Q_{i, \text{dia\_corr}}$ , the absolute value of the coupling factor  $|Q_c|$  and the loaded quality factor  $Q_L$  with their respective errors. For enhanced accuracy, the internal quality factor is extracted with the diameter correction method, instead of the conventionally employed  $\varphi$  rotation method. The conventional method overestimates the value of  $Q_i$  for asymmetric line shapes [40].

### 3.5.2 Arrays

For the resonator arrays, each peak of the  $S_{21}$  magnitude was fitted with the Lorentzian

$$|S_{21}(f)| = \frac{S_{\max}}{\sqrt{1 + 4 \left( \frac{f - f_0}{\kappa} \right)^2}} \quad (3.2)$$

with the central frequency  $f_0$  and a full width at half maximum (FWHM)  $\kappa$ . The loaded quality factor is then estimated as  $Q = f_0/\kappa$  [41].

The fitting code iterates over all peaks. First, it searches for the transmission amplitude maximum in the data, then proceeds to fit the curve in a window around it. Afterwards, the fit parameters are used to draw the fit over the whole measurement range. This fit is then subtracted from the measurement data. The code then finds the next maximum in the data and so on.

## 4 Modelling

As a guideline for fabrication and afterwards interpretation of results, the resonator arrays were modelled making use of Sonnet. In this section, we present the findings from Sonnet simulations and from theoretical models in Section 2.3. First, a resonator dimer is investigated in Section 4.1. The discussion is then extended to arrays in Section 4.2.

### 4.1 Dimer

We initially studied the coupling strength between two capacitively coupled resonators (a dimer, see Fig. 4.1a). From the  $S_{21}$  spectrum (see Fig. 4.1b), the two mode frequencies  $f_1, f_2$  were extracted as the two maxima and the coupling  $J = \frac{1}{2}(f_2 - f_1)$  was determined. This was done for different inter-dimer separations  $d$  and spacings to the feedline  $S_r$ , ranging from 4 to 86  $\mu\text{m}$  for  $d$  and 4 to 32  $\mu\text{m}$  for  $S_r$ . The result is plotted in Fig. 4.1. For an array in the trivial configuration ( $t_i = 12 \mu\text{m}$ ,  $t_x = 24 \mu\text{m}$ ), we thus expect alternating couplings of (157, 106) MHz, while they are swapped for the topological configuration. In the normal configuration, the average inter-resonator coupling is expected to be around 133 MHz.

From these simulations, we also take notice of a possible non-negligible second neighbour coupling in the arrays: Resonators separated by more than one resonator width ( $> 50 \mu\text{m}$ ) still exhibit coupling constants around 50 MHz (see Fig. 4.1).

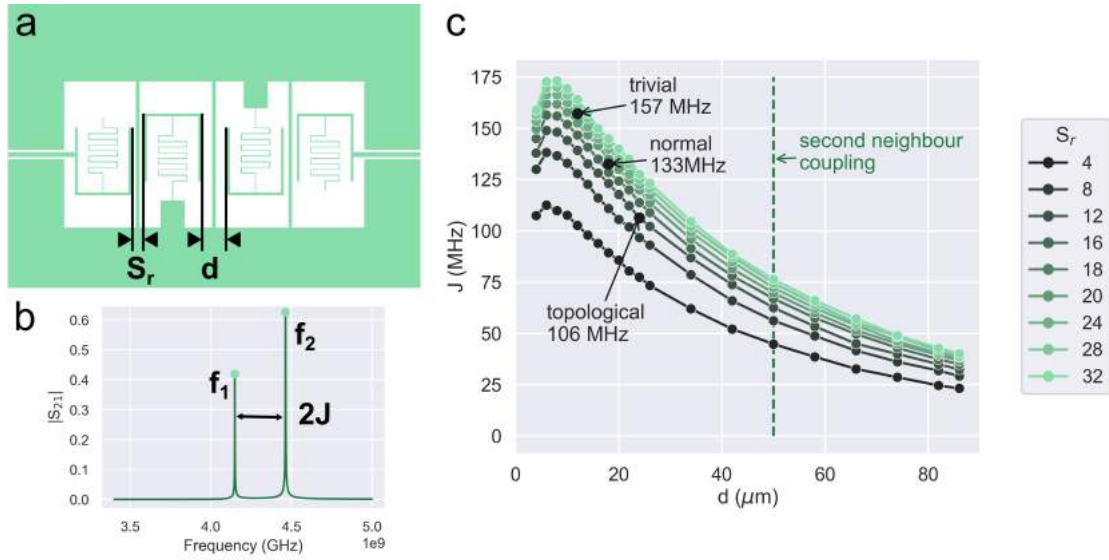


**Fig. 4.1: Simulation of Dimer.** a) Schematic of simulated Dimer. The two variables, distance  $d$  and separation to the feedline  $S_r$  are marked. b) Simulated  $S_{21}$  spectrum for  $d = 12 \mu\text{m}$ ,  $S_r = 24 \mu\text{m}$ . The frequency spacing  $|f_2 - f_1|$  is equal to  $2J$ . c) Coupling constant  $J$  as a function of dimer separation  $d$ . The values for ( $d = 12 \mu\text{m}$ ,  $S_r = 24 \mu\text{m}$ ), ( $d = 18 \mu\text{m}$ ,  $S_r = 18 \mu\text{m}$ ) and ( $d = 24 \mu\text{m}$ ,  $S_r = 12 \mu\text{m}$ ) are highlighted since those parameters were used in the trivial, normal and topological configuration of the simulated and measured resonator arrays.

### 4.2 Array

The resonator arrays are simulated using Sonnet, with a kinetic square inductance  $L_{\square} = 160 \text{ pH}/\square$ . Moreover, calculations from an ABCD circuit model and a tight-binding model provide a tool to study the influence of particular parameters of the system on the metamaterial transmission spectrum. In Section 4.2.1, we report the results of Sonnet simulations performed on arrays with a growing number of unit cells. The discussion is extended in the next subsection by observing the simulated current density distributions for the different modes of the array. In Section 4.2.3, the influence of second-neighbour coupling on both transmission spectrum and current distribution is studied. Lastly, the influence of the feedline coupling and deviations in resonance frequency on the transmission spectrum are investigated.

#### 4.2.1 $S_{21}$ Transmission Spectra

In a first step, the evolution of the  $S_{21}$  transmission spectrum with increasing unit cell number  $N$  is investigated. Transmission spectra for  $N=(2,4,8,16)$  unit cells simulated with Sonnet are plotted in Fig. 4.2. In all arrays, the same spacings were chosen for the three configurations, namely  $(d_i, d_x)=(18,18) \mu\text{m}$  for normal and  $(d_i, d_x)=(12,24) \mu\text{m}$  for trivial and swapped for topological, respectively.

Looking at all spectra, one can point out general features. An array of  $N$  unit cells shows  $2N$  peaks in transmission. Those transmission modes (peaks) are spaced more densely with increasing  $N$ . Focusing on the normal configuration (left column in Fig. 4.2), one can see that the passband span  $\approx 4J$  is roughly the same for all  $N$ . This is expected since in all arrays, the inter-resonator coupling  $J$  is the same. Hence, for instance, in an array with 16 resonators ( $N = 8$ ), the peaks are more densely spaced than in a octamer ( $N = 4$ ) for the same passband span. The same reasoning applies for the two other configurations (trivial, topological) as well. Moreover, in all spectra, the transmission amplitude is at a maximum inside the band and decreases towards the edges of the passband on both sides. The trend is more pronounced for higher  $N$ . An explanation for this passband shape is provided below in Section 4.2.2. Lastly, the transmission amplitude generally decreases for increasing  $N$  (compare y-axis labels in Fig. 4.2). The more sites an array has, the more opportunities present itself for a microwave photon travelling through to escape the array into the environment. Hence, higher losses and lower transmission amplitude are expected for longer arrays.

Now we focus on the trivial and topological configuration. As expected, a middle band gap opens in the array spectrum for the trivial and topological configuration. In the topological arrays, two peaks, the HEMs, reside in the center of the middle band gap. They are further studied in Sections 4.2.2 and 4.2.3. The frequency spacing of these HEMs corresponds to a certain degree of hybridisation between the edge modes. The presence of these modes in the center of the middle band gap is not a coincidence. Their relative position in the middle band gap can be tuned via the feedline coupling of the array edges (see Section 4.2.3). As expected, the splitting between the HEMs decreases for increasing  $N$ . The superposition between the photonic envelopes of the edge modes decreases with the array length. Additionally, their transmission amplitudes also decrease with increasing  $N$ . Since the overlap between the left and right edge mode is reduced with increasing  $N$ , the transmission goes down, reaching zero for zero overlap. As we see later, in this case, the edge modes are still accessible in reflection (see Section 5.2.5).

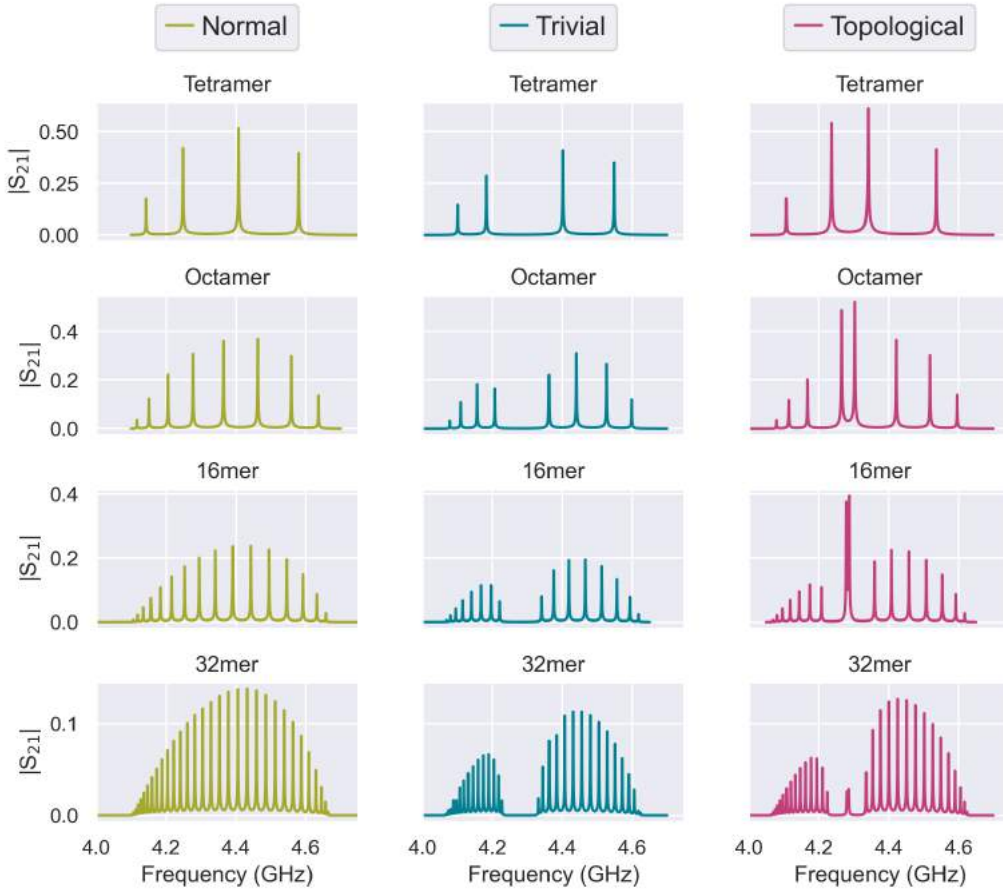


**Fig. 4.2:  $S_{21}$  Transmission Spectra of Arrays with Sonnet.** Simulated  $S_{21}$  transmission spectra for  $N = (2,4,8,16)$  unit cells. For all arrays, the same spacings were used: Normal  $(d_i, d_x) = (18, 18) \mu\text{m}$ , trivial  $(d_i, d_x) = (12, 24) \mu\text{m}$ , topological  $(d_i, d_x) = (24, 12) \mu\text{m}$ . The square inductance was  $L_{\square} = 160 \text{ pH}/\square$ .

#### 4.2.2 Current Distributions

Sonnet also provides the option to simulate the current density for the different array modes. It allows us to get an impression of the mode structure of the array. To couple the resonator array to a qubit, it is valuable

to know its mode structure. Depending on the specific mode profile, one can determine the best position for coupling qubits in order to maximise the interaction strength.

All following bar plots were extracted from Sonnet current density simulations of the specified resonator array. The simulation data was then exported for each site of the array, giving a table of current density values. These current density values were calculated for each (x,y)-coordinate of the array, with a mesh size of  $25\ \mu\text{m}$  in both directions. In the bar plot, the maximal current density for each site is then plotted.

Being aware of the expected mode structure of the resonator array helps in understanding the transmission and reflection spectra. For instance, it provides an explanation for the passband shapes observed in Fig. 4.2. In Fig. 4.3, the maximal on-site current density is plotted for an eight resonator array at each peak in the transmission spectrum (Fig. 4.2). It can be observed that the current density magnitude on the first and last side is maximal for modes  $n = 4, 5$  and decreases towards  $n = 1$  and  $n = 8$  respectively. This implies that the coupling of a mode to the feedline is maximal for  $n = 4, 5$ , but minimal for  $n = 1, 8$ . The transmission for modes with low coupling to the feedline is lowered, resulting in the given passband shape.

The same reasoning as above also applies to the other arrays. Their current density profiles can be found in appendix B for  $N = 2, 8$ .

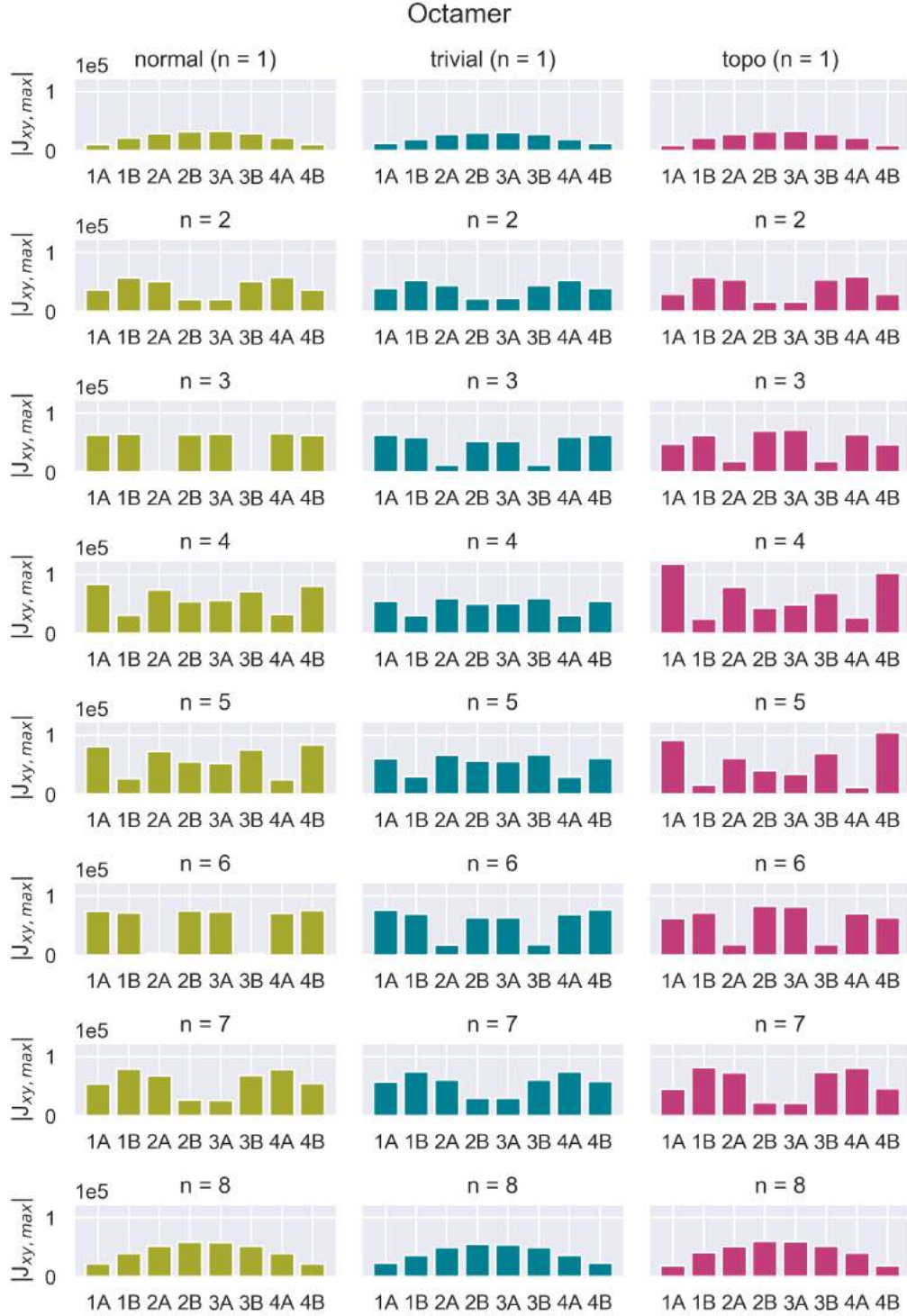


**Fig. 4.3: Simulated Maximal Current Density on Each Site in a Normal, Trivial and Topological Octamer.** Simulated current density maxima  $|J_{xy}|$  on each site for an octamer ( $N=4$ ). The plots are arranged according to mode number  $n$ .

#### 4.2.3 Second-Neighbour Coupling

Introducing second-neighbour coupling  $J_s$  into the system leads to an asymmetric band structure. Moreover, the edge states become less localised for increasing  $J_s$  [25]. To assert whether we have second neighbour coupling in our system, Sonnet current density simulations are compared to a tight-binding model. The tight-binding model Hamiltonian is constructed as in Eq. (2.70), with added second neighbour coupling entries  $J_s$ . The matrix

for the system thus reads

$$[\mathbf{H}] = \begin{pmatrix} \omega_r & J_i & J_s & 0 & 0 & 0 & \cdots & 0 & 0 & 0 & 0 \\ J_i & \omega_r & J_x & J_s & 0 & 0 & \cdots & 0 & 0 & 0 & 0 \\ J_s & J_x & \omega_r & J_i & J_s & 0 & \cdots & 0 & 0 & 0 & 0 \\ 0 & J_s & J_i & \omega_r & J_x & J_s & \cdots & 0 & 0 & 0 & 0 \\ \vdots & 0 & J_s & \ddots & \ddots & \ddots & \ddots & 0 & 0 & 0 & 0 \\ \vdots & \vdots & 0 & J_s & \ddots & \ddots & \ddots & \ddots & 0 & 0 & 0 \\ \vdots & \vdots & \vdots & 0 & \ddots & \ddots & \ddots & \ddots & \ddots & 0 & 0 \\ \vdots & \vdots & \vdots & \vdots & 0 & J_s & \ddots & \ddots & \ddots & J_s & 0 \\ \vdots & \vdots & \vdots & \vdots & \vdots & \vdots & \ddots & \ddots & \ddots & J_x & J_s \\ 0 & 0 & 0 & 0 & 0 & 0 & \cdots & J_s & J_x & \omega_r & J_i \\ 0 & 0 & 0 & 0 & 0 & 0 & \cdots & 0 & J_s & J_i & \omega_r \end{pmatrix} \quad (4.1)$$

In Fig. 4.4, the extracted on-site current density amplitudes from Sonnet simulations are plotted for a 16 resonator array. Additionally, the eigenmodes of the Hamiltonian in Eq. (4.1) were numerically calculated for  $J_s/2\pi = 0$  and 40 MHz. The other parameters were chosen as  $J_i/2\pi = 106$  MHz,  $J_x/2\pi = 157$  MHz,  $\omega_r/2\pi = 4.33$  GHz. These are estimated by comparing calculated eigenfrequency spectra for different parameters with the simulated transmission spectra, as well as the dimer simulations in Section 4.1. For no second-neighbour coupling, the occupation amplitude on every other site vanishes (see Fig. 4.4). However, that is not what we observe in the Sonnet current density simulation, implying we have second-neighbour coupling in our resonator arrays. The current density simulation resembles the eigenmode distribution for  $J_s/2\pi = 40$  MHz.

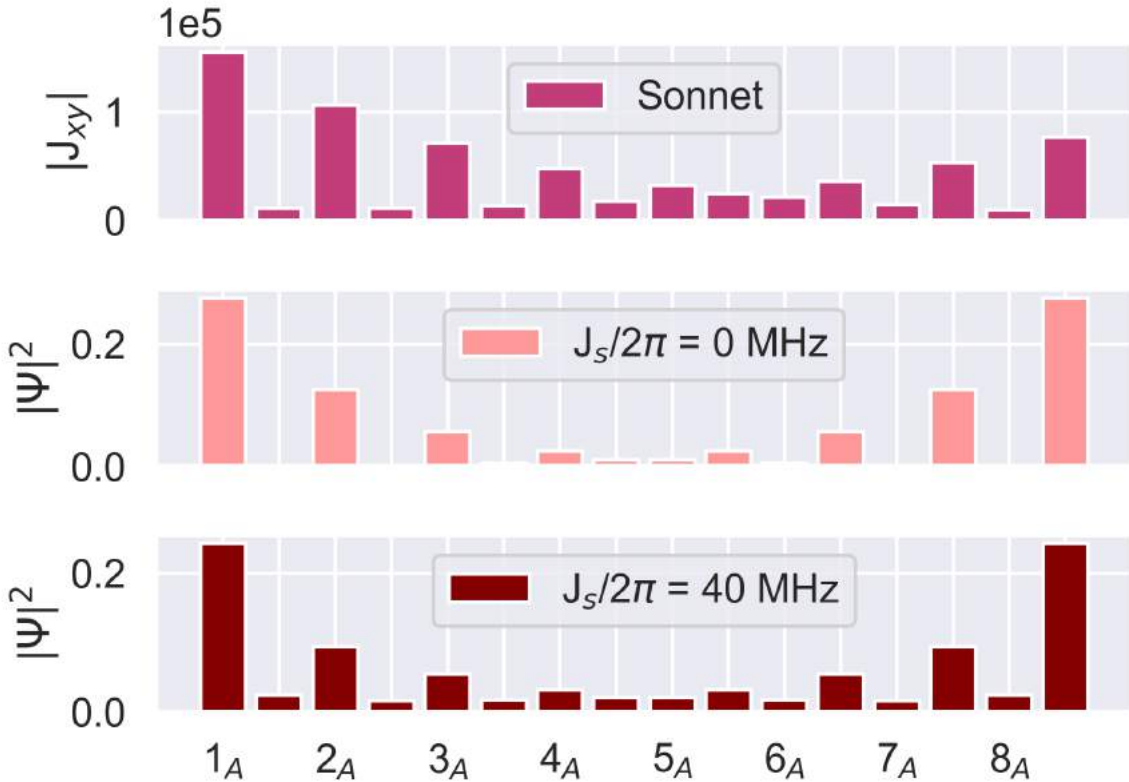


**Fig. 4.4: Second-Neighbour Coupling: HEM Occupation Distribution.** Top: Simulated current density amplitude maxima  $|J_{xy}|$  of mode  $n = 7$  on each site for  $N = 8$  unit cells. Middle: Calculated eigenmode occupation for mode  $n = 7$  with  $J_s/2\pi = 0$  MHz. Bottom: Calculated eigenmode occupation for mode  $n = 7$  with  $J_s/2\pi = 40$  MHz.

The second-neighbour coupling also influences the  $S_{21}$  transmission spectrum. This can be seen in Fig. 4.5. The plot shows a modelled  $S_{21}$  transmission spectrum from the tight-binding Hamiltonian. The spectrum is



obtained by drawing a Lorentzian shape (refer to Eq. (3.2)) centered at each eigenfrequency, with a linewidth of  $\kappa = 0.3$  MHz, and summing them up. While the lower passband is compressed, the upper passband expands relative to no second-neighbour coupling. This also results in a relative shift of the middle band gap compared to no second-neighbour coupling.

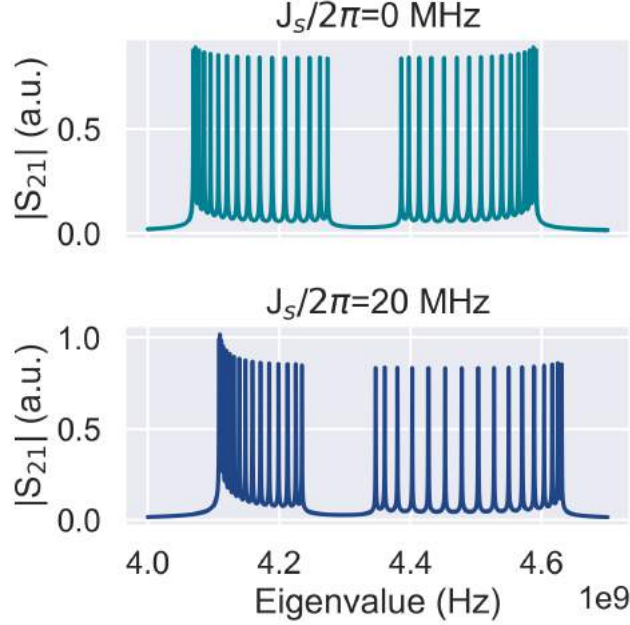


**Fig. 4.5: Second-Neighbour Coupling: Transmission Spectrum.** The eigenfrequencies of the tight-binding Hamiltonian in Eq. (4.1) with  $N = 16$ ,  $J_i/2\pi = 106$  MHz,  $J_x/2\pi = 157$  MHz and  $\omega_r/2\pi = 4.33$  GHz are plotted as a transmission spectrum. Top:  $S_{21}$  spectrum from eigenfrequencies of the tight-binding Hamiltonian, with  $J_s/2\pi = 0$  MHz. Bottom: For non-zero second-neighbour coupling, the eigenfrequencies in the upper (lower) passband are (less) more densely spaced than for  $J_s = 0$  MHz. This compression/ expansion of the pass band leads to a shifted middle band gap.

#### 4.2.4 Displacement of HEMs

The HEMs in topological configuration are expected to lie in the center of the middle band gap. However, they can be shifted due to the asymmetric coupling environment of first and last resonator. More precisely, if the first and last resonator have a different capacitive environment, their resonance frequency is shifted in comparison to the other resonators in the array. This breaks the required symmetry of the SSH model (see Section 2.3.2) and leads to an asymmetric spectrum. The HEMs no longer lie at the center of the middle band gap. This can be studied, for instance, by tuning the feedline coupling capacitance  $C_c$  and observing its effect on the transmission spectrum, as plotted in Fig. 4.6. The spectrum is most symmetric for  $C_c = C_x$ . This is reasonable, considering this provides first and last resonator of the array with the same capacitive environment as the other resonators. The transmission spectrum is calculated following the ABCD formalism in Section 2.3.1 and applying Eqs. (2.27) and (2.28). The circuit parameters were set as  $C_r = 13.3$  fF,  $L_r = 89.28$  nH,  $C_i = 0.61$  fF and  $C_x = 1.22$  fF. They were estimated from comparing a ABCD-derived spectrum with a Sonnet-simulated spectrum for unit cell number  $N = 4$ .

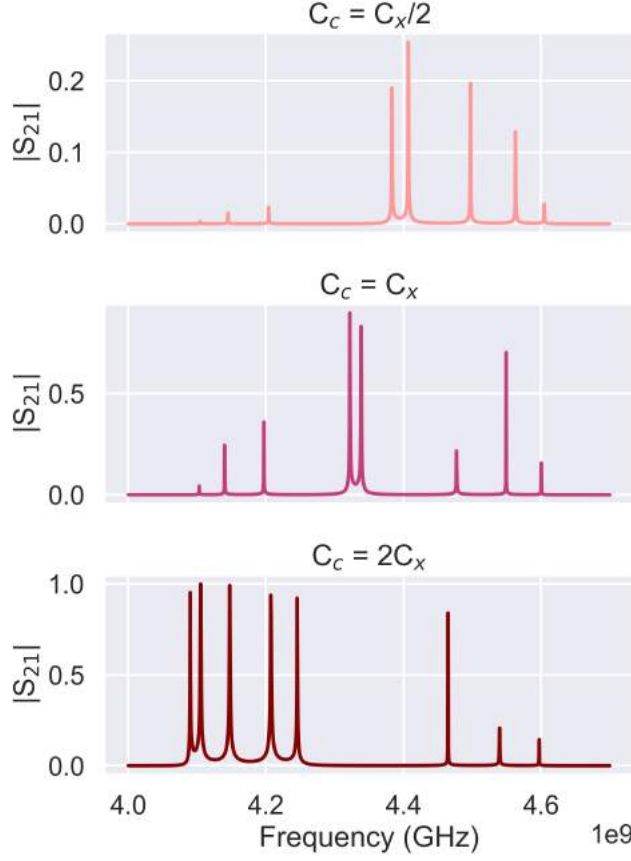


**Fig. 4.6: Influence of Feedline Coupling.**  $S_{21}$  Transmission spectra calculated from an ABCD Model with  $N = 4$ ,  $C_r = 13.3$  fF,  $L_r = 89.28$  nH,  $C_i = 0.61$  fF and  $C_x = 1.22$  fF. The three spectra show the influence of different feedline coupling capacitance  $C_c$  in terms of  $C_x$ . For mismatched  $C_c$  and  $C_x$ , the HEMs are displaced from the center of the middle band gap and the spectrum is asymmetric.

Analogously, a variation  $\delta$  can be introduced in resonance frequency  $\omega_r$  of the first and last resonator in the tight-binding Hamiltonian formalism:

$$[\mathbf{H}] = \begin{pmatrix} \omega_r + \delta & J_i & 0 & 0 & 0 & 0 & \cdots & 0 & 0 & 0 & 0 \\ J_i & \omega_r & J_x & 0 & 0 & 0 & \cdots & 0 & 0 & 0 & 0 \\ 0 & J_x & \omega_r & J_i & 0 & 0 & \cdots & 0 & 0 & 0 & 0 \\ 0 & 0 & J_i & \omega_r & J_x & 0 & \cdots & 0 & 0 & 0 & 0 \\ \vdots & \vdots & 0 & \ddots & \ddots & \ddots & \ddots & 0 & 0 & 0 & 0 \\ \vdots & \vdots & \vdots & 0 & \ddots & \ddots & \ddots & \ddots & 0 & 0 & 0 \\ \vdots & \vdots & \vdots & \vdots & 0 & \ddots & \ddots & \ddots & \ddots & 0 & 0 \\ \vdots & \vdots & \vdots & \vdots & \vdots & 0 & \ddots & \ddots & \ddots & 0 & 0 \\ \vdots & \vdots & \vdots & \vdots & \vdots & \vdots & \ddots & \ddots & \ddots & J_x & 0 \\ 0 & 0 & 0 & 0 & 0 & 0 & \cdots & 0 & J_x & \omega_r & J_i \\ 0 & 0 & 0 & 0 & 0 & 0 & \cdots & 0 & 0 & J_i & \omega_r + \delta \end{pmatrix}. \quad (4.2)$$

By plotting the eigenvalue spectra as a function of  $\delta$  (see Fig. 4.7), it is also evident that for a symmetric spectrum, the resonance frequency of the first and last resonator must be similar to all other resonators. For negative  $\delta$ , the HEMs are shifted towards the lower passband, while for positive  $\delta$ , they are shifted towards the upper passband. The passband eigenvalues start to also shift for  $|\delta| \gtrsim J_i, J_x$ .



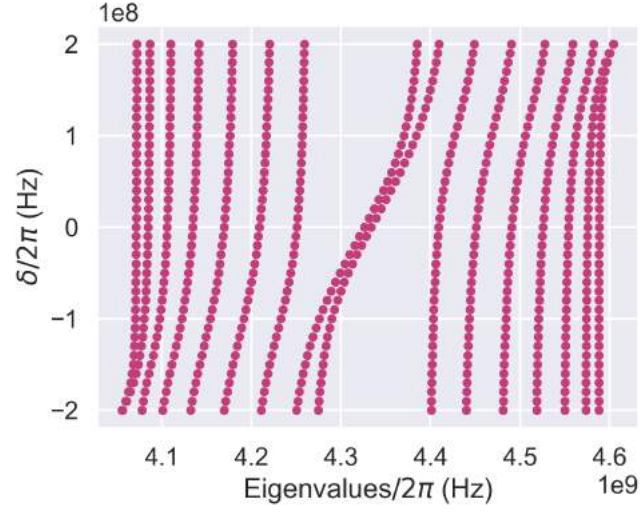


**Fig. 4.7: Influence of Feedline Coupling.** For each value  $\delta/2\pi$ , the eigenvalue spectra calculated from tight-binding Hamiltonian in Eq. (4.2) with  $N = 8$ ,  $f_r = 4.33$  GHz,  $J_i/2\pi = 106$  MHz and  $J_x/2\pi = 157$  MHz is plotted. This shows that a variation  $\delta$  in resonance frequency  $\omega_r$  of the first and last resonator leads to an asymmetric band spectrum with displaced HEMs.

## 5 Experimental Results

In this section, the main measurement results are presented. First, the measurements from hanged resonators are summarised in Section 5.1. They serve as a characterisation of the building block of the metamaterial, the superconducting lumped-element resonators. Second, the principal findings of resonator arrays measurements are presented in Section 5.2.

### 5.1 Characterisation of Resonators

As explained above (Section 2.1.1), the resonators were measured in hanged configuration to extract all quality factors in one measurement. Two devices with different feedline coupling configuration were measured (see schematics on left in Fig. 5.1)). For both devices, all four resonance frequencies of the four resonators were visible (see Fig. 5.1). To determine the quality factors for the resonators at low photon number, a power sweep on each resonance was performed. These sweeps were then fitted with Eq. (3.1).

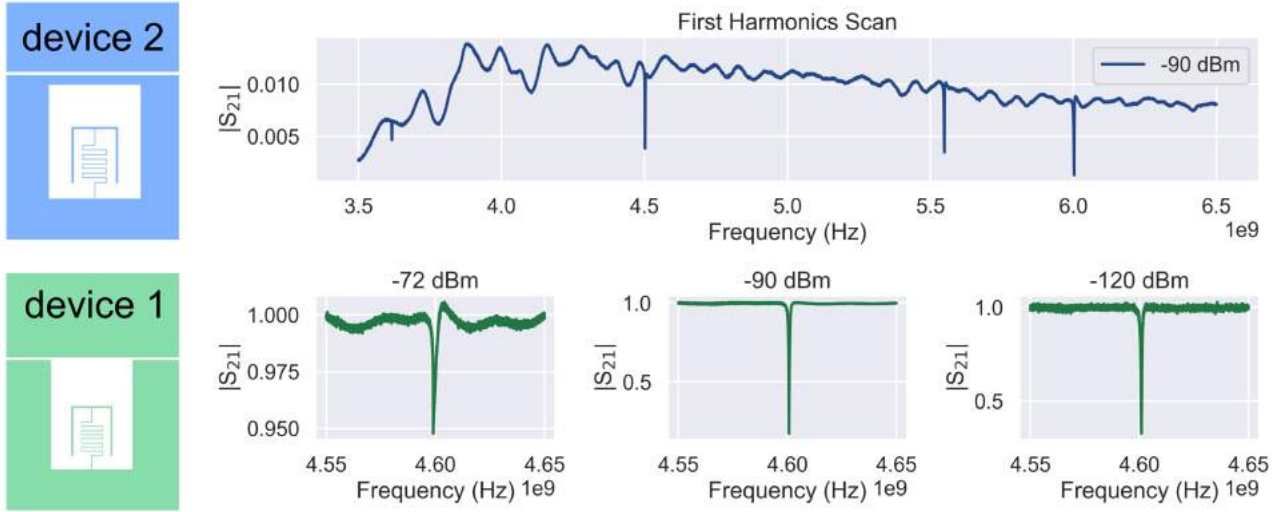


**Fig. 5.1: Overview on Transmission Measurements.** Top: First harmonics scan for device 2 at -90 dBm drive power. All four resonances are visible, as well as standing waves in the background. Bottom: Zoom-in on the resonance dip for a resonator (on device 1) with inductor length  $l = 279 \mu\text{m}$  for three different drive powers (-72, -90, -120) dBm. The data is baseline-corrected and normalised. Data for drive powers between -90 and -120 dBm was fitted to extract the quality factors. Above -90 dBm, the fit failed (see -72 dBm), due to the non-linearity of the system.

In Fig. 5.2, the extracted quality factors are plotted as a function of drive power. The internal quality factor assumes values between 20'000 and 50'000. It converges for low power to the single photon limit. The saturation at high power could not be observed, since the non-linearity of the system hampers fitting at drive powers above -90 dBm.

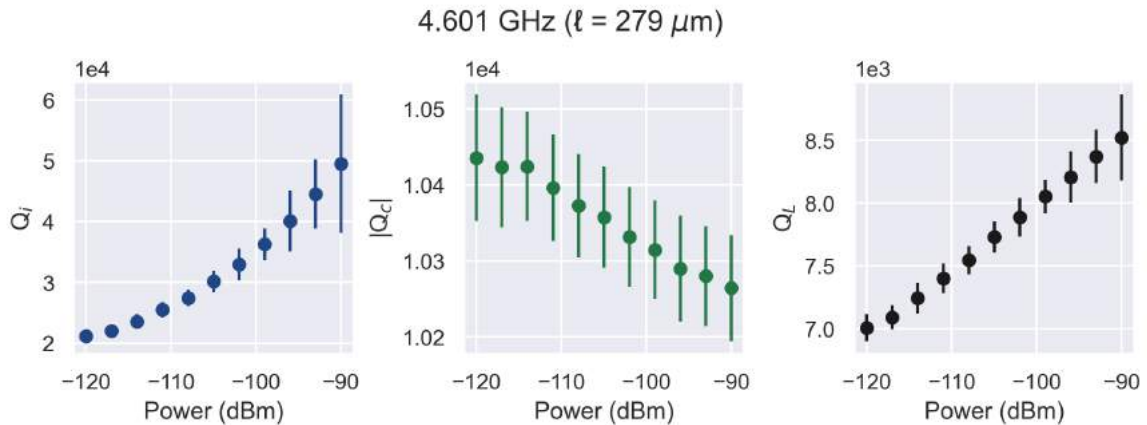


**Fig. 5.2: Quality Factors as Function of Input Power.** Here shown are the internal quality factor  $Q_i$ , the loaded quality factor  $Q_L$  and the coupling quality factor  $|Q_c|$  for a resonator with inductor length  $l = 279 \mu\text{m}$  on device 1.

The estimated and measured resonance frequencies are listed in Table 4. The fabricated inductors had a width

of 470 nm. However, in order to reduce the required time for simulation, a width of 500 nm was chosen for the simulated device. This difference in inductor width  $w$  must be taken into account when setting  $L_{\square}$  for simulations. The resonator has an inductance of approximatively  $L_k = L_{\square} \cdot \ell/w$ , with inductor length  $\ell$ . To simulate, the targeted  $L_{\square} = 105$  pH in film fabrication was thus multiplied by 50/47 in order to compensate for the different geometry. Therefore, the inductance per square was set to  $L_{\square} = 112$  pH/ $\square$  for simulations. The difference between simulated and measured resonance frequency was about 120 MHz for all four resonators, indicating an actual sheet inductance of  $L_{\square} = 102$  pH/ $\square$  for the measured devices.

**Table 4: Resonance Frequencies of the Hanged Resonators.** For each resonator on device 1, inductor length  $l$ , expected resonance frequency  $f_{r,\text{sim}}$  and actual resonance frequency  $f_{r,\text{meas}}$  are listed. The expected resonance frequency stems from taking the maximum of the simulated  $S_{21}$  response in Sonnet. The actual resonance frequency was determined from  $S_{21}$  measurements by fitting with Eq. (3.1).

$l$ ( $\mu\text{m}$ )	$f_{r,\text{sim}}$ (GHz)	$f_{r,\text{meas}}$ (GHz)
250	5.990	6.108
279	5.557	5.650
380	4.520	4.601
500	3.627	3.691

## 5.2 Arrays

In total, five chips were measured with each one hosting a 16, 24, 32 or 64 LC resonator array in normal, trivial and topological configuration. Thus, in total, 15 devices were measured. The results presented in the main text summarise the principal findings of the measured arrays. To avoid redundancy, for each finding, the results are shown for only one chip. A complete overview can be found in appendix C.

### 5.2.1 Influence of Geometry of Feedline on Transmission Spectrum

For the 16 resonator array, two different types of feedline geometry were investigated. In a first step, a feedline providing high capacitive coupling was implemented (see Fig. 5.3, bottom left) to ensure that a transmission signal could be recorded. Indeed, 16 peaks could be observed in the transmission spectrum for all three configurations. However, this kind of geometry leads to an asymmetric coupling environment of the first and last resonator in comparison to the “bulk” resonators. In the transmission spectrum, this asymmetry is reflected by the peak frequencies of the HEMs, which are shifted towards the upper middle band gap edge (beginning of upper passband, see Fig. 5.3). From Microwave Office Simulations and Section 4.2.4 we observed that one obtains the most symmetric spectrum if all resonators have the same coupling environment, i.e. when the coupling of the first/last resonator to the feedline is comparable to the inter-cell coupling. This is why we designed a new kind of feedline, where a “ghost” resonator is galvanically connected to a straight feedline (see grey schematic in Fig. 5.3, top left). Measurements with this new type of feedline revealed improved symmetry of the transmission spectra as expected (see Fig. 5.3). This type of feedline was used exclusively for the following experiments with 32 and 64 resonator arrays.

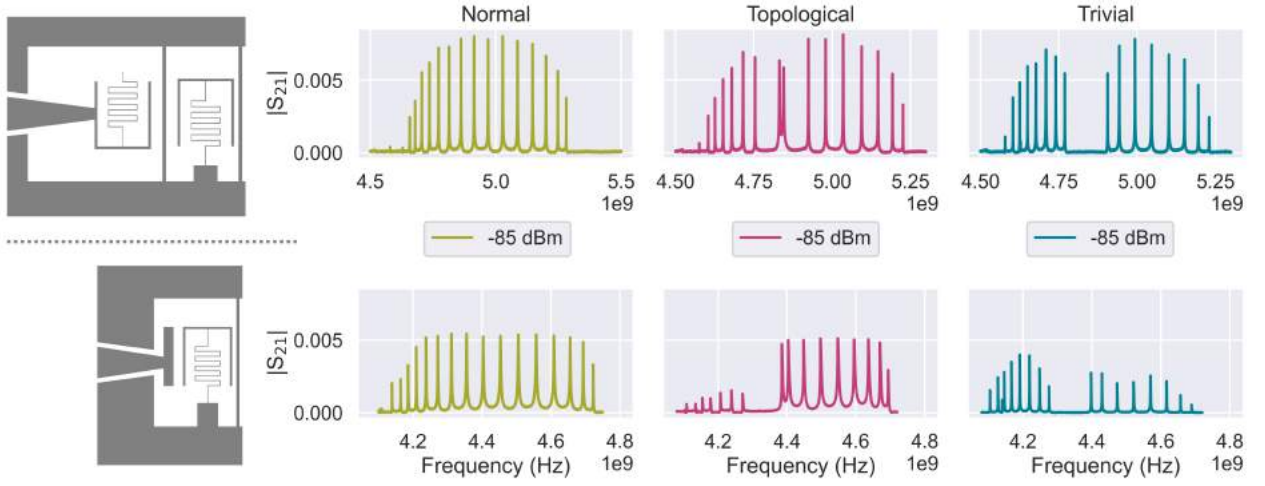


**Fig. 5.3: Influence of Feedline Geometry on  $S_{21}$  Transmission Spectra of 16 Resonator Arrays.** Top: Transmission spectra for ghost feedline (see grey schematic on left) for normal, topological and trivial configuration, recorded at -85 dBm drive power. For the topological array (magenta), the HEMs are in the center of the middle band gap, indicating that the capacitive environment of the first/last resonator is similar to the bulk resonators. Bottom: Transmission spectra for T-shaped feedline (see grey schematic on left) for normal, topological and trivial configuration, recorded at -85 dBm drive power. For the topological array (magenta), the HEMs peaks lie at the upper edge of the middle band gap.

### 5.2.2 Power Sweep

For each device, a power sweep was recorded in order to extract the loaded quality factor and to observe non-linear behaviour of those resonators. As stated in Section 2.4, non-linearity is an intrinsic property in high kinetic inductance thin films. With the VNA, the lowest drive power we could still measure was -120 dBm. The arrays generally conform to a linear description between -78 and -120 dBm drive power. In Fig. 5.4,  $|S_{21}|$  transmission profiles are plotted for different drive powers for the 16 resonator array with “ghost” feedline geometry. They are displaced by an offset to improve readability. Throughout the whole powersweep, all 16 peaks were visible for all three configurations. The powersweeps for the other arrays can be found in appendix C. They exhibit similar behaviour.

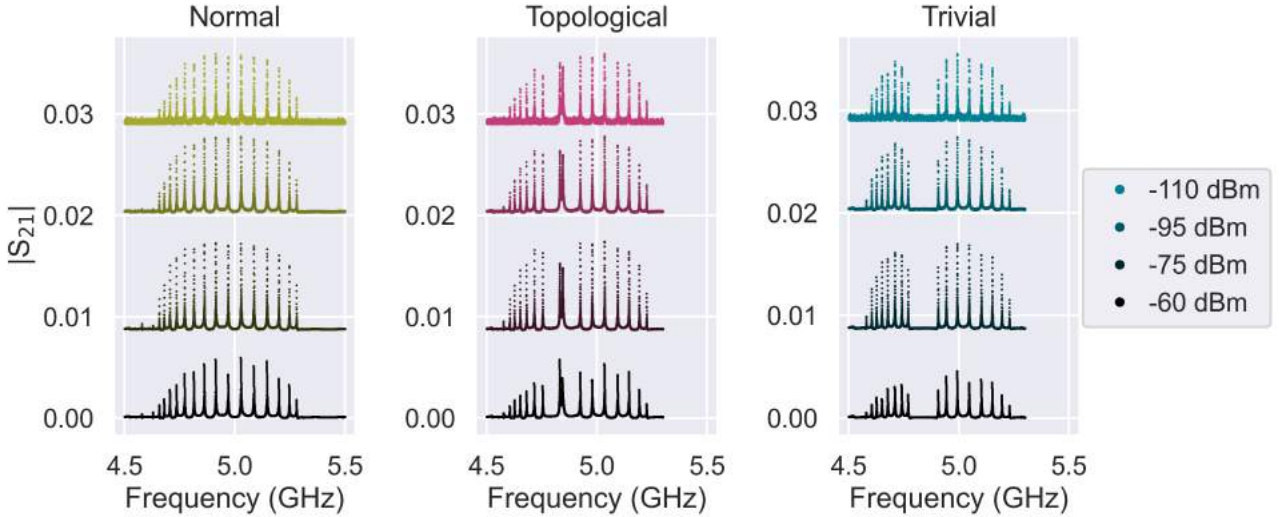


**Fig. 5.4: Power Sweep Measurement of 16 Resonator Array in Normal, Trivial and Topological Configuration.** The transmission amplitude  $|S_{21}|$  is plotted for different drive powers. The non-linearity of the system influences the peak shape for high drive powers. We introduced an offset between datasets for readability.

To better illustrate the non-linearity of the arrays, a powersweep on the HEMs of the 24 resonator array is plotted in Fig. 5.5. The splitting between the two peaks is distinct. The lower-frequency peak is more shifted with increasing drive power than the upper-frequency one, because it is more coupled to the feedline used to drive them in this measurement. It can be seen in Fig. 5.5b that for higher power, the transmission peaks get deformed and do not follow a Lorentzian curve shape any more, due to non-linearity emerging.

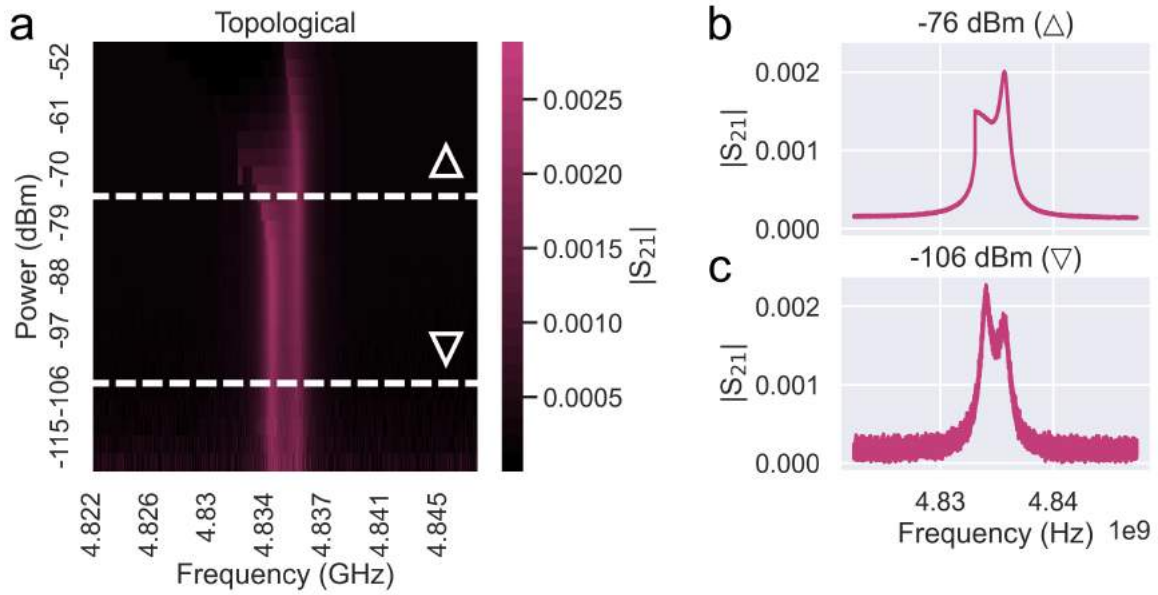


**Fig. 5.5: Power Sweep of 24 Array HEMs.** a) The transmission amplitude  $|S_{21}|$  as a function of drive power and frequency. The shifting of the HEMs for high drive powers is an indication of the non-linearity of the system. b/c) Linecut of a) at -76/-106 dBm drive power. The peak shapes differ from each other, a result of the non-linearity of the metamaterial.

### 5.2.3 Comparison to Simulation

The measurements were compared to simulated transmission and reflection spectra from Sonnet. Following the same argumentation as in Section 5.1, the  $L_{\square}$  for simulations was set to  $(125, 112)$  pH /  $\square$  for the (16,32) resonator array. In Fig. 5.6, a measured transmission spectrum of a 16 resonator array (top) is compared to the simulation (bottom). For a 32 resonator array, transmission and reflection spectra are plotted in Fig. 5.7. Qualitatively, simulation and measurement exhibit several common signatures. First, their passband envelope shapes match for both arrays and all three configurations. All passbands have their transmission minima at the edges, while the maxima lie in the passbands. Second, for the trivial and topological configuration, they both exhibit lower transmission amplitude for the lower-frequency passband section relative to the higher-frequency passband. Third, the HEM transmission amplitude for the topological 32 resonator array is small in both measurement and simulation, but high in the topological 16 resonator array. On the other hand, in reflection, the topological 32 resonator array features a prominent HEM for both measurement and simulation. Fourth, in both measurement and simulation, the lower passband looks compressed in comparison to the upper passband for the trivial and topological configurations. This is attributed to non-negligible second-neighbour coupling in our arrays, as illustrated in Fig. 4.5.

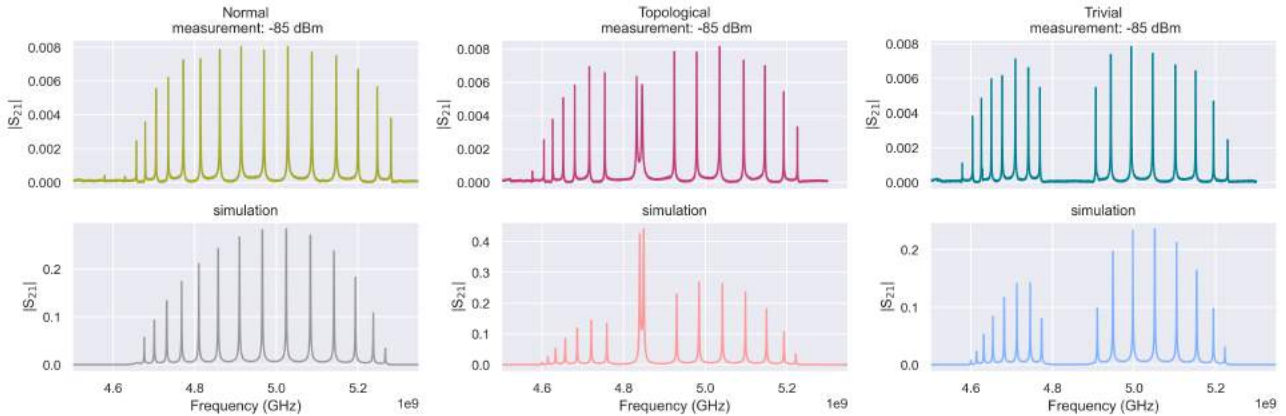


**Fig. 5.6: Measured and Simulated Transmission Spectra for 16 Resonator Array in Normal, Trivial and Topological Configuration.** Core features, such as envelope shape, transmission behaviour and shape of upper and lower passband, of the simulated spectra could be observed in measured data as well. Top: Measured  $S_{21}$  amplitude for -85 dBm drive power. Bottom: Simulated  $S_{21}$  amplitude for a superconducting material with  $L_{\square} = 125$  pH /  $\square$  and  $\tan \delta = 10^{-7}$  tangential loss.



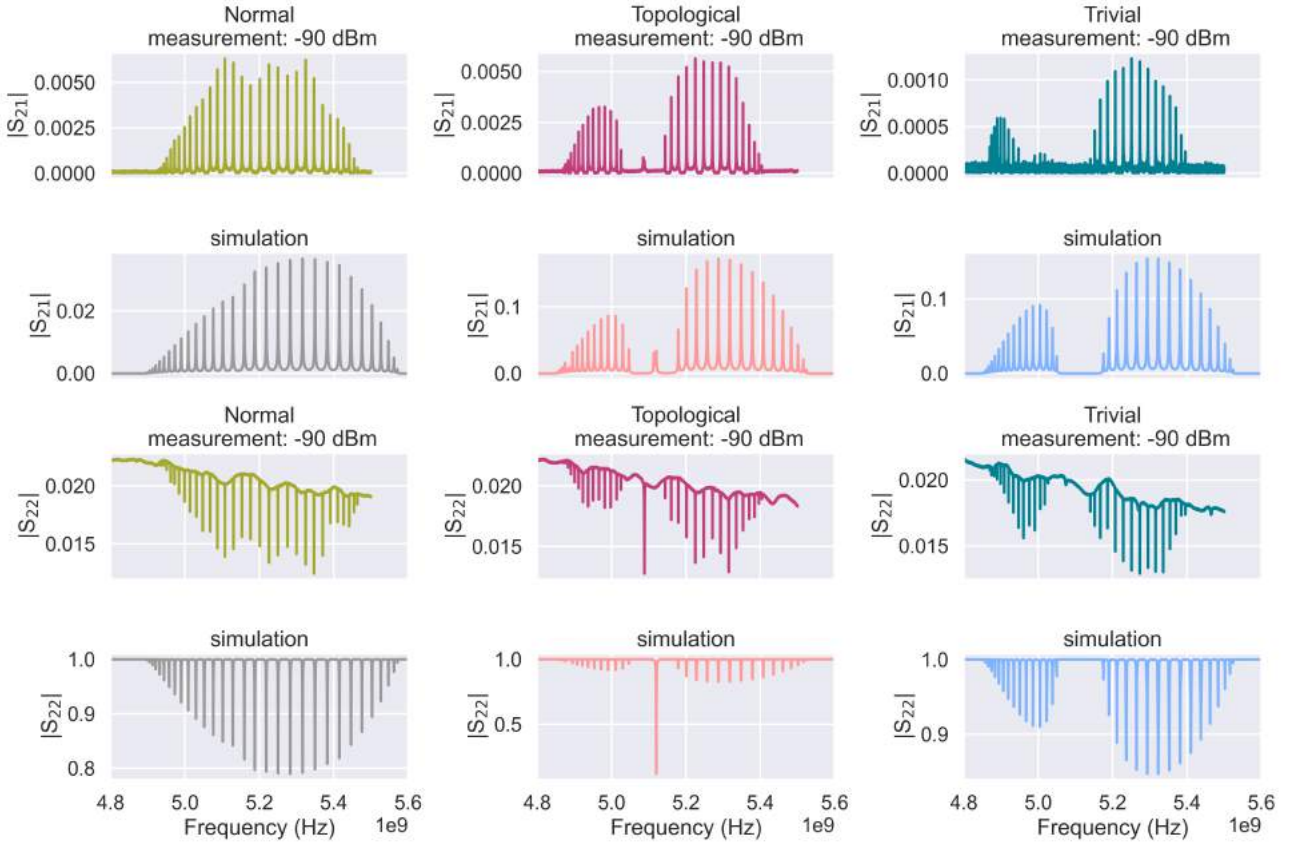


**Fig. 5.7: Transmission and Reflection Spectra for 32 Array in Normal, Trivial and Topological Configuration.** First row: Measured  $S_{21}$  amplitude for -90 dBm drive power. Second row: Simulated  $S_{21}$  amplitude for a superconducting material with  $L_{\square} = 112$  pH /  $\square$  and  $\tan \delta = 10^{-7}$  tangential loss. Third row: Measured  $S_{22}$  amplitude for -90 dBm drive power. Fourth row: Simulated  $S_{22}$  amplitude for a superconducting material with  $L_{\square} = 112$  pH /  $\square$  and  $\tan \delta = 10^{-7}$  tangential loss. For both reflection and transmission spectra, simulation and measurement agree on core features such as pass band shape, relative amplitude height of HEMs in comparison to pass band peak amplitudes and compression of the lower passband due to second-neighbour coupling.

The discrepancy in the lower part of the passband measured in the trivial configuration of the 32 resonator array (see petrol blue curve in the first row of Fig. 5.7) likely stems from a defect in the microwave feedline of port 1, for the tested device. This can be seen in the third row of Fig. 5.7, where the reflection profile from microwave port 2 is plotted (petrol blue curve). All modes are clearly visible, which indicates that the device is working properly.

#### 5.2.4 Decay Rate and Density of States

By fitting each transmission peak with a Lorentzian (see Eq. (3.2)), its central frequency  $f_p$  and line width  $\kappa_{tot}$  were extracted. Fitting was applied to data between -78 and -120 dBm drive power. Above -78 dBm, the peaks were shifted due to non-linear effects prevailing (see Fig. 5.5). In Fig. 5.8, the values are plotted for the 32 resonator array. The values at the band edges diverge since the fit protocol fitted those peaks with a broader shape than they actually were (see Fig. 5.8c). The peaks at the band edges have a significantly lower amplitude in comparison to the ones in the centre of the passbands. This reduces the accuracy of the fit, as the background noise becomes comparable in amplitude with the peaks themselves. In Fig. 5.8, only values of  $\kappa_{tot}$ , where the error is less than 10% of the value, are considered. The decay rates  $\kappa_{tot}$  for all three configuration lie between 3.4 and 0.14 MHz. The HEMs of the topological array exhibit higher decay rates than pass band modes, because they are localised at the resonators at the edge and thus couple more strongly to the feedline.

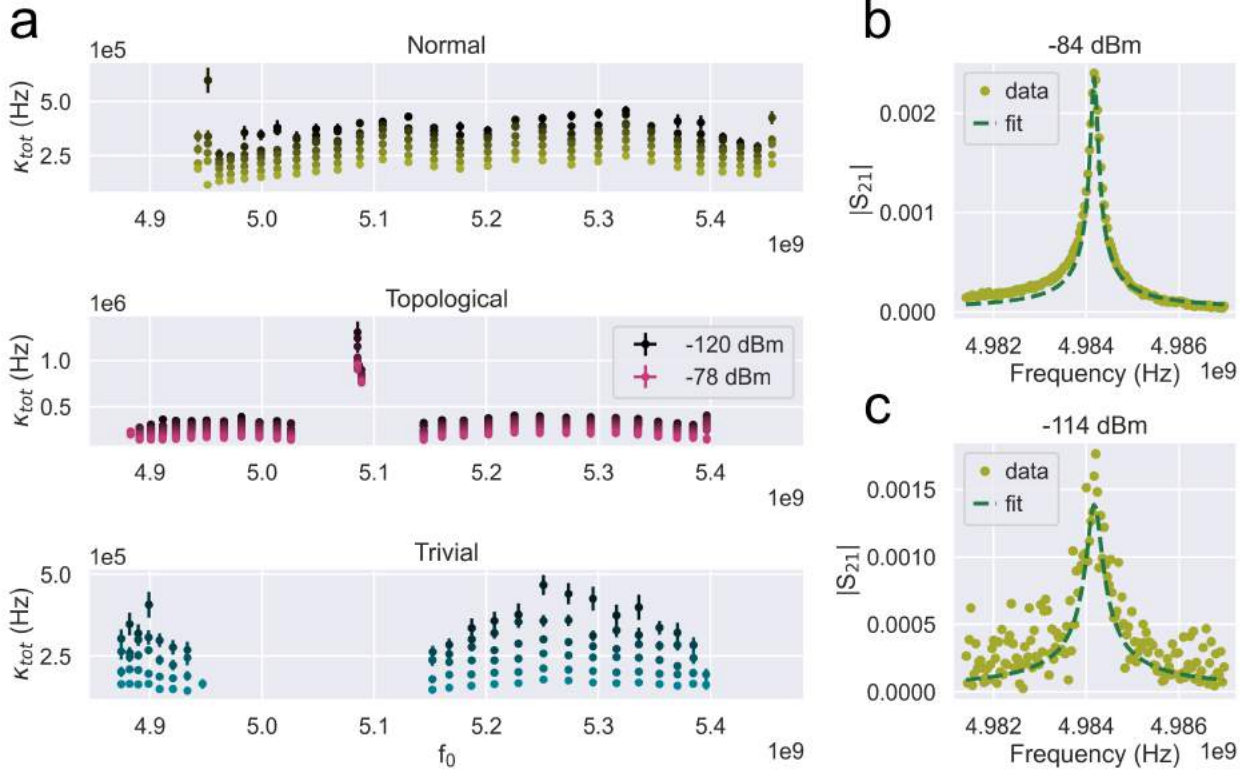


**Fig. 5.8: Total Coupling Rate  $\kappa_{tot}$  as a Function of Peak Frequency  $f_p$  for 32 Resonator Array.** a) The error bars indicate the fitting errors. Only values which have an error less than 10% of the value are included. Values at the pass band edges diverge since they are overestimated by the fit. The HEMs of the topological array exhibit high decay rate as they are directly localised at the resonator directly coupled to the feedline. b) Exemplary good fit to the data, c) for lower power and frequencies at the edge of the passband, the fit over-estimates the line width.

Plotting the differences in frequency between neighbouring peaks against peak frequency (or mode number  $n$ ) provides information on the mode density in the passband (see Fig. 5.9). In Fig. 5.9, the dot in the center of the middle band gap in topological configuration quantifies the frequency splitting of the hybridised edge modes. Table 5 summarizes information about the band structures for the different configurations, i.e. passband sizes in MHz. The passbands of the trivial and topological band structure have similar values. This is expected since they have roughly the same total capacitance and inductance, i.e. same total coupling  $J$  in the system, and the total passband span is equal to  $\approx 4J$ . For the normal configuration, the passband spans 534 MHz, giving an estimate for the coupling rate  $J \approx 133.5$  MHz, which is consistent with the estimate from dimer simulations (133 MHz, see Section 4.1). On the other hand, the extracted middle band gap for trivial (topological) configuration 119 (112) MHz, is a tad higher than estimated: In dimer simulation,  $(J_i/2\pi, J_x/2\pi) = (105, 157)$  MHz, which gives a middle band gap of  $2(157 - 105) = 104$  MHz.

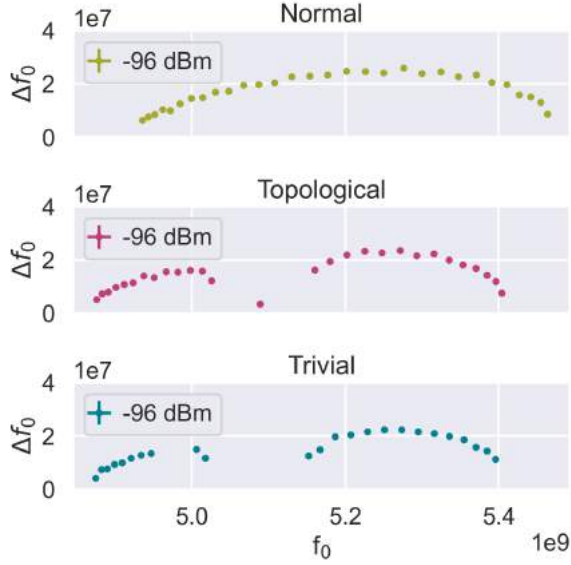


**Fig. 5.9: Frequency Spacing as a Function of Peak Frequency.** The frequency spacing  $\Delta f_0$  between neighbouring peaks is plotted against the peak frequencies  $f_0$  for the 32 resonator array. This provides information on the mode density in the passband. The value in the middle band gap of the topological configuration quantifies the HEM splitting.

**Table 5: Band Structure Values for 32 Resonator Array.** The abbreviations stand for passband (PB), lower passband (LPB), upper passband (UPB), middle band gap (BG) and splitting of HEMs (TPS). The reported values are extracted from fitted  $S_{21}$  measurements for drive powers between -78 and -114 dBm. For the passbands, the maximal value over all power spectra was taken (most likely to contain all peaks). Conversely, the minimal value was chosen for the middle band gap, following the same logic. The TPS value is the average over all obtained values. For all parameters, the extracted values lie in  $\pm 5\%$  of the listed value in the table.

Normal			
LPB (MHz)			
534			
Topological			
PB (MHz)	UPB (MHz)	BG (MHz)	TPS (MHz)
150	260	119 MHz	3.4 MHz
Trivial			
LPB (MHz)	UPB (MHz)	BG (MHz)	
157	264	112	

### 5.2.5 Evolution of Topological Peak Amplitude With Number of Resonators

The HEM transmission amplitudes decrease with increasing resonator number. In our arrays, the HEMs are still visible in the  $S_{21}$  spectrum for 32 resonators (see Fig. 5.7), but not for 64 resonators (see top middle in Fig. 5.10). This behaviour is expected since the (left and right) edge mode amplitudes are exponentially suppressed in the bulk of the resonator array. Therefore, their overlap decreases when increasing the array length. It seems that, given our device parameters, the overlap for 64 resonators is too small for their transmission in the bulk to be detected. However, since each edge mode is localised at the boundary, it should be clearly visible while measuring in reflection, from the microwave port coupled to the edge resonator. Indeed, we observe a very prominent edge mode in  $S_{22}$  reflection measurements (see bottom of Fig. 5.10). Since there is no detectable overlap between the two edge modes, only the left edge mode is probed in  $S_{22}$  reflection. For  $S_{11}$ , the right edge mode is visible (see appendix C.5, Fig. C.12)).



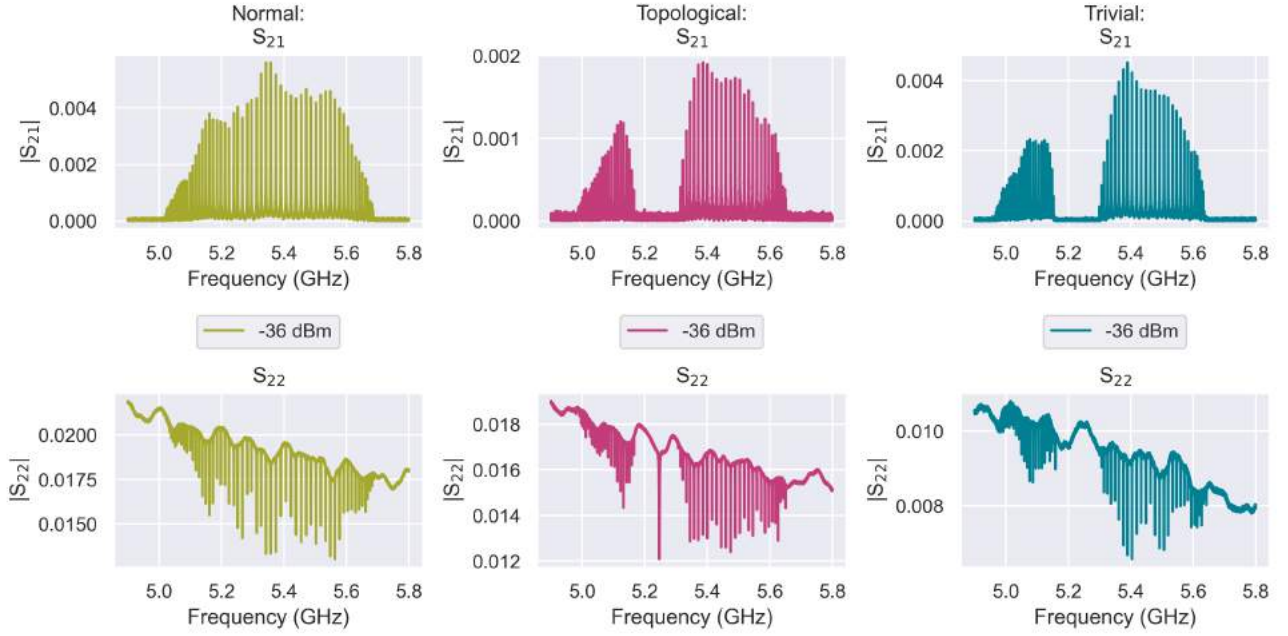


**Fig. 5.10: 64 Resonator Array in Transmission and Reflection.** All data was recorded at -96 dBm drive power. Top:  $S_{21}$  transmission amplitude, bottom:  $S_{22}$  reflection amplitude. In reflection, standing waves in the measurement line affect the baseline. In the topological array, no state is visible in the middle band gap for transmission, but can be probed in reflection since it is localised at the boundary (compare black arrows).

While the HEMs vanish in transmission for  $N = 16, 32$ , they can be probed in reflection. This trend was also observed in a more recent cooldown (Fig. 5.11). For the data shown in Fig. 5.11, the signal to noise ratio is increased considerably due to adding a room temperature amplifier directly in front of the VNA (refer to Fig. 3.9 for prior set up). This permitted clean data collection at low drive powers without excessive averaging (see Fig. 5.11).

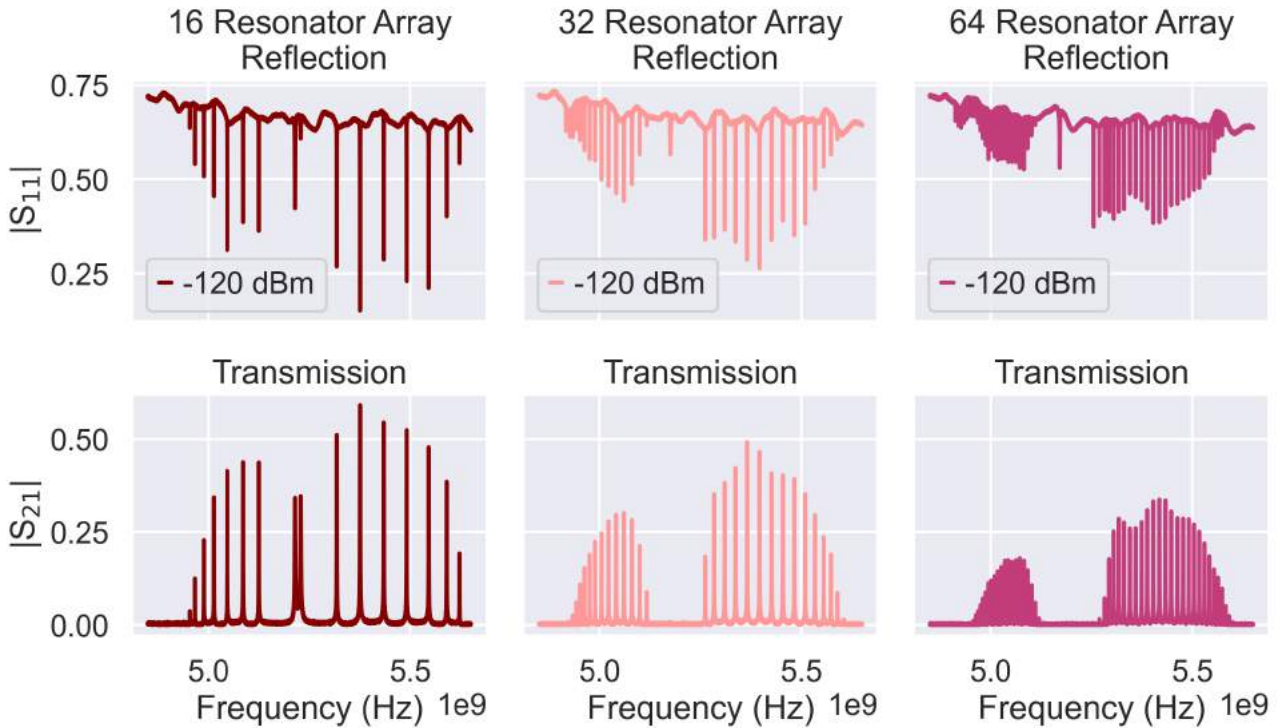


**Fig. 5.11: Topological Resonator Arrays in Transmission and Reflection.** All data was recorded at -120 dBm drive power. Top:  $S_{11}$  reflection amplitude, bottom:  $S_{21}$  transmission amplitude. From left to right, the unit cell number increases:  $N = 8, 16, 32$ .

### 5.2.6 Engineering the Band Spectrum

By varying the inter- and intra-cell spacing  $t_x, t_i$  (and thus the coupling capacitances  $C_x, C_i$ ), properties of the metamaterial such as middle band gap and passband span can be tuned.

For the data presented in this subsection, the inter- and intra-cell spacing were  $(t_x, t_i) = (8, 12) \mu\text{m}$  respectively for topological configuration and swapped for trivial configuration. The spacing was chosen to be  $t_x = t_i = 10 \mu\text{m}$  in normal configuration. In comparison to prior spacing pair of  $(t_x, t_i) = (12, 24) \mu\text{m}$ , the couplings are expected to be increased, due to over-all decreased inter-resonator spacing.

A rough estimation by eye from Fig. 5.12 gives a passband span around 760 MHz for the 32 resonator array, i.e. a coupling  $J \approx 760/4 \approx 190 \text{ MHz}$ , which is indeed higher than extracted for the normal 32 resonator array with  $t_x = t_i = 18 \mu\text{m}$  ( $J \approx 133.5 \text{ MHz}$ , see Section 5.2.4).

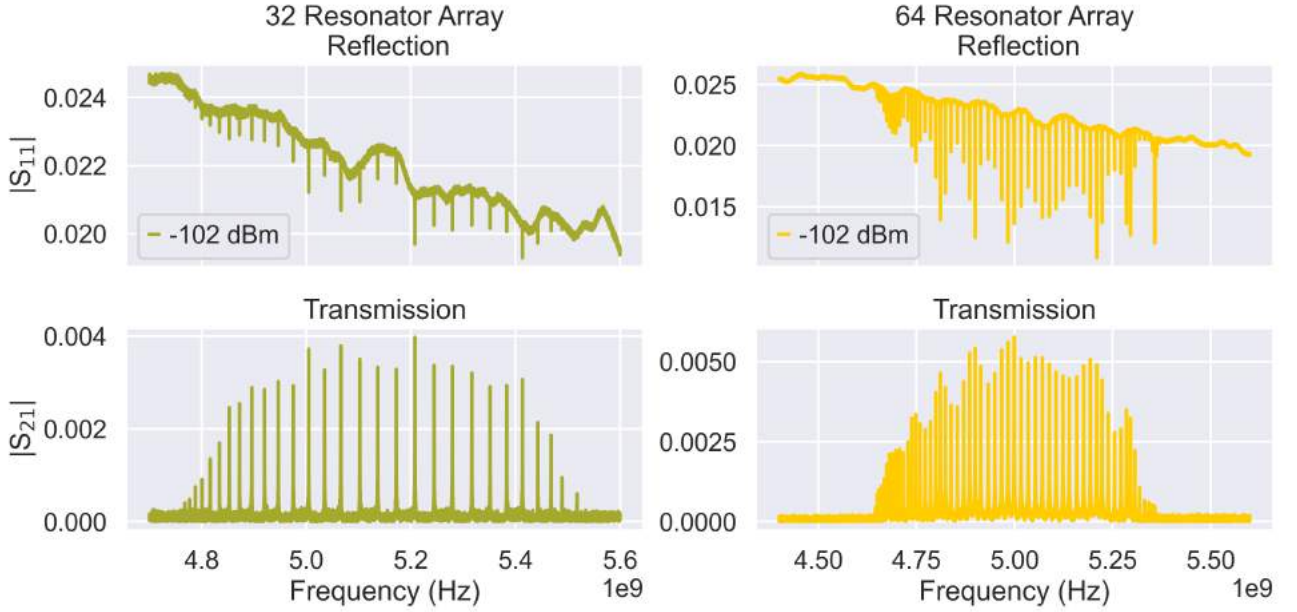


**Fig. 5.12: Normal Resonator Arrays in Transmission and Reflection.** All data was recorded at -102 dBm drive power. Top:  $S_{11}$  reflection amplitude, bottom:  $S_{21}$  transmission amplitude. From left to right, the unit cell number increases:  $N = 16, 32$ .

On the other hand, the middle band gap in trivial and topological configuration (see Figs. 5.13 and 5.14) is expected to be smaller for  $(t_x, t_i) = (8, 12) \mu\text{m}$  than  $(t_x, t_i) = (12, 24) \mu\text{m}$  because the difference in intra- and inter-cell coupling is lower. This expectation is also met, with an estimated middle band gap of (70,100) MHz for (trivial, topological) configuration (compare with Table 5, 112 and 119 MHz).

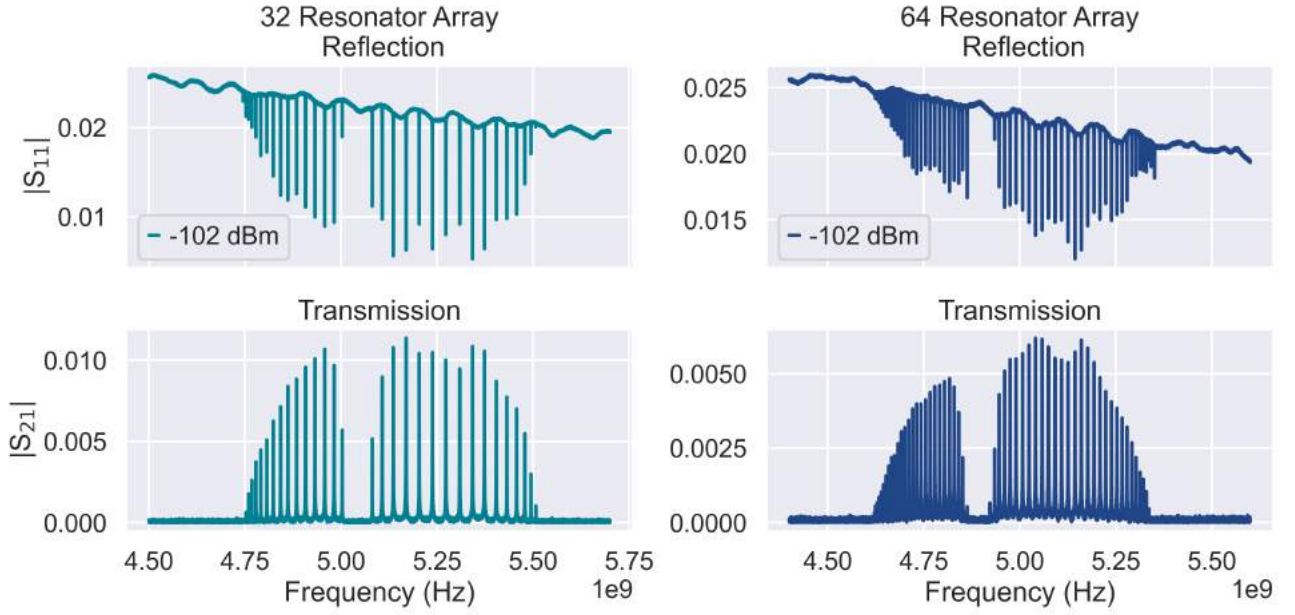


**Fig. 5.13: Trivial Resonator Arrays in Transmission and Reflection.** All data was recorded at -102 dBm drive power. Top:  $S_{11}$  reflection amplitude, bottom:  $S_{21}$  transmission amplitude. From left to right, the unit cell number increases:  $N = 16, 32$ .

Moreover, the localisation length  $\zeta$  of the HEMs in topological configuration is expected to be longer than in arrays with  $(t_x, t_i) = (12, 24) \mu\text{m}$ , because the ratio  $J_x/J_i$  is expected to be smaller. Thus, the overlap between the edge modes is, for a given  $N$ , expected to be higher in arrays with  $(t_x, t_i) = (8, 12) \mu\text{m}$ , compared to  $(t_x, t_i) = (12, 24) \mu\text{m}$ . Indeed, this seems to be the case as the HEMs have non-vanishing transmission amplitude for both  $N = 16$  and  $N = 32$  (see Fig. 5.14).

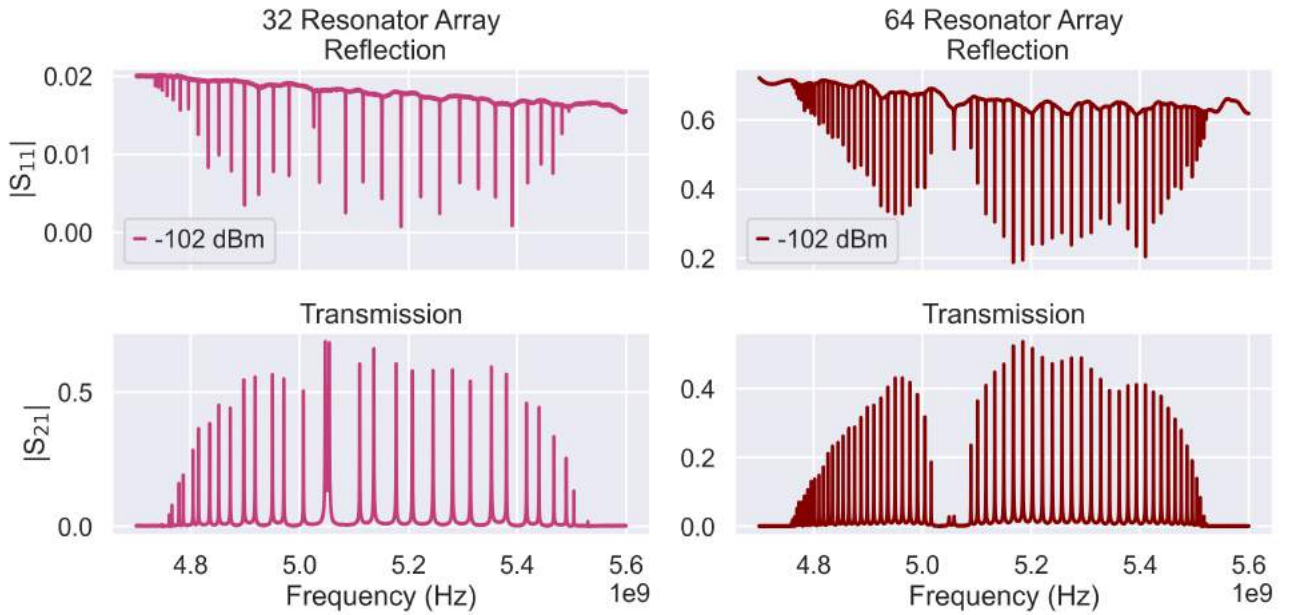


**Fig. 5.14: Topological Resonator Arrays in Transmission and Reflection.** All data was recorded at -102 dBm drive power. Top:  $S_{11}$  reflection amplitude, bottom:  $S_{21}$  transmission amplitude. From left to right, the unit cell number increases:  $N = 16, 32$ . In both arrays, the HEMs are visible.

## 6 Conclusion

After presentation and discussion of the principal findings in Section 4 and Section 5, they are briefly recapped here and conclusions are drawn.

In Section 4, the designed coupled resonator array was simulated with Sonnet. This allowed pre-fabrication engineering of the device parameters, by interpreting simulated transmission responses from the arrays. Furthermore, simulations of the current density of the array modes provided deeper insight into the underlying physics of the system. The simulations were complemented with numerical calculations from ABCD circuit models of the resonator arrays, as well as from a tight-binding Hamiltonian description. From simulation and modelling, a non-negligible second-neighbour coupling was discovered for our resonator array. The observations of Section 4 in simulation could be reproduced in measurements in Section 5.2. It is thus concluded that Sonnet simulations, as well as a lumped-element circuit model and tight-binding description of the resonator array form a well-suited tool box for understanding the coupled resonator array physics.

In Section 5, the coupled resonator arrays were probed experimentally. The internal quality factor of the resonators at low photon number lies between 10'000 and 30'000, as estimated by measuring resonators in hanged configuration in Section 5.1. For future applications, is it desirable to reach internal quality factors  $> 10^5$ . Thus, a study on loss mechanisms of our system should be a next step.

As just mentioned, the resonator array measurements were consistent with simulations. The results presented in this thesis thus provide a solid basis for further research. The investigated metamaterial allows for flexible engineering of its band spectrum by tweaking its geometrical parameters. It is a suitable platform to study the SSH model and allows exploitation of topological edge state physics.

There is room for optimisation, namely in choice of geometric parameters such as waveguide dimensions, resonator inter-spacing and resonator dimensions, to allow precise and deliberate engineering of the passband spectrum. Moreover, the influence of inter-resonator grounding ("ground strips" in Fig. 3.2) on the frequency response can be further investigated and optimised.

Furthermore, a more advanced modelling and fitting routine for the resonator arrays should be developed. In this thesis, circuit parameters for lumped-element circuit models were estimated by hand. In the future, a method to extract the circuit parameters of a given resonator array from measurement is required for more accurate modelling. The same applies for extraction of loss and coupling rates.

All in all, the metamaterial presented in this thesis is deemed a promising candidate for realisation of a bosonic multimode environment for analog quantum simulation.

## 7 Outlook

In this section, a brief overview of ongoing research in the group related to coupled resonator arrays is provided.

### 7.1 Hexagonal Lattice

Instead of restricting ourselves to one-dimension, coupled resonator arrays can also be realised in two dimensions, as an implementation of a two-dimensional SSH model with topologically protected edge states [42] and as a study of second-order topological modes [43]. For this, a hexagonal lumped-element resonator was designed, allowing the coupling of one resonator to three others. With this kind of resonator geometry, a two-dimensional resonator lattice can be built. This two-dimensional coupled resonator array was successfully fabricated (Fig. 7.1) and will be further investigated.

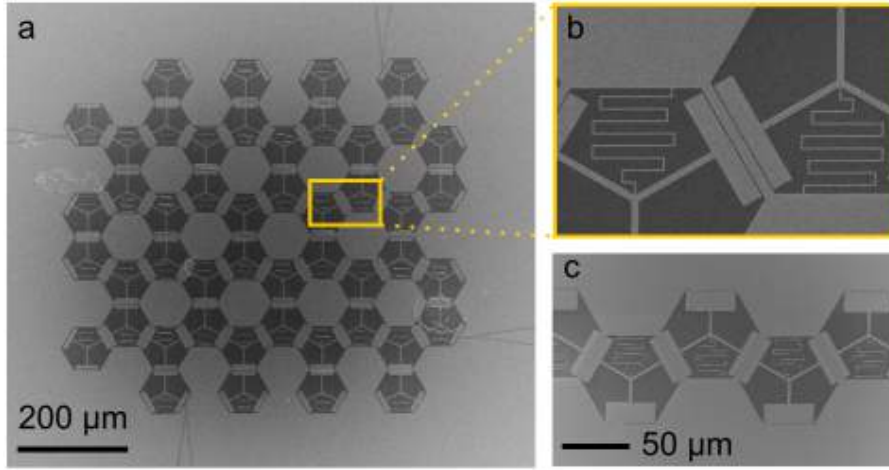


**Fig. 7.1: Hexagonal Coupled Resonator Array.** Each resonator has an inductor to ground and three capacitances for coupling. a) SEM image of a two-dimensional hexagonal resonator array. b) Zoom-in of a), showing the coupling capacitances between two resonators. c) One-dimensional hexagonal resonator array.

## 7.2 Coupling to Transmon

After a preliminary study of the implemented multimode bosonic environment, the next step is to couple it to a qubit. For this, a 88 resonator array was successfully fabricated and measured (see Fig. 7.2).

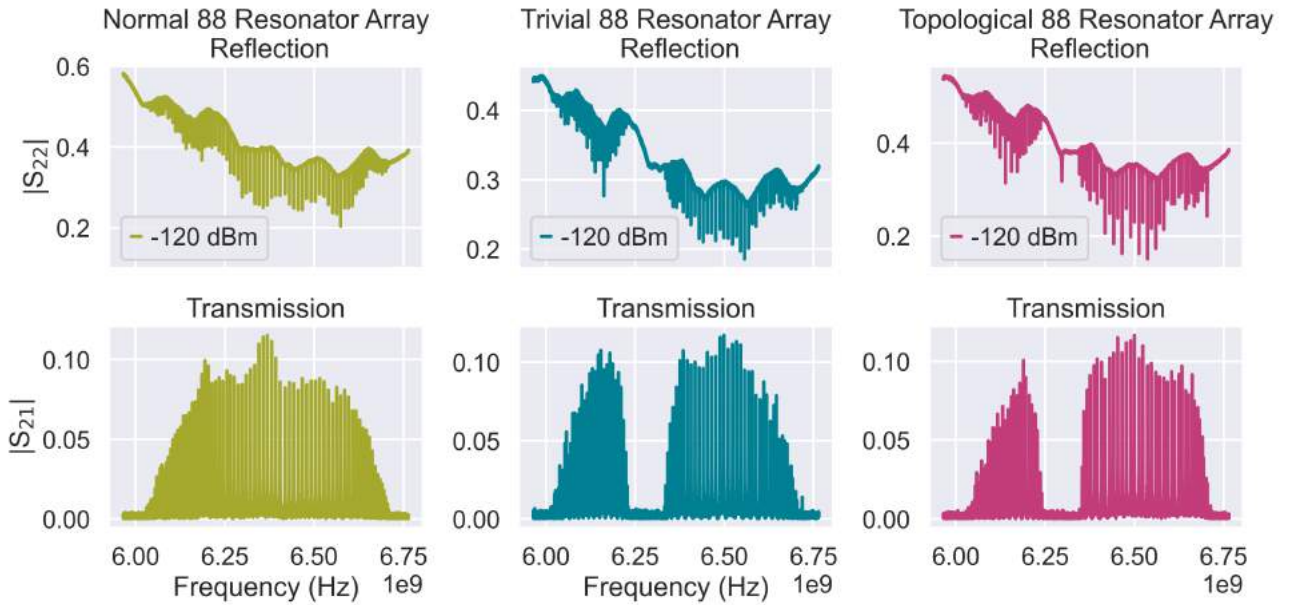


**Fig. 7.2: Reflection and Transmission Spectra for 88 Resonator Array in Normal, Trivial and Topological Configuration.** Top:  $S_{22}$  reflection amplitude spectra, recorded at -120 dBm drive power. Bottom:  $S_{21}$  transmission amplitude spectra for a drive power of -120 dBm.

Two approaches are in preparation (see Fig. 7.3). The first one is to couple a transmon to the central part of an 88 resonator array in trivial configuration. The second approach uses a cooper pair box coupled at one site to an 88 resonator array in normal configuration. The goal is to reach and study the ultra-strong coupling regime with the array.



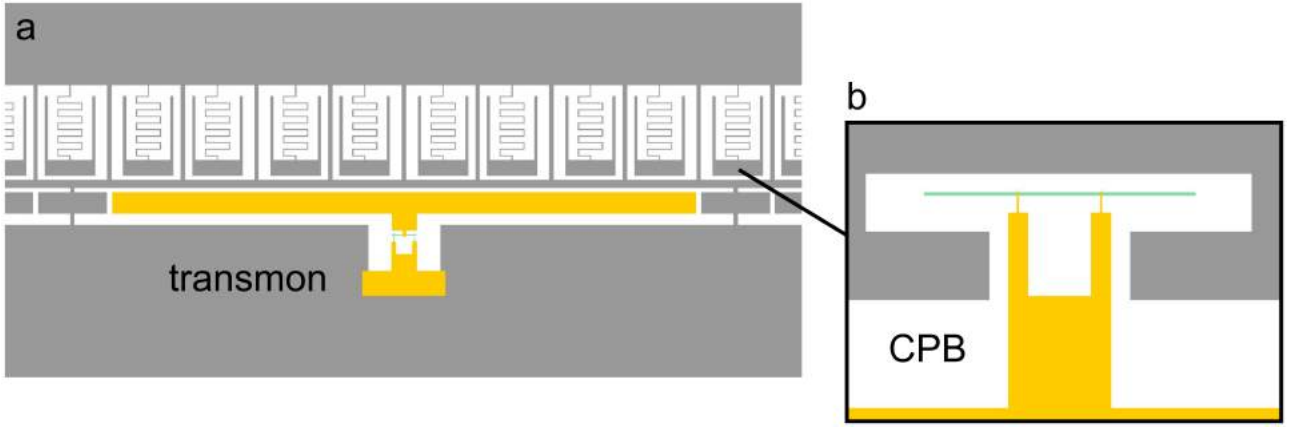


**Fig. 7.3: Coupling Resonator Array To Qubit.** a) A transmon is coupled to the central part of an 88 resonator array in trivial configuration. b) A cooper pair box can be coupled at one site to an 88 resonator array in normal configuration.

### 7.3 Study of Array Non-Linearity

As mentioned in Section 2.4 and briefly shown in Fig. 5.5, our metamaterial exhibits non-linear behaviour at high drive power (see Fig. 7.4). At high drive power, one can expect the resonators to behave like Duffing oscillators, which exhibit bistable behaviour [44]. A future goal is to exploit this property to study dissipative phase transitions [45].

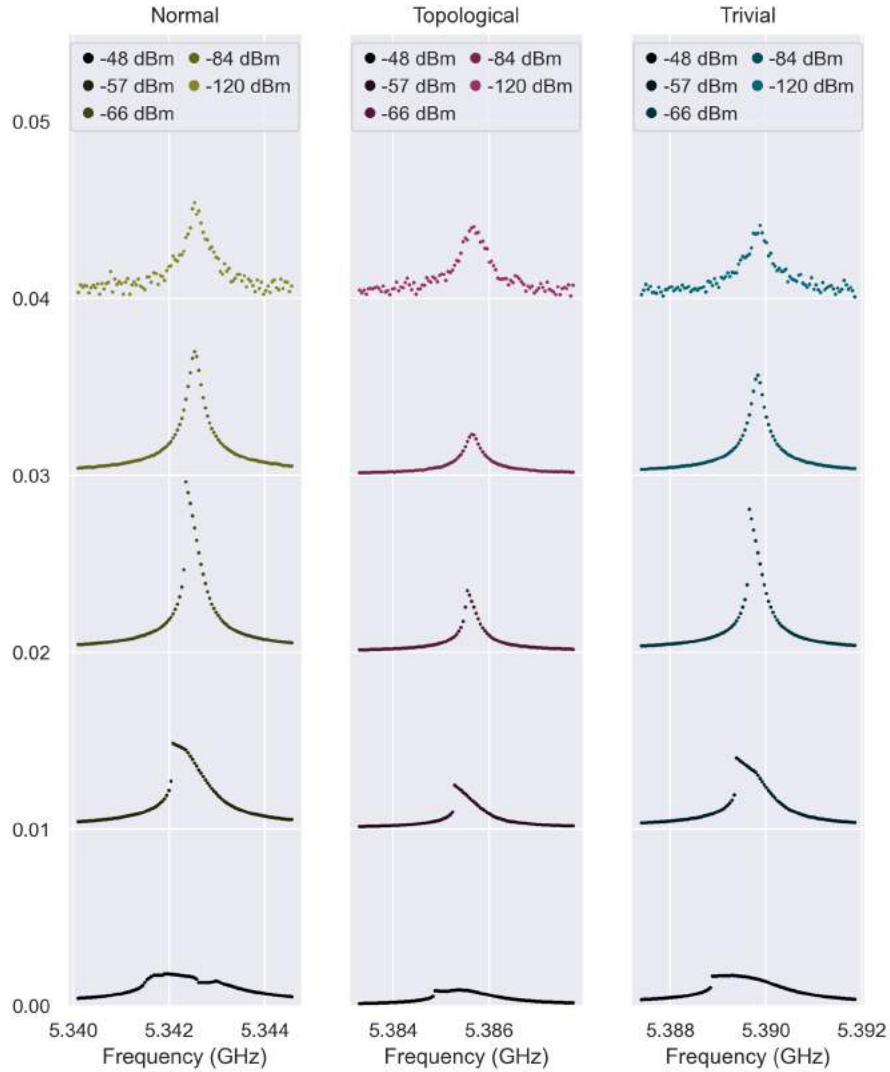


**Fig. 7.4: Non-Linearity of Resonator Arrays.** Powersweep on mode  $n = 7$  for a 64 resonator array in normal, topological and trivial configuration. For high drive powers, the peak resembles a shark fin.

## Acknowledgements

I extend my thanks to Prof. Pasquale Scarlino for giving me the opportunity to join the HQC laboratory for my master thesis and his engagement. Thank you Pasquale for putting things in context in clear explanations and providing very helpful inputs, as well proof-reading my thesis. It was a pleasure to work under/with you. I also say thank you to Vincent Jouanny for supervising my thesis, proof-reading it and working alongside me on this project. Vincent, thanks for always patiently answering all my questions, for motivating me to do my best and being a great “parter in crime”. A huge thank you goes to Simone Frasca for allowing us to make use of his superb fabrication skills and rich knowledge. Thank you Simone for investing so much time to help us do exciting science. Many thanks to Fabian Oppliger and Sebastian Cozma for fabricating the devices and helping where they could. I say “merci” to Rita Heiniger for dealing with all administrative stuff, so everything went smoothly and giving me an opportunity to brush up my rusty French. To the peoples I met at EPFL, I say thank you for making my time here an enjoyable one.

I also extend my thanks to Andrea Bancora for fruitful discussion and providing helpful input to start simulating in Sonnet and Microwave Office, as well as allowing us to use their simulation computer (K-Lab at EPFL). I thank Marco Scigliuzzo for sharing his Mathematica code for fitting and array modelling. A thank you also to Jann Hinnerk Ungerer for putting me in contact with Pasquale and Prof. Christian Schönenberger for being my first assessor from the University of Basel.

Many thanks also to my proofreaders, Michael and Alice, for their valuable corrections and inputs. Last but not least, I thank my family and my boyfriend from the bottom of my heart for being an awesome support during my thesis and encouraging me to pursue this opportunity, as well as my friends for being there for me.



## References

- [1] A. A. Houck, H. E. Türeci, and J. Koch, “On-chip quantum simulation with superconducting circuits,” *Nature Physics*, vol. 8, pp. 292–299, Apr 2012.
- [2] R. Bulla, T. A. Costi, and T. Pruschke, “Numerical renormalization group method for quantum impurity systems,” *Reviews of Modern Physics*, vol. 80, pp. 395–450, Apr 2008.
- [3] J. Kondo, “Resistance minimum in dilute magnetic alloys,” *Progress of Theoretical Physics*, vol. 32, pp. 37–49, July 1964.
- [4] K. G. Wilson, “The renormalization group: Critical phenomena and the kondo problem,” *Reviews of Modern Physics*, vol. 47, pp. 773–840, Oct 1975.
- [5] A. J. Leggett, S. Chakravarty, A. T. Dorsey, M. P. A. Fisher, A. Garg, and W. Zwerger, “Dynamics of the dissipative two-state system,” *Reviews of Modern Physics*, vol. 59, pp. 1–85, Jan 1987.
- [6] K. L. Hur, “Quantum phase transitions in spin-boson systems: Dissipation and light phenomena,” *arXiv:0909.4822 [cond-mat]*, Sept 2009.
- [7] T. Niemczyk, F. Deppe, H. Huebl, E. P. Menzel, F. Hocke, M. J. Schwarz, J. J. Garcia-Ripoll, D. Zueco, T. Hümmer, E. Solano, A. Marx, and R. Gross, “Circuit quantum electrodynamics in the ultrastrong-coupling regime,” *Nature Physics*, vol. 6, pp. 772–776, Oct 2010.
- [8] N. M. Sundaresan, Y. Liu, D. Sadri, L. J. Szöcs, D. L. Underwood, M. Malekakhlagh, H. E. Türeci, and A. A. Houck, “Beyond strong coupling in a multimode cavity,” *Physical Review X*, vol. 5, p. 021035, June 2015.
- [9] N. T. Bronn, Y. Liu, J. B. Hertzberg, A. D. Córcoles, A. A. Houck, J. M. Gambetta, and J. M. Chow, “Broadband filters for abatement of spontaneous emission in circuit quantum electrodynamics,” *Applied Physics Letters*, vol. 107, p. 172601, Oct 2015.
- [10] D. C. McKay, R. Naik, P. Reinhold, L. S. Bishop, and D. I. Schuster, “High-contrast qubit interactions using multimode cavity QED,” *Physical Review Letters*, vol. 114, p. 080501, Feb 2015.
- [11] E. Kim, X. Zhang, V. S. Ferreira, J. Banker, J. K. Iverson, A. Sipahigil, M. Bello, A. González-Tudela, M. Mirhosseini, and O. Painter, “Quantum electrodynamics in a topological waveguide,” *Physical Review X*, vol. 11, p. 011015, Jan 2021.
- [12] M. Scigliuzzo, G. Calajò, F. Ciccarello, D. P. Lozano, A. Bengtsson, P. Scarlino, A. Wallraff, D. Chang, P. Delsing, and S. Gasparinetti, “Extensible quantum simulation architecture based on atom-photon bound states in an array of high-impedance resonators,” *arXiv:2107.06852 [quant-ph]*, July 2021.
- [13] I. J. Bahl, *Lumped elements for RF and microwave circuits*. Artech House microwave library, Artech House, 2003.
- [14] D. M. Pozar, *Microwave engineering*. Wiley, 4th ed ed., 2012. OCLC: ocn714728044.
- [15] R. E. Collin, “Electromagnetic resonators,” in *Foundations for Microwave Engineering*, pp. 481–549, IEEE, 2001.
- [16] E. I. Green, “THE STORY OF Q,” *American Scientist*, vol. 43, no. 4, pp. 584–594, 1955.
- [17] C. R. H. McRae, H. Wang, J. Gao, M. Vissers, T. Brecht, A. Dunsworth, D. Pappas, and J. Mutus, “Materials loss measurements using superconducting microwave resonators,” *Review of Scientific Instruments*, vol. 91, p. 091101, Sept 2020.
- [18] H. Wang, *Fabrication and Characterization of Superconducting Metamaterial Resonators*. PhD thesis, Syracuse University, Aug 2018.
- [19] A. Megrant, C. Neill, R. Barends, B. Chiaro, Y. Chen, L. Feigl, J. Kelly, E. Lucero, M. Mariantoni, P. J. J. O’Malley, D. Sank, A. Vainsencher, J. Wenner, T. C. White, Y. Yin, J. Zhao, C. J. Palmstrøm, J. M. Martinis, and A. N. Cleland, “Planar superconducting resonators with internal quality factors above one million,” *Applied Physics Letters*, vol. 100, p. 113510, Mar 2021.
- [20] M. Scigliuzzo, *Effects of the environment on quantum systems: decoherence, bound states and high impedance in superconducting circuits*. PhD thesis, Chalmers University of Technology, 2021.

- [21] H. Wang, A. Zhuravel, S. Indrajeet, B. Taketani, M. Hutchings, Y. Hao, F. Rouxinol, F. Wilhelm, M. La-Haye, A. Ustinov, and B. Plourde, “Mode structure in superconducting metamaterial transmission-line resonators,” *Physical Review Applied*, vol. 11, p. 054062, May 2019.
- [22] S. M. Girvin, “Circuit QED: superconducting qubits coupled to microwave photons,” in *Quantum Machines: Measurement and Control of Engineered Quantum Systems* (M. Devoret, B. Huard, R. Schoelkopf, and L. F. Cugliandolo, eds.), pp. 113–256, Oxford University Press, June 2014.
- [23] W. P. Su, J. R. Schrieffer, and A. J. Heeger, “Solitons in polyacetylene,” *Physical Review Letters*, vol. 42, pp. 1698–1701, June 1979.
- [24] J. K. Asbóth, L. Oroszlány, and A. Pályi, “A short course on topological insulators: Band-structure topology and edge states in one and two dimensions,” *arXiv:1509.02295 [cond-mat]*, vol. 919, Feb 2016.
- [25] B. Pérez-González, M. Bello, I. Gómez-León, and G. Platero, “SSH model with long-range hoppings: topology, driving and disorder,” *arXiv:1802.03973 [cond-mat]*, Oct 2018.
- [26] C. X. Yu, S. Zihlmann, G. Troncoso Fernández-Bada, J.-L. Thomassin, F. Gustavo, t. Dumur, and R. Maunrand, “Magnetic field resilient high kinetic inductance superconducting niobium nitride coplanar waveguide resonators,” *Applied Physics Letters*, vol. 118, p. 054001, Feb 2021.
- [27] A. Shearrow, G. Koolstra, S. J. Whiteley, N. Earnest, P. S. Barry, F. J. Heremans, D. D. Awschalom, E. Shirokoff, and D. I. Schuster, “Atomic layer deposition of titanium nitride for quantum circuits,” *Applied Physics Letters*, vol. 113, p. 212601, Nov 2018.
- [28] N. Kirsh, E. Svetitsky, S. Goldstein, G. Pardo, O. Hachmo, and N. Katz, “Linear and nonlinear properties of a compact high-kinetic-inductance wsi multimode resonator,” *Physical Review Applied*, vol. 16, p. 044017, Oct 2021.
- [29] A. Semenov, I. Devyatov, M. Westig, and T. Klapwijk, “Effect of microwaves on superconductors for kinetic inductance detection and parametric amplification,” *Physical Review Applied*, vol. 13, p. 024079, Feb 2020.
- [30] L. H. Gabrielli, “GDSPY README.” <https://github.com/heitzmann/gdspy>, 2021.
- [31] “KLayout layout viewer and editor.” <https://klayout.de/>.
- [32] HQClabo, “High kinetic inductance metamaterial project.” <https://github.com/HQClabo/HighKineticInductanceMetamaterials>, 2021.
- [33] “Microwave office | AWR software.” <https://www.awr.com/awr-software/products/microwave-office>.
- [34] “Sonnet Suites version 17.56 - Sonnet Software.” <https://www.sonnetsoftware.com/products/sonnet-suites/>.
- [35] “Sonnet user’s guide.” [https://www.sonnetsoftware.com/support/downloads/manuals/st\\_users.pdf](https://www.sonnetsoftware.com/support/downloads/manuals/st_users.pdf).
- [36] BlueFors Cryogenics, “User manual of BF-LD-series (version 1.5.0),” Jan 2016.
- [37] sebastianprobst, “resonator\_tools.” [https://github.com/sebastianprobst/resonator\\_tools](https://github.com/sebastianprobst/resonator_tools). original-date: 2015-09-23T17:08:36Z.
- [38] S. Probst, F. B. Song, P. A. Bushev, A. V. Ustinov, and M. Weides, “Efficient and robust analysis of complex scattering data under noise in microwave resonators,” *Review of Scientific Instruments*, vol. 86, p. 024706, Feb 2015.
- [39] N. Chernov and C. Lesort, “Least squares fitting of circles,” *Journal of Mathematical Imaging and Vision*, vol. 23, pp. 239–252, Nov 2005.
- [40] M. S. Khalil, M. J. A. Stoutimore, F. C. Wellstood, and K. D. Osborn, “An analysis method for asymmetric resonator transmission applied to superconducting devices,” *Journal of Applied Physics*, vol. 111, p. 054510, Mar 2012.
- [41] P. J. Petersan and S. M. Anlage, “Measurement of resonant frequency and quality factor of microwave resonators: Comparison of methods,” *Journal of Applied Physics*, vol. 84, pp. 3392–3402, Sept 1998.
- [42] P. Delplace, D. Ullmo, and G. Montambaux, “Zak phase and the existence of edge states in graphene,” *Physical Review B*, vol. 84, p. 195452, Nov 2011.

- [43] J. Kořata and O. Zilberberg, “Second-order topological modes in two-dimensional continuous media,” *Physical Review Research*, vol. 3, p. L032029, July 2021.
- [44] P. D. Nation, M. P. Blencowe, and E. Buks, “Quantum analysis of a nonlinear microwave cavity-embedded dc SQUID displacement detector,” *Physical Review B*, vol. 78, p. 104516, Sept 2008.
- [45] M. Fitzpatrick, N. M. Sundaresan, A. C. Li, J. Koch, and A. A. Houck, “Observation of a dissipative phase transition in a one-dimensional circuit QED lattice,” *Physical Review X*, vol. 7, p. 011016, Feb 2017.

## A Derivation of SSH Model

Su, Schrieffer and Heeger published a theoretical study on polyacetylene (see Fig. A.1) in 1979, which focussed on describing electrons hopping along this one-dimensional chain with alternating hopping amplitudes [23]. This study is now known as Su-Schrieffer-Heeger (SSH) model and can generally be employed to study spinless fermions in a one dimensional lattice with staggered hopping amplitudes. Henceforth, the spinless fermions are addressed as particles.

Following reference [24], the SSH model is introduced in this section. For the whole discussion, we use units where  $\hbar = 1$ . In the SSH model, one considers  $N$  unit cells of size  $L$ , each having two sites  $A$  and  $B$  (see Fig. A.1). Interactions between the hopping particles are neglected. The system is at zero temperature and zero chemical potential. Energies are measured relative to the Fermi energy. The staggered hopping amplitudes are denoted  $t$  for intra-cell hopping and  $\gamma t$  for inter-cell hopping, where  $t, \gamma \geq 0$  are assumed for simplicity. The states of the chain are described with  $|n, S\rangle$ , where  $n$  is the index of the unit cell ( $n \in \{1, 2, \dots, N\}$ ) and  $S \in \{A, B\}$  specifies on which site the particle resides. Now, for intra-cell hopping, in the  $n$ -th unit cell, there are two possible processes:

$$\begin{aligned} |n, A\rangle &\longrightarrow t|n, B\rangle && \implies \text{Hamiltonian term } t|n, B\rangle\langle n, A| \\ |n, B\rangle &\longrightarrow t|n, A\rangle && \implies \text{Hamiltonian term } t|n, A\rangle\langle n, B| \end{aligned} \quad (\text{A.1})$$

On the other hand, inter-cell hopping also occurs from  $B$  to  $A$  and vice versa:

$$\begin{aligned} |n, B\rangle &\longrightarrow \gamma t|n+1, A\rangle && \implies \text{Hamiltonian term } \gamma t|n+1, A\rangle\langle n, B| \\ |n+1, A\rangle &\longrightarrow \gamma t|n, B\rangle && \implies \text{Hamiltonian term } \gamma t|n, B\rangle\langle n+1, A| \end{aligned} \quad (\text{A.2})$$

The Hamiltonian is thus given by summing the processes in Eqs. (A.1) and (A.2) over all unit cell indices  $n$

$$\hat{\mathcal{H}}_{\text{SSH}} = t \sum_{n=1}^N (|n, B\rangle\langle n, A| + |n, A\rangle\langle n, B|) + \gamma t \sum_{n=1}^{N-1} (|n+1, A\rangle\langle n, B| + |n, B\rangle\langle n+1, A|) \quad (\text{A.3})$$

Note that the Hamiltonian is not taking the spin degree of freedom into account as there is no term acting on the spin. If one was to describe a real life system, two copies of Eq. (A.3) would be needed to make up the Hamiltonian for the system.

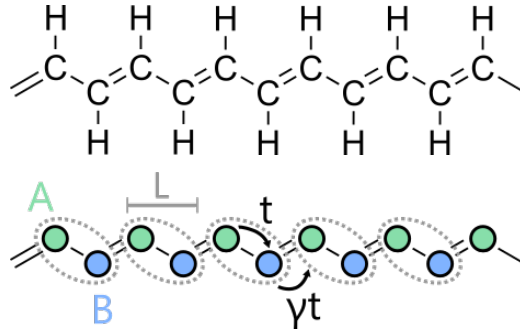


**Fig. A.1: 1D SSH Model.** Top: Chemical structure of polyacetylene, bottom: Schematic of the SSH model with sites  $A$  and  $B$  composing the unit cell (grey dotted frame). The hopping amplitudes are denoted  $t$  ( $\gamma t$ ) for intra- (inter-) cell hopping. The unit cell is of dimension  $L$ .

Using  $\{|n, S\rangle, n \in \{1, 2, \dots, N\}, S \in \{A, B\}\}$  as a basis, the Hamiltonian can be written in matrix form as

$$\mathcal{H}_{N=4} = \begin{matrix} & \begin{matrix} |1, A\rangle & |1, B\rangle & |2, A\rangle & |2, B\rangle & |3, A\rangle & |3, B\rangle & |4, A\rangle & |4, B\rangle \end{matrix} \\ \begin{matrix} \langle 1, A| \\ \langle 1, B| \\ \langle 2, A| \\ \langle 2, B| \\ \langle 3, A| \\ \langle 3, B| \\ \langle 4, A| \\ \langle 4, B| \end{matrix} & \begin{pmatrix} 0 & t & 0 & 0 & 0 & 0 & 0 & 0 \\ t & 0 & \gamma t & 0 & 0 & 0 & 0 & 0 \\ 0 & \gamma t & 0 & t & 0 & 0 & 0 & 0 \\ 0 & 0 & t & 0 & \gamma t & 0 & 0 & 0 \\ 0 & 0 & 0 & \gamma t & 0 & t & 0 & 0 \\ 0 & 0 & 0 & 0 & t & 0 & \gamma t & 0 \\ 0 & 0 & 0 & 0 & 0 & \gamma t & 0 & t \\ 0 & 0 & 0 & 0 & 0 & 0 & t & 0 \end{pmatrix} \end{matrix} \quad (\text{A.4})$$

for  $N = 4$  unit cells.

Alternatively, the unit cell index  $n$  and the site index  $S$  can be treated as external and internal degrees of freedom and the Hamiltonian can be expressed as a tensor product

$$\hat{\mathcal{H}}_{\text{SSH}} = \underbrace{\hat{\mathcal{H}}_{\text{ext}}}_{\text{basis } \{|n\rangle\}} \otimes \underbrace{\hat{\mathcal{H}}_{\text{int}}}_{\text{basis } \{|S\rangle\}} \quad (\text{A.5})$$

## A.1 Bulk Hamiltonian

For further consideration, the chain is split into bulk and boundary. The boundary denotes the two ends of the chain. The bulk is everything in between the two ends. For a long enough chain, the bulk is not influenced by the edges and can thus be treated as an infinite chain with periodic boundary conditions (Born-von Karman boundary condition). One can think of as taking the chain and closing it to form a ring. For  $N$  bulk unit cells, thus the  $(N+1)$ -th will be equivalent to the first unit cell. The bulk Hamiltonian hence becomes

$$\hat{\mathcal{H}}_{\text{bulk}} = \sum_{n=1}^N t(|n, B\rangle\langle n, A| + |n, A\rangle\langle n, B|) + \gamma t(|(n \bmod N) + 1, A\rangle\langle n, B| + |n, B\rangle\langle (n \bmod N) + 1, A|) \quad (\text{A.6})$$

where the modulo (mod) reflects the periodicity of the chain [24]. In the next step, the eigenstates  $|\Psi_l(k)\rangle$  of this Hamiltonian,

$$\hat{\mathcal{H}}_{\text{bulk}}|\Psi_l(k)\rangle = E_l(k)|\Psi_l(k)\rangle, \quad l \in \{1, 2, \dots, 2N\} \quad (\text{A.7})$$

are to be determined. Due to the periodic boundary conditions, the system possesses a translation invariance and thus, the Bloch theorem can be applied. Similar to Eq. (A.6), the eigenstates can be written as a tensor product between the internal and external degrees of freedom. After application of the Bloch theorem on the external degree of freedom (unit cell index  $n$ ), the eigenstates read

$$|\Psi_l(k)\rangle = |k\rangle \otimes |u_l(k)\rangle = \frac{1}{\sqrt{N}} \sum_{n=1}^N e^{iLnk} |n\rangle \otimes (a_l(k)|A\rangle + b_l(k)|B\rangle) \quad (\text{A.8})$$

where the wave number  $k$  takes values in the first Brillouin zone:  $k = m \cdot 2\pi/(NL)$ ,  $m \in \{-N/2, \dots, N/2\}$  [24, 42]. The eigenstates of the internal degree of freedom (site index  $S$ ) can be found upon projection of the Hamiltonian on the momentum space (i.e. applying a Fourier transformation). This bulk momentum-space Hamiltonian  $\hat{\mathcal{H}}(k)$  is given by

$$\begin{aligned} \hat{\mathcal{H}}(k) &= \langle k | \hat{\mathcal{H}}_{\text{bulk}} | k \rangle \stackrel{(\text{A.8})}{=} \left( \frac{1}{\sqrt{N}} \sum_{m=1}^N e^{-iLmk} \langle m | \right) \hat{\mathcal{H}}_{\text{bulk}} \left( \frac{1}{\sqrt{N}} \sum_{n=1}^N e^{iLnk} | n \rangle \right) = \\ &\stackrel{(*)}{=} \frac{1}{N} \sum_{n=1}^N \left( e^{-iLnk} t | B \rangle \langle A | e^{iLnk} + e^{-iLnk} t | A \rangle \langle B | e^{iLnk} + e^{-iL(n+1)k} \gamma t | A \rangle \langle B | e^{iLnk} + e^{-iLnk} \gamma t | B \rangle \langle A | e^{iL(n+1)k} \right) = \\ &= t(1 + \gamma e^{-iLk}) | A \rangle \langle B | + t(1 + \gamma e^{iLk}) | B \rangle \langle A | \end{aligned} \quad (\text{A.9})$$

using that  $\langle m | n \rangle = \delta_{mn}$  (\*). The states  $|u_l(k)\rangle$  can now be identified as the eigenstates of the momentum-space Hamiltonian,

$$\hat{\mathcal{H}}(k) |u_l(k)\rangle = E_l(k) |u_l(k)\rangle \quad (\text{A.10})$$

or in matrix form

$$\begin{aligned} H(k) &= \begin{pmatrix} 0 & t(1 + \gamma e^{-iLk}) \\ t(1 + \gamma e^{iLk}) & 0 \end{pmatrix} \\ \implies H(k) \begin{pmatrix} a_l(k) \\ b_l(k) \end{pmatrix} &= E_l(k) \begin{pmatrix} a_l(k) \\ b_l(k) \end{pmatrix} \end{aligned} \quad (\text{A.11})$$

using  $\{|A\rangle, |B\rangle\}$  as a basis. The eigenvalues  $E(k)$  of Eq. (A.11) are readily calculated using the fact that

$$H(k)^2 = \begin{pmatrix} 0 & t(1 + \gamma e^{-iLk}) \\ t(1 + \gamma e^{iLk}) & 0 \end{pmatrix} \begin{pmatrix} 0 & t(1 + \gamma e^{-iLk}) \\ t(1 + \gamma e^{iLk}) & 0 \end{pmatrix} = |t + \gamma t e^{-iLk}|^2 \begin{pmatrix} 1 & 0 \\ 0 & 1 \end{pmatrix}, \quad (\text{A.12})$$

so  $H(k)^2$  has a double eigenvalue  $E(k)^2 = |t + \gamma t e^{-iLk}|^2$ , meaning

$$E_{\pm}(k) = \pm \sqrt{|t + \gamma t e^{-iLk}|^2} = \pm t |1 + \gamma e^{-iLk}| = \pm t \sqrt{1 + \gamma^2 + 2\gamma \cos(Lk)}. \quad (\text{A.13})$$

For  $\gamma \neq 1$ , the energy dispersion has a gap

$$2\Delta = \min_k (E_+(k) - E_-(k)) = E_+(\pm \frac{\pi}{L}) - E_-(\pm \frac{\pi}{L}) = 2t|\gamma - 1|. \quad (\text{A.14})$$

The energy dispersion for different  $\gamma$  is plotted in Fig. A.2. Depending on the value of  $\gamma$ , one can distinguish between four different regimes:

- ↪  $\gamma = 0$ : The chain consists of isolated dimers, as the inter-cell hopping term  $\gamma t$  is zero. This regime is named **fully dimerised chain**.
- ↪  $0 < \gamma < 1$ : The intra-cell hopping amplitude is larger than the inter-cell hopping term. The dispersion has a gap of size  $2\Delta = 2t(1 - \gamma)$ . This regime is called **trivial**.
- ↪  $\gamma = 1$ : Intra- and inter-cell coupling are equal, the energy gap is closed. We further refer to this configuration as **normal**.
- ↪  $\gamma > 1$ : The inter-cell hopping amplitude is larger than the intra-cell hopping term. An energy gap of  $2\Delta = 2t(\gamma - 1)$  opens. This is the **topological** regime.

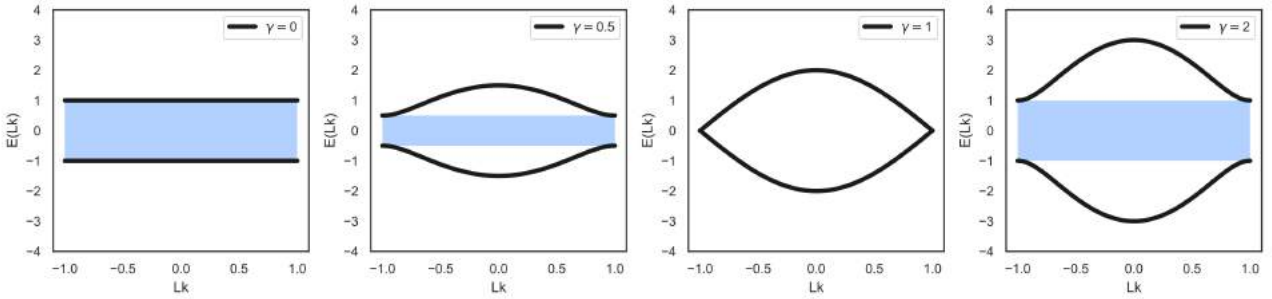


**Fig. A.2: Energy Dispersion  $E(k)$  of the Bulk SSH Model.** The energy gap is shaded in blue. The four plots correspond to four regimes, depending on the value of  $\gamma$ : fully dimerised ( $\gamma = 0$ ), trivial ( $0 < \gamma < 1$ ), normal ( $\gamma = 1$ ) and topological ( $\gamma > 1$ ).

Even though trivial and topological regime seem equivalent from looking at their dispersion relation, they exhibit fundamentally different physics. As hinted by the name, they can be distinguished topologically. For this, one defines the 3-dimensional vector  $\vec{d}(k)$  with entries

$$\vec{d}(k) = \begin{pmatrix} d_x \\ d_y \\ d_z \end{pmatrix} = \begin{pmatrix} t + \gamma t \cos(kL) \\ \gamma t \sin(kL) \\ 0 \end{pmatrix} \quad (\text{A.15})$$

This form is derived from comparing  $H(k)$  of Eq. (A.11) to the general model of a two-band system [24]:

$$H(k) = d_x(k)\hat{\sigma}_x + d_y(k)\hat{\sigma}_y + d_z(k)\hat{\sigma}_z + d_0(k)\hat{\sigma}_0 \quad (\text{A.16})$$

with the Pauli matrices  $\sigma_x, \sigma_y, \sigma_z$  and the  $2 \times 2$  identity matrix  $\sigma_0$ .

As can be seen from Eq. (A.15), the end point of  $\vec{d}(k)$  describes a circle in the  $(d_x, d_y)$  plane as  $k$  goes from  $-\pi/L$  to  $\pi/L$  through the Brillouin zone. This circle has radius  $\gamma t$  and center  $(t, 0)$ . For this circle, one can define the integer winding number  $\nu$ , which counts how many times the trajectory encircles the origin. For a radius  $\gamma t$  bigger than  $t$ , the winding number  $\nu = 1$ , as the origin lies in the circle. Using this winding number, one can now distinguish between trivial and topological regime (see Fig. A.3): For trivial,  $\nu = 0$ , whereas in the topological case,  $\nu = 1$ . In the case of  $\gamma = 1$ , the winding number is undefined as the origin is part of the loop. This winding number  $\nu$  is a so-called topological invariant: It remains unchanged under adiabatic deformations [24]. Here, it means that one cannot go from a trivial to topological configuration without closing the energy gap. This closing of the energy gap is reflected in the discontinuity in  $\nu$  at  $\gamma = 1$ .



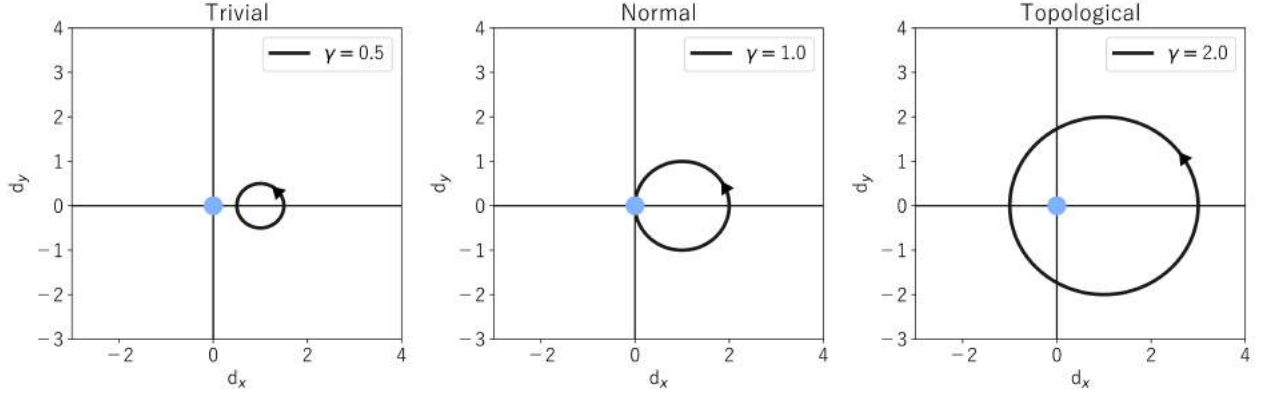


**Fig. A.3: Trajectory of  $\vec{d}$  in  $(d_x, d_y)$  Plane.** The origin is emphasised with the blue dot. Left: For  $\gamma < 1$ , the loop does not encircle the origin, so the winding number is  $\nu = 0$ . Middle: The winding number  $\nu$  is undefined for  $\gamma = 1$  as the trajectory crosses the origin. Right: For  $\gamma > 1$ ,  $\nu$  is 1 since the origin is enclosed in the circle.

## A.2 Edge States

In the topological regime, the boundary of the chain hosts two edge states. One is localised at the right end of the chain and one on the left end. The two edge states are henceforth called  $|R\rangle$  and  $|L\rangle$ . Their energy is on the order of  $E = e^{-N/\xi} \ll \Delta$ , where  $\xi$  is the localisation length

$$\xi = \frac{1}{\log((\gamma t)/t)} = \frac{1}{\log(\gamma)}. \quad (\text{A.17})$$

Their energy lies within the bulk band gap, where no states are available. Hence, the edge states decay exponentially towards the middle of the chain. State  $|R\rangle$  only has occupation on sites  $A$  whereas state  $|L\rangle$  only resides on sites  $B$ . These two edge states have an exponentially small overlap and will thus hybridise. The resulting symmetric and antisymmetric superpositions

$$|\Psi_{\text{sym}}\rangle = \frac{1}{\sqrt{2}} \left( e^{-i\phi/2} |L\rangle + e^{i\phi/2} |R\rangle \right) \quad (\text{A.18})$$

$$|\Psi_{\text{anti}}\rangle = \frac{1}{\sqrt{2}} \left( e^{-i\phi/2} |L\rangle - e^{i\phi/2} |R\rangle \right) \quad (\text{A.19})$$

$$\phi \in [0, 2\pi[$$

appear as available states in the middle of the band gap at almost zero energy. This can be seen in Fig. A.4, where the eigenvalues of the SSH Hamiltonian in Eq. (A.3) are plotted as a function of the inter-cell hopping amplitude for  $N = 8$  unit cells. The intra-cell hopping amplitude  $t$  is set to 1. For  $\gamma < 1$ , the system is in the trivial regime. Two bands with each 8 energy states are separated by a band gap. As  $\gamma \rightarrow 1$ , the two states at the edge of the band gap (index  $l = 4, 5$ ) approach each other until there is no band gap for  $\gamma = 1$ . However, for  $\gamma > 1$ , these two states converge to lie at almost zero energy and the band gap re-opens. These almost-zero energy states are the two superpositions  $|\Psi_{\text{sym}}\rangle$  and  $|\Psi_{\text{anti}}\rangle$  of the edge states  $|R\rangle$ ,  $|L\rangle$ . Their wavefunction is plotted in Fig. A.4 for  $t = 1, \gamma = 2$ .

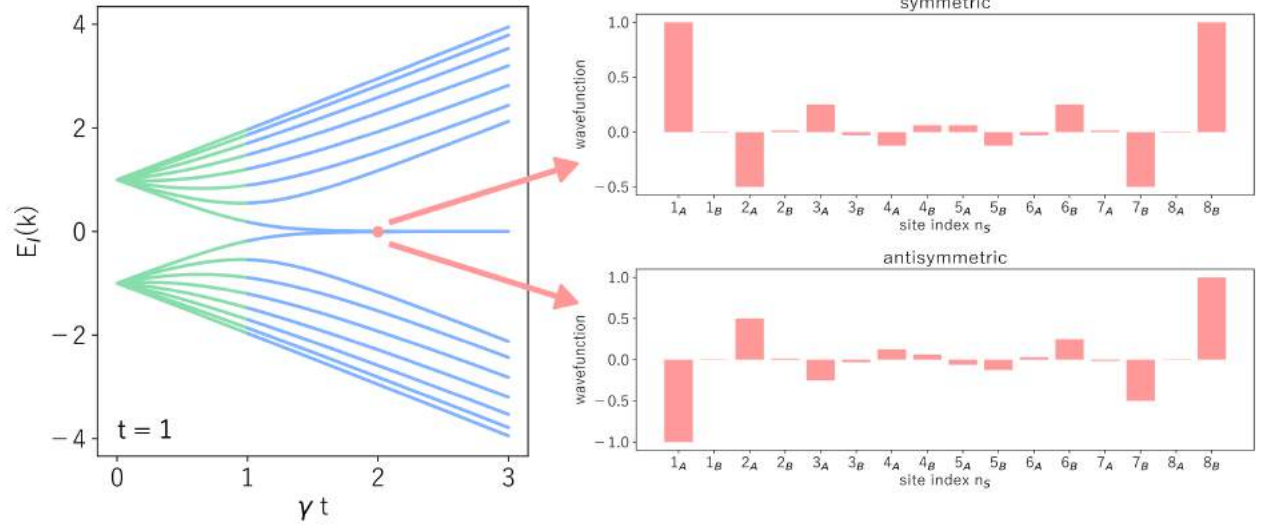


**Fig. A.4: Eigenenergies as a Function of Inter-cell Coupling.** The eigenenergies and eigenstates were calculated in Mathematica using the SSH Hamiltonian matrix for  $N = 8$ ; analogous to Eq. (A.4). Left: Eigenvalues of Eq. (A.3) as a function of inter-cell coupling  $\gamma t$ , with  $t = 1$ . For  $\gamma < 1$ , there are no edge states in the band gap (trivial regime, green). In the topological regime ( $\gamma > 1$ , blue), almost-zero-energy states appear in the middle of the band gap. Right: Wavefunction of the two almost-zero-energy states. They are the symmetric and antisymmetric superpositions of the edge states  $|L\rangle$  and  $|R\rangle$ .

## B Supplementary Simulation Data

In this appendix, supplementary current density simulation data is shown. The bar plots show the maximum current density magnitude on each site of the array, extracted from current simulations in Sonnet. Each bar plot corresponds to one mode number  $n$ .

### B.1 4 LC Array with Ghost Feedline

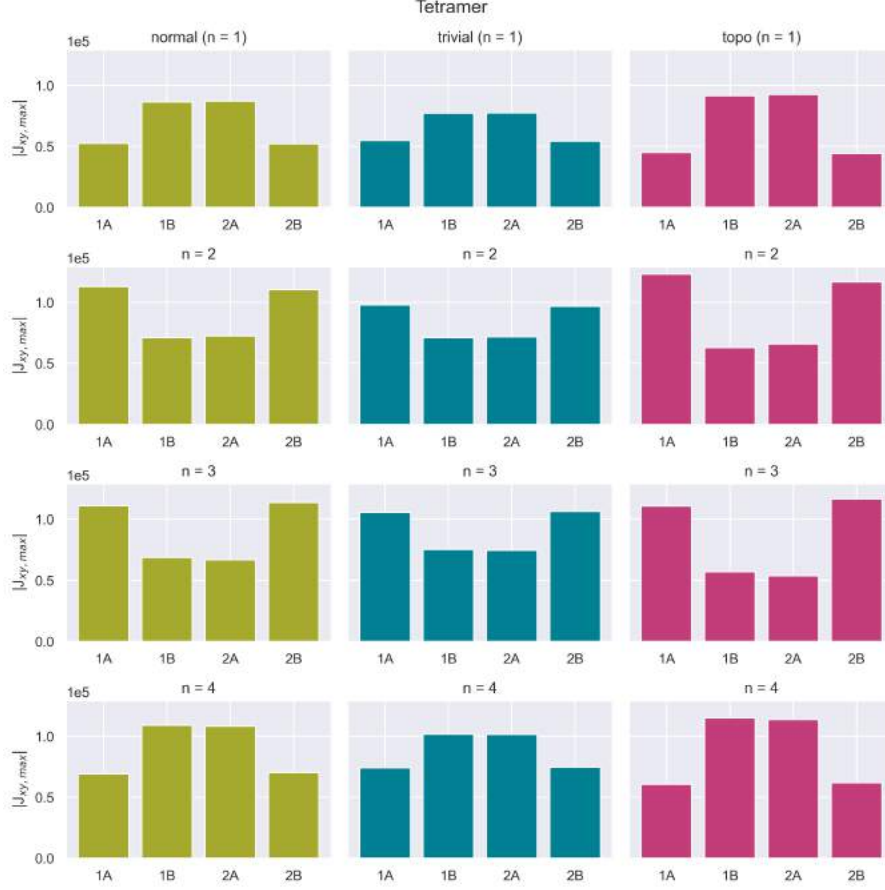


**Fig. B.1: Current Density Simulation Data for Tetramer in Normal, Trivial and Topological Configuration.** Maximal current density on each site. The sites are labelled with  $N(A, B)$  for the first (A) or second (B) position in the  $N$ -th unit cell. The index  $n$  denotes the mode number.

## B.2 16 LC Array with Ghost Feedline



**Fig. B.2: Current Density Simulation Data for 16 LC Resonator Array in Normal, Trivial and Topological Configuration.** Maximal current density on each site. The sites are labelled with  $N(A, B)$  for the first (A) or second (B) position in the  $N$ -th unit cell. The index  $n$  denotes the mode number.

## C Supplementary Measurement Data

In this section, supplementary measurement data from both hanged resonator and resonator arrays are shown.

### C.1 Hanged Resonators

In this section, all extracted quality factors for both measured devices are plotted.

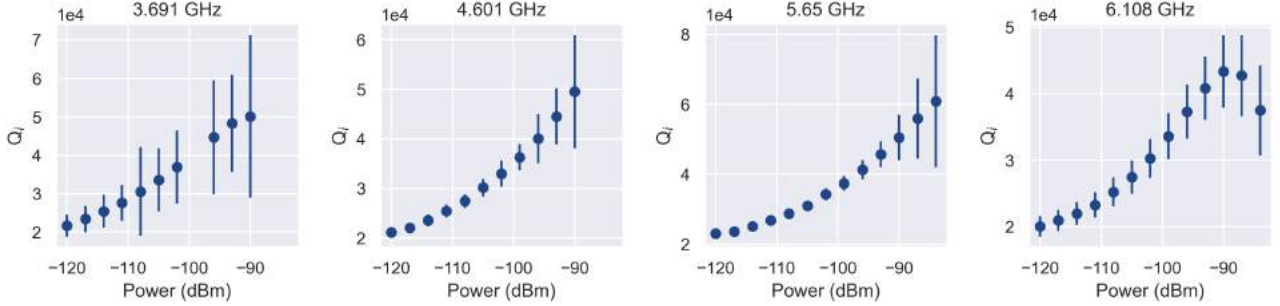


Fig. C.1: Internal Quality Factor versus Input Power for Device 1.

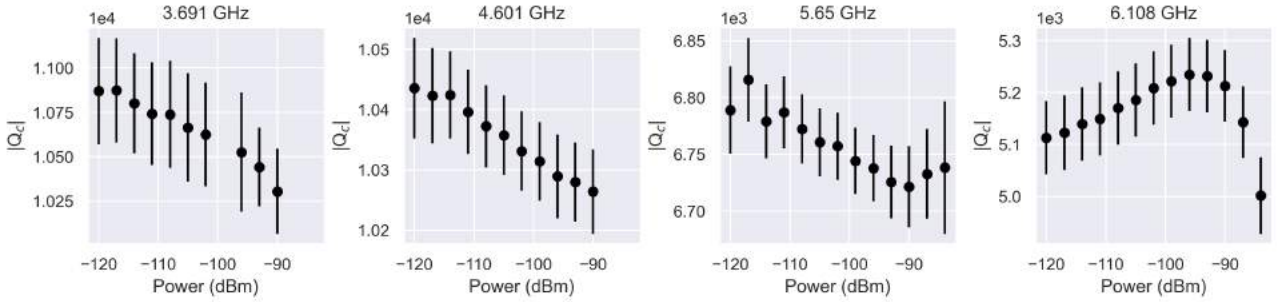


Fig. C.2: Coupling Quality Factor versus Input Power for Device 1.

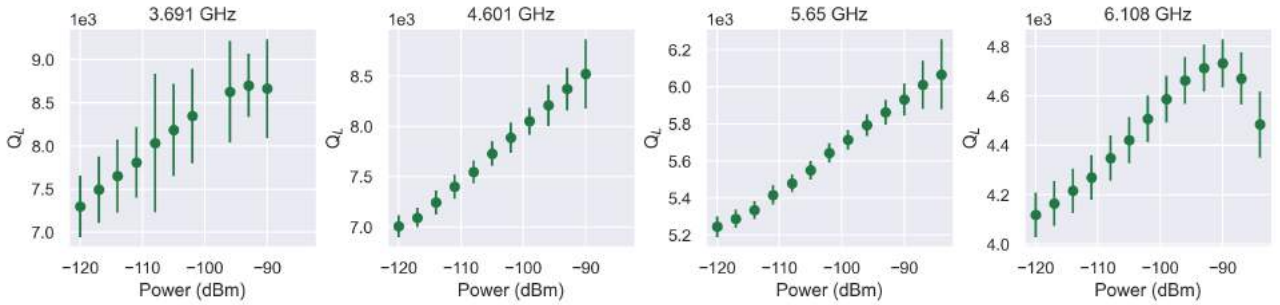


Fig. C.3: Loaded Quality Factor versus Input Power for Device 1.

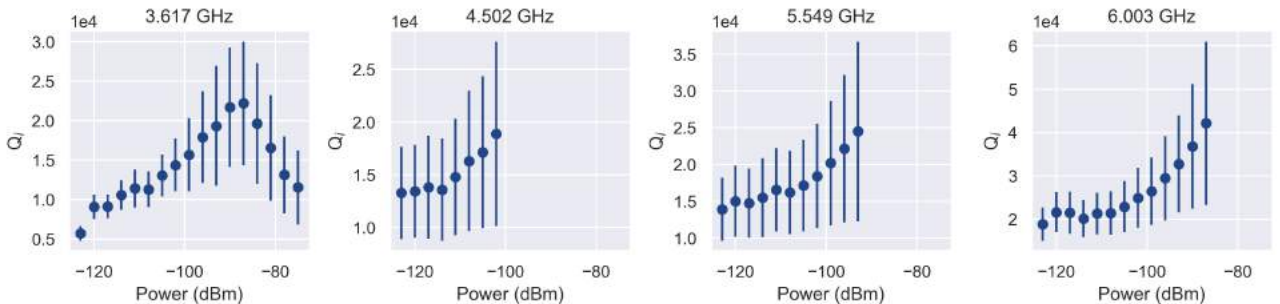


Fig. C.4: Internal Quality Factor versus Input Power for Device 2.



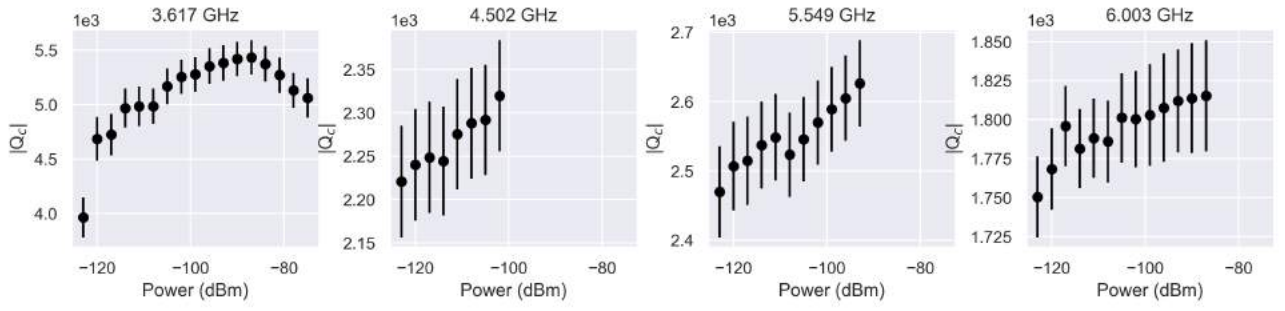


Fig. C.5: Coupling Quality Factor versus Input Power for Device 2.

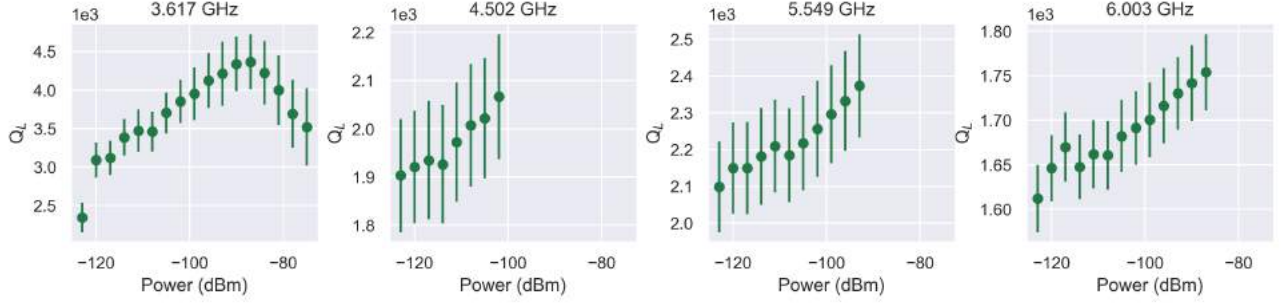


Fig. C.6: Loaded Quality Factor versus Input Power for Device 2.

## C.2 16 LC Array with T-shaped Feedline

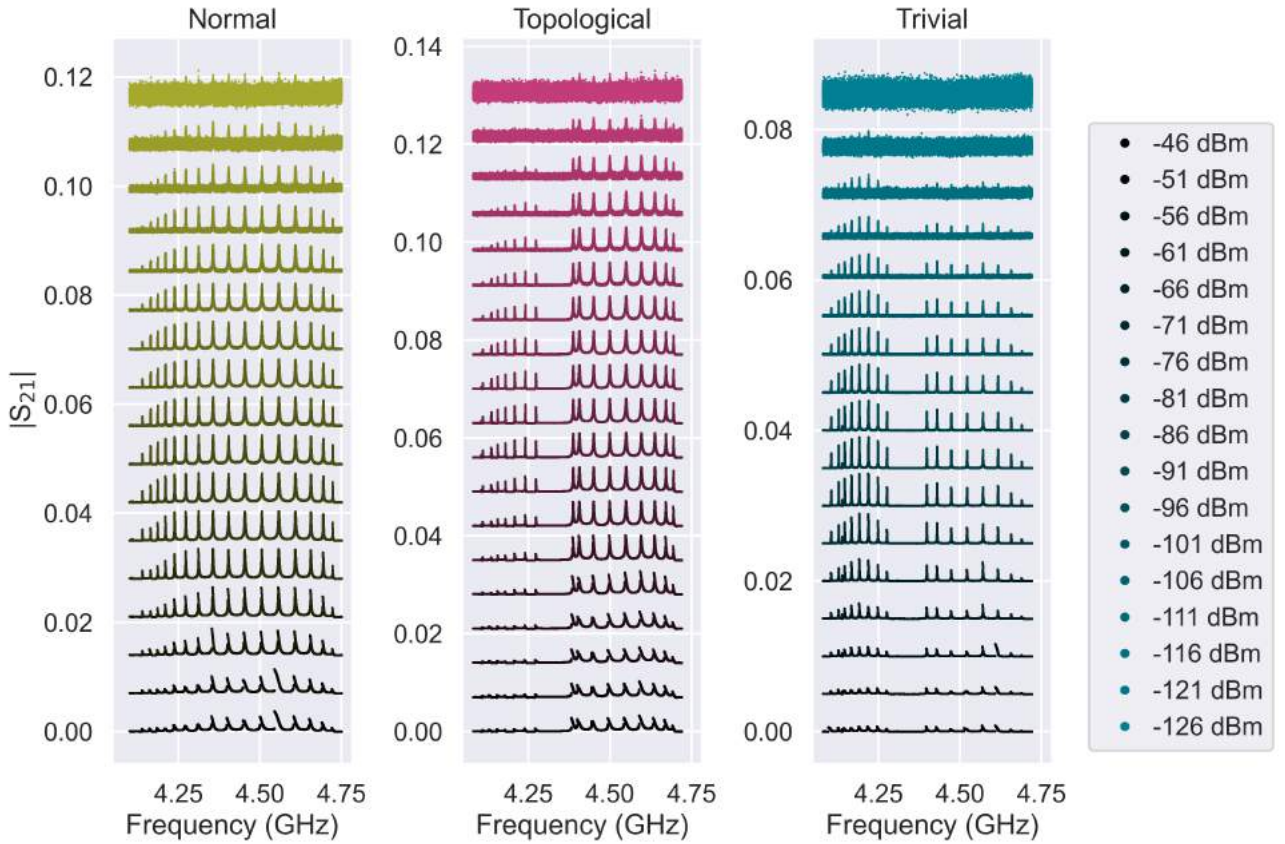


Fig. C.7: Power Sweep of 16 Resonator Array with T-shaped Feedline.



### C.3 16 LC Array with Ghost Feedline

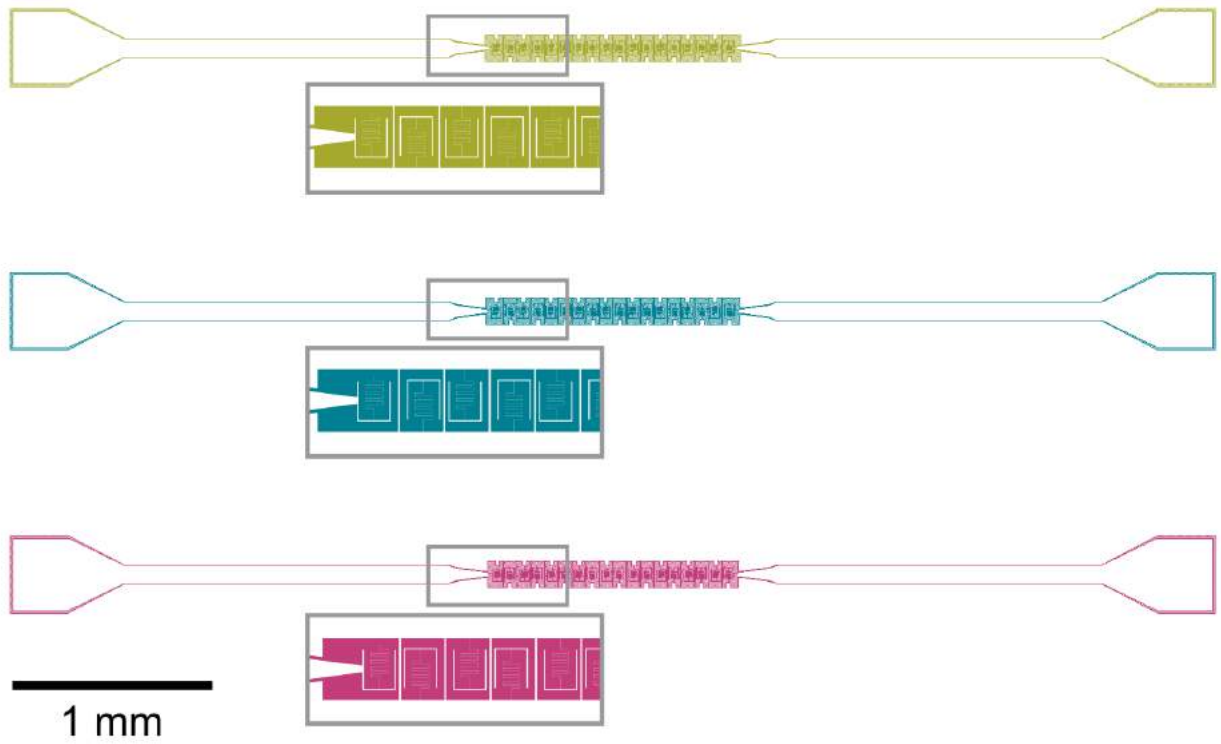


Fig. C.8: EBL Mask for Etching the 16 Resonator Arrays.

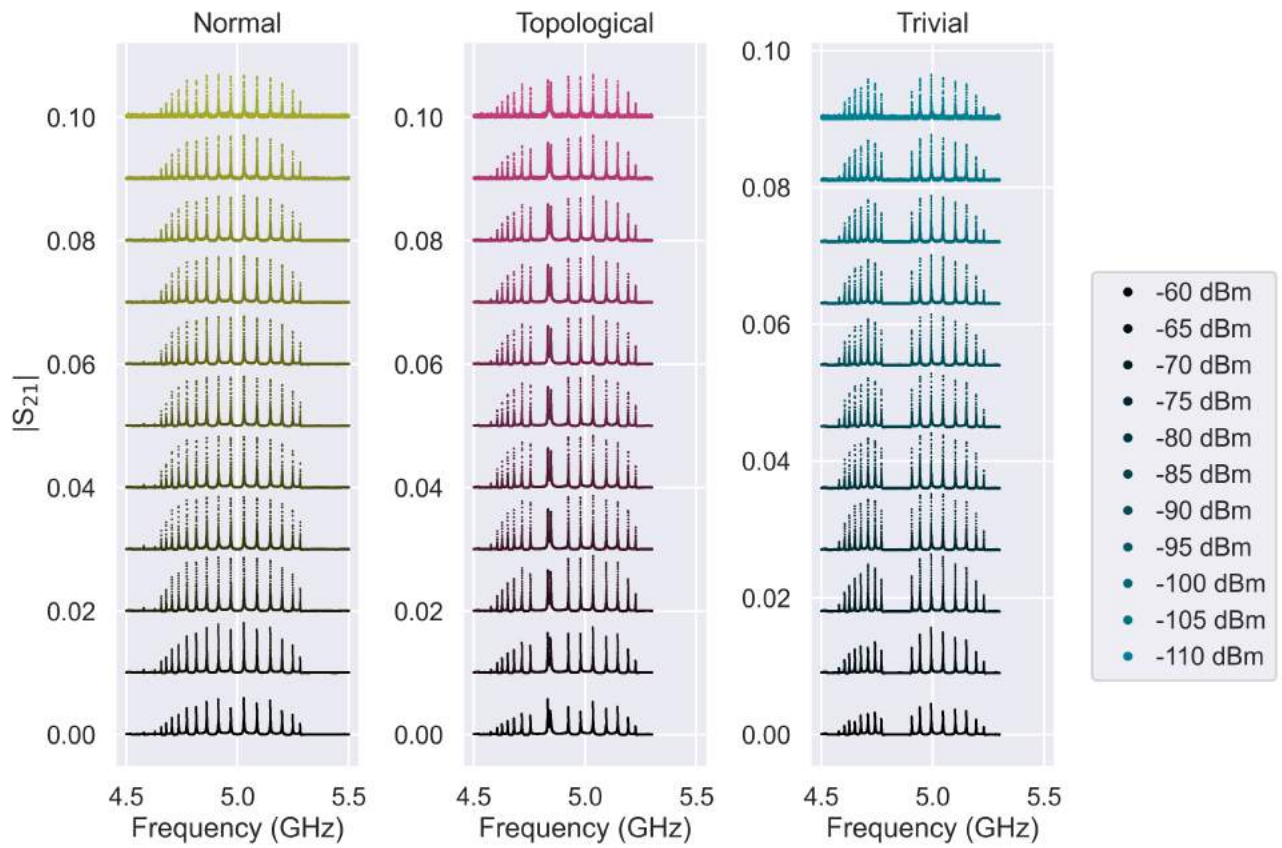


Fig. C.9: Power Sweep of 16 Resonator Array with Ghost Feedline.

## C.4 32 LC Array with Ghost Feedline

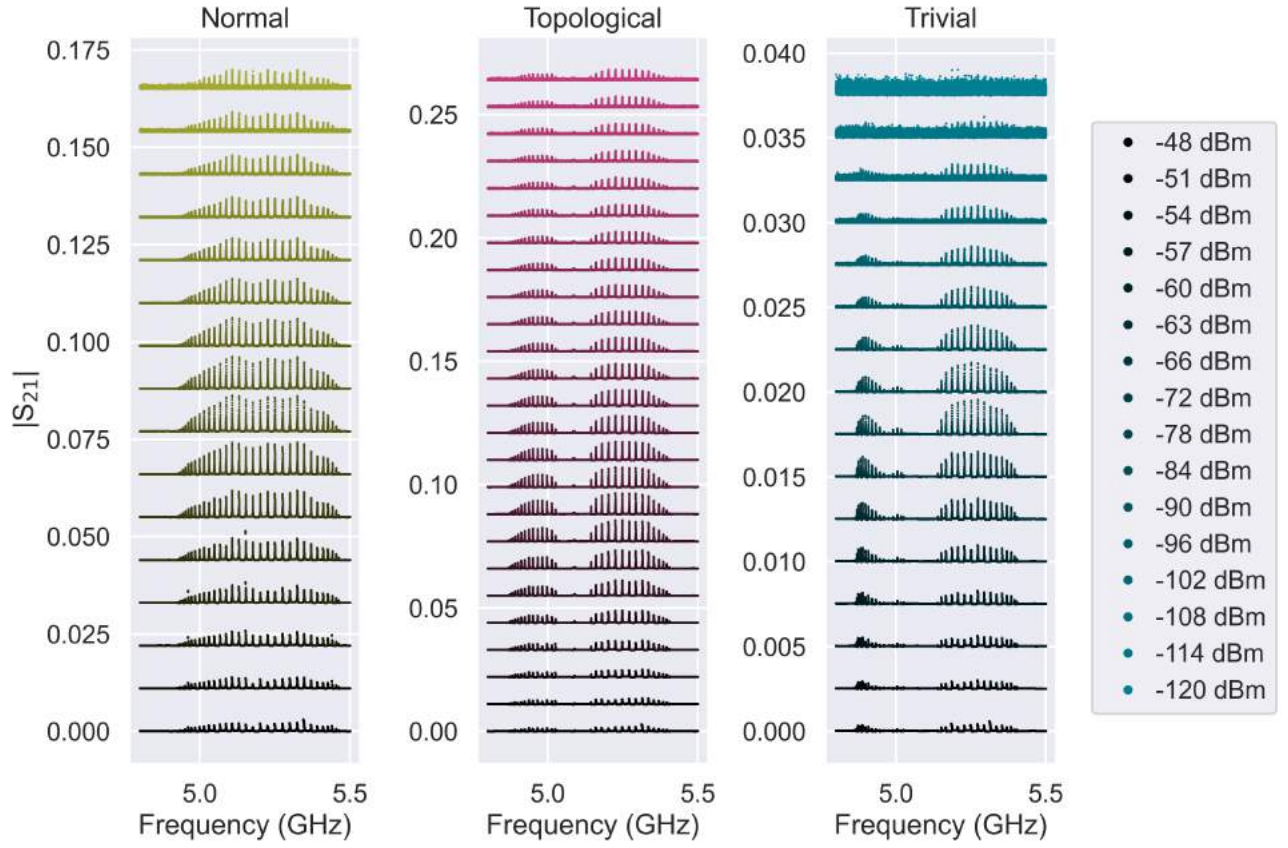


Fig. C.10: Power Sweep of 32 Resonator Array.

## C.5 64 LC Array with Ghost Feedline

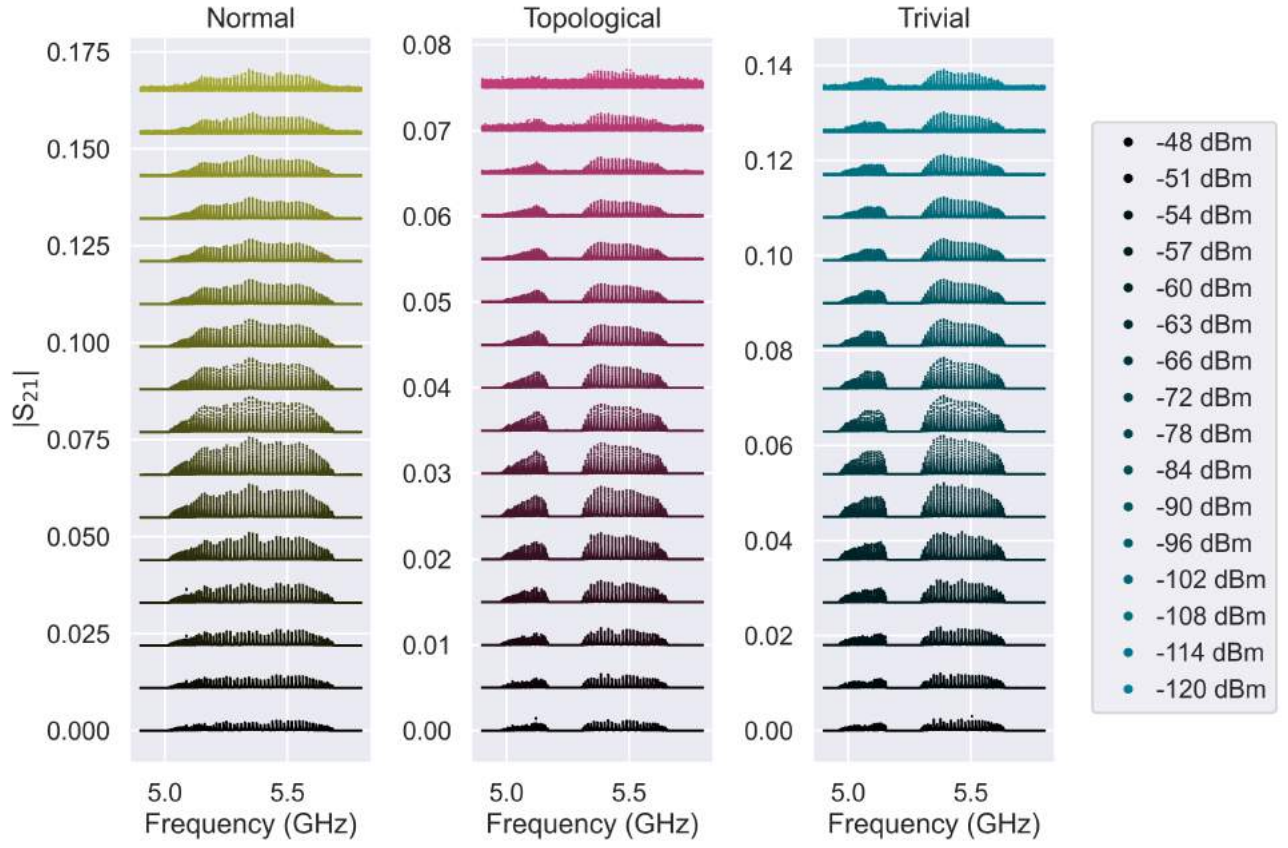


Fig. C.11: Power Sweep of 64 Resonator Array.

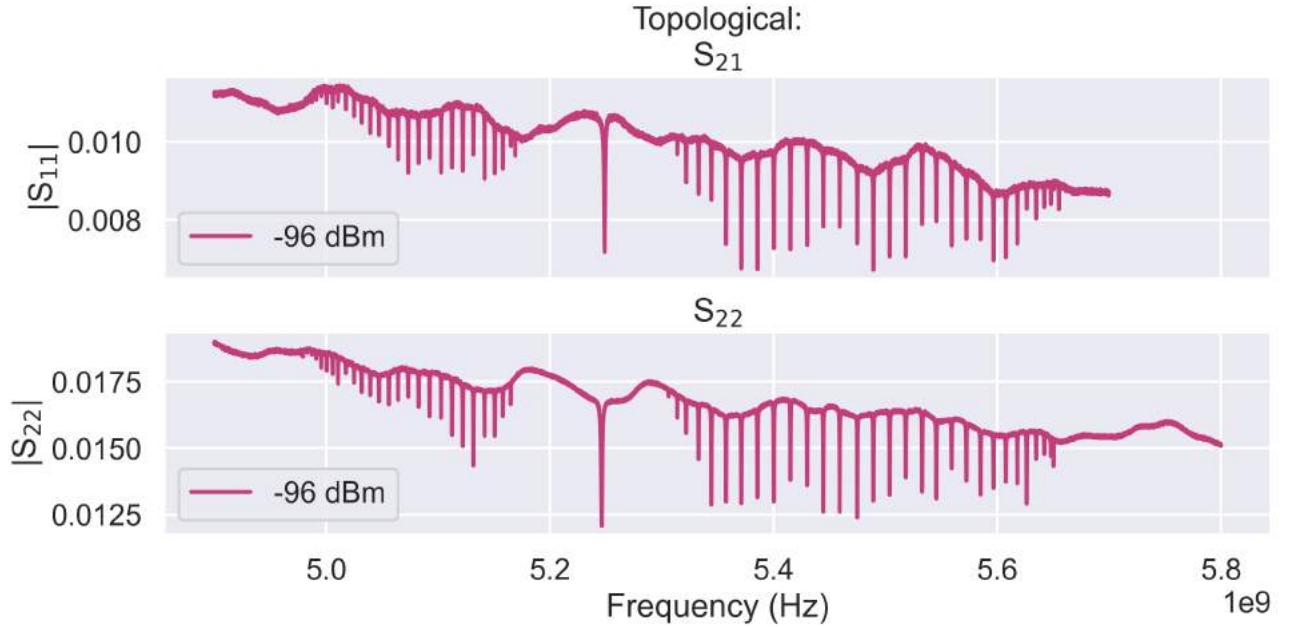


Fig. C.12: Reflection Spectra for Topological 64 Resonator Array. Top:  $S_{11}$  reflection amplitude for -96 dBm drive power. Bottom:  $S_{11}$  reflection amplitude for -96 dBm drive power, as shown in Fig. 5.10 of the main text.





**Declaration on Scientific Integrity**

(including a Declaration on Plagiarism and Fraud)

Translation from German original

Title of Thesis: Microwave Superconducting Metamaterials  
for Analog Quantum Simulation

Name Assessor: Prof. Dr. Christian Schönenberger

Name Student: Vera Jo Weibel

Matriculation No.: 15-058-860

With my signature I declare that this submission is my own work and that I have fully acknowledged the assistance received in completing this work and that it contains no material that has not been formally acknowledged. I have mentioned all source materials used and have cited these in accordance with recognised scientific rules.

Place, Date: Rothenburg, Student: V. Weibel  
28.11.2020

Will this work be published?



No



Yes. With my signature I confirm that I agree to a publication of the work (print/digital) in the library, on the research database of the University of Basel and/or on the document server of the department. Likewise, I agree to the bibliographic reference in the catalog SLSP (Swiss Library Service Platform). (cross out as applicable)

Publication as of: 06.12.2021

Place, Date: 03.12.2021 Student: V. Weibel

Place, Date: Basel 3.12.2021 Assessor: [Signature]

Please enclose a completed and signed copy of this declaration in your Bachelor's or Master's thesis.